

Force sensing and surface analysis with optically trapped microprobes



Dissertation

zur Erlangung des Grades eines
Doktors der Naturwissenschaften
(Dr. rer. nat.)

der Naturwissenschaftlichen Fakultät IV
- Chemie und Pharmazie -
der Universität Regensburg

vorgelegt von
Francesco Pampaloni
aus Firenze
2002

Die Arbeit wurde angeleitet von: PD Dr. Jörg Enderlein

Promotiongesuch eingereicht am: 19.02.2002

Promotionskolloquium am: 08.04.2002

Prüfungsausschuß:

Vorsitzender:	Prof Dr. H. Krienke
1. Gutachter:	PD Dr. J. Enderlein
2. Gutachter:	Prof. Dr. W. Kunz
3. Gutachter:	Prof. Dr. C. Steinem

"What I want to talk about is the problem of
manipulating and controlling things on a small scale".

Richard P. Feynman

There's plenty of room at the bottom

To my wife Chiara

Contents

	<i>Page</i>
Chapter I <i>Introduction</i>	1
1.1 The forces exerted by light	1
1.2 The development of optical tweezers	5
1.3 Theory of optical trapping	7
1.4 Applications of optical tweezers	12
1.5 Organization of this work	16
 <i>References</i>	 17
 Chapter II <i>System development and methods</i>	 24
2.1 Construction of optical tweezers	24
2.1.1 <i>General optical trap design consideration</i>	24
2.1.2 <i>Description of the optical set-up</i>	29
2.1.3 <i>Optical tweezers alignment procedure</i>	31
2.1.4 <i>High-resolution position measurement techniques</i>	33
2.1.5 <i>PSD's signal conditioning</i>	38
2.1.6 <i>Data acquisition</i>	43
2.1.7 <i>PSD circuit: performance and electronic noise control</i>	44
2.2 System performance	49
2.2.1 <i>Laser</i>	49

2.2.2	<i>position and force detector</i>	49
	<i>References</i>	64
Chapter III	<i>Optical tweezers as a force transducer: microrheology and surface scanning</i>	65
3.1	What is microrheology	65
3.2	Microrheology with optical tweezers	66
3.2.1	<i>Introduction</i>	66
3.2.2	<i>Brownian motion in a harmonic potential</i>	67
3.2.3	<i>Set-up</i>	70
3.2.4	<i>Measurements</i>	72
3.2.4.1	<i>Trap stiffness</i>	73
3.2.4.2	<i>Viscosity of glycerine/water mixtures</i>	73
3.2.4.3	<i>Discussion</i>	78
3.3	Scanning probe microscopy with optical tweezers	80
3.3.1	<i>Introduction</i>	80
3.3.2	<i>Set-up</i>	82
3.3.3	<i>Measurements</i>	84
3.3.4	<i>Discussion</i>	86
	<i>References</i>	88
Chapter IV	<i>Compact optical tweezers using aspherical optics</i>	92

4.1	Introduction	92
4.1.1	<i>Motivation: why compact optical tweezers</i>	92
4.1.2	<i>the optical pickup of a compact disk drive</i>	94
4.2	Compact optical tweezers	97
4.2.1	<i>Testing set-up</i>	97
4.2.2	<i>Compact optical tweezers prototype</i>	101
4.3	Discussion	105
	<i>References</i>	107
Chapter V	<i>Hollow beam optical tweezers by using an axicon</i>	109
5.1	Hollow beam laser traps	109
5.1.1	<i>Limitation of Gaussian-beam optical traps</i>	109
5.1.2	<i>Scanning-beam optical trap</i>	110
5.1.3	<i>Optical trapping with doughnut-mode beams</i>	111
5.2	Hollow beam optical trap by using an axicon	119
5.2.1	<i>Introduction</i>	119
5.2.2	<i>Set-up</i>	123
5.2.3	<i>Measurements</i>	124
5.2.4	<i>Discussion</i>	126
	<i>References</i>	128
	<i>Summary</i>	132

1.1 *The forces exerted by light*

The idea that light can exert forces on material bodies can be traced back Johannes Kepler (*De cometis*) and Isaac Newton (*Opticks*). However, it took another two centuries before James Clerk Maxwell was able to calculate quantitatively the strength of the optical force (so-called *radiation pressure*) within the framework of his theory of electromagnetism (1873). Light, when understood as a propagating electromagnetic field, carries energy and momentum. The energy flow of an electromagnetic wave across a unit surface and time is given by the so called Poynting vector:

$$\vec{S} = \frac{c}{4\pi} \vec{E} \times \vec{H} \quad (1.1)$$

*radiation
pressure*

where c is the velocity of light, and \vec{E} and \vec{H} are the electric and magnetic field, respectively. If one denotes by $\langle S \rangle$ the time average of this vector, then the radiation pressure is given by

$$P_R = \frac{\langle S \rangle}{c} (1 + r) n \quad (1.2)$$

where r is the reflectivity of the body the radiation acts on, and n the refractive index of the medium. For black bodies one has $r = 0$, while $r = 1$ for a perfectly reflecting surface. Radiation pressure is very small when light from conventional sources (like the sun or a lamp) is absorbed or reflected by macroscopic objects. For example, direct sun illumination of a perfectly reflecting surface causes a negligible pressure of 4.7×10^{-6} N/m². Even if

radiation pressure is very small, its effects are relevant in nature. For example, radiation pressure allows stars like the sun to exist by counteracting the force of their own gravity, and stellar radiation pressure is one of the most important mechanisms responsible for particle dynamics in the interstellar medium. The existence of radiation pressure was first demonstrated experimentally by the Russian physicist Pyotr Nikolayevich Lebedev (1901) with an apparatus consisting of a set of flat metallic sheets with very low mass placed into a vacuum chamber. The incident light emerging from a voltaic arc induced a measurable deflection of the metallic sheets due to radiation pressure. The value of the light pressure found by Lebedev agreed well with that obtained by Maxwell's theory, which was considered to be conclusive evidence of the validity of the new electromagnetic theory of light.

An alternative explanation of radiation pressure is provided by quantum theory. According to quantum theory, light is constituted of photons. Each photon carries a momentum given by the De Broglie relation:

$$p = \frac{h}{\lambda} \quad (1.3)$$

where h is Planck's constant and λ the wavelength of light. By assuming light as a flow of photons carrying momentum, one can use a simple geometric optics model to understand the origin of optical forces. Consider a ray of light which propagates in a medium of uniform refractive index (Fig. 1.1a). All its momentum (\vec{p}_1) is directed along the propagation direction. As the ray meets an object, reflection (Fig. 1.1b) and refraction (Fig. 1.1c) occur and the momentum of the photons changes direction (\vec{p}'_1).

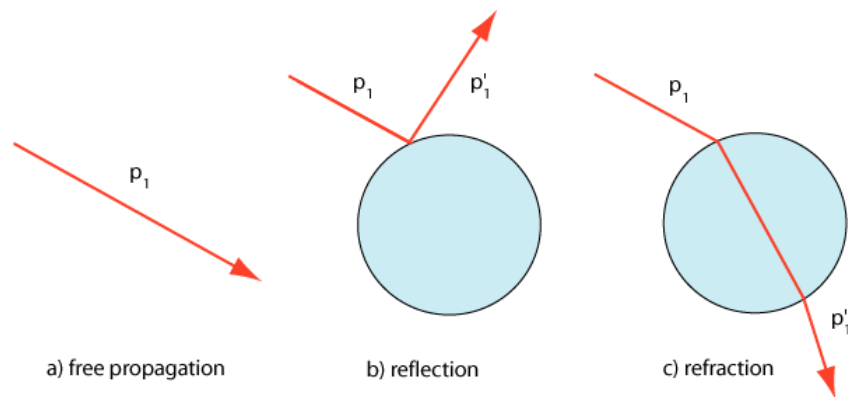


FIGURE 1.1 Change of momentum of light due to reflection and refraction.

Since the total momentum of the system is conserved (momentum conservation), the change in the momentum of the photons has to be balanced by an equal and opposite change in the momentum of the object. Thus, by Newton's second law, the object experiences a force pointing in the direction of the momentum change:

$$\vec{F} = \frac{d}{dt}(\Delta\vec{p}) \quad (1.4)$$

Fig. 1.2 illustrates how reflection and refraction of light induce forces on a spherical object, where \vec{p}_1 and \vec{p}'_1 are the momentum of the free propagating ray and the momentum of the ray after interaction with the object, respectively. $\Delta\vec{p}$ is the momentum change and $\vec{p}_2 = -\Delta\vec{p}$ the momentum acquired by the object.

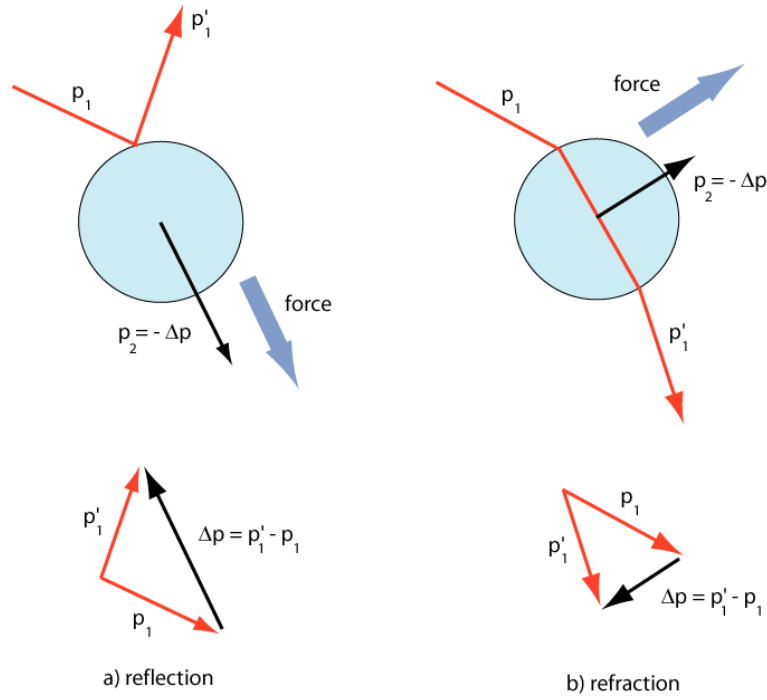


FIGURE 1.2 Forces on a spherical object induced by reflection and refraction of light.

In case of reflection (Fig. 1.2a), the force points into the direction of the incident ray, whereas the force induced by refraction points transversely to the ray (Fig. 1.2b). The “reflection” force is usually called *scattering force* (\vec{F}_{sc}), because it arises when photons are scattered by an object. Moreover, since the “refraction” force points in the direction of the gradient of light

gradient force

intensity (Fig. 1.3), it is also termed *gradient force* (\vec{F}_{gr}) [Gordon 1973]. The gradient force drives the object towards the region of highest brightness.

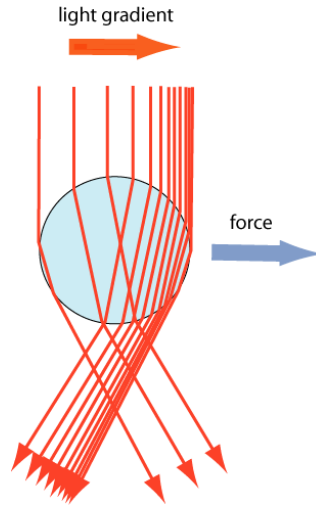


FIGURE 1.3 The “refraction” force in a gradient of light intensity.

The direction of the gradient force is affected by the relative refractive index of the particle compared to the surrounding medium:

influence of the refractive index on the optical forces

$$\tilde{n} = \frac{n_{particle}}{n_{medium}} \quad (1.5)$$

If the relative refractive index is greater than unity (as for a polystyrene sphere in water, $\tilde{n} = 1.2$), the gradient force attracts the particle towards the optical axis. If the relative refractive index is lower than unity (as for water bubbles in paraffin oil, $\tilde{n} = 0.7$), the particle is pushed out of the beam. In summary, the radiation pressure acting onto an object is given by:

$$\vec{F}_{tot} = \vec{F}_{sc} + \vec{F}_{gr} \quad (1.6)$$

In the case of *dielectric* objects, which are transparent to light, the gradient force predominates over the scattering force. In contrast, for highly reflecting objects (e.g. a metallic particle), the scattering force is usually stronger. When focusing a parallel light beam with a lens (Fig. 1.4), all the rays ideally converge to a point (the focus) which has the highest light intensity. A reflecting object will be strongly repelled from the focus

because the scattering force is at a maximum there (the light intensity is maximum). In contrast, the gradient force will attract a dielectric object with $\tilde{n} > 1$ toward the focus. The object experiences a restoring force which can *hold it trapped in three dimensions*. This is the principle of optical trapping. However, to realize such an optical trap in practice, some conditions must be met. Since the gradient force (attractive) must overcome the scattering force (repulsive), a very steep intensity gradient has to be created. That requires a very intense light source and a lens capable of focusing the light to the smallest achievable spot. The sharper the focus, the steeper the gradient. The first condition is met by using a laser light source, and the second condition by using a high-numerical aperture microscope objective. A laser and a good microscope objective are indeed the two fundamental components of every optical trapping system.

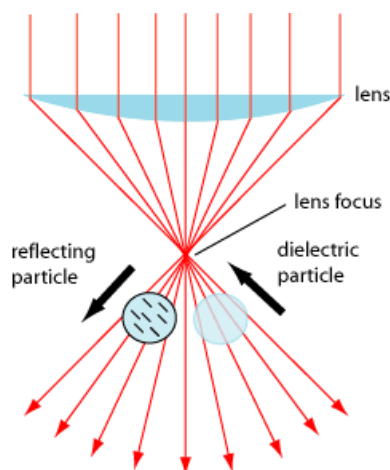


FIGURE 1.3 Scattering and gradient force in a focused light beam.

1.2 *The development of optical tweezers*

About sixty years after the fundamental experiment of Lebedev, the invention of the laser (in the early 1960s) started a new era in the study of light/matter interaction. Lasers generate a monochromatic and very intense light, which can exert a radiation pressure large enough to accelerate, decelerate, deflect, guide and trap small particles. An early pioneer who applied lasers in the study of radiation pressure was the American physicist Arthur Ashkin. In the 1970s, Ashkin and his co-workers at AT&T

optical levitation

Laboratories showed that a micron-sized sphere could be *trapped* by using two counter-propagating beams, so that the scattering forces from both beams balanced each other, while the gradient forces acted together to keep the particle near the optical axis (Fig. 1.4b) [Ashkin 1970]. By adjusting the relative power of the two beams, the particle could be moved back and forth along the optical axis or held at a fixed position. Later, Ashkin demonstrated that micron-sized glass spheres could be *levitated* in air by a laser beam oriented vertically upward and focused to a spot radius of $6.2\text{ }\mu\text{m}$ (Fig. 1.4a) [Ashkin 1971]. Gravity counterbalanced the scattering force exerted by the laser, and the gradient force provided transversal stability, allowing the levitation of the particle.

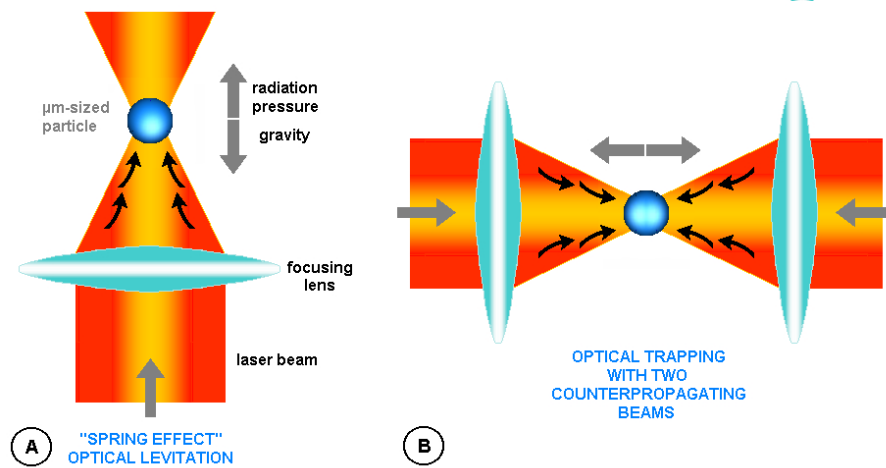


FIGURE 1.4 Optical levitation and trapping of a particle based on scattering force.

single beam optical trap

While optical levitation proved to be a useful tool for investigating the effects of radiation pressure, the need for an external restoring force (either gravity or a second laser beam) prevented its application as a tool for micro-manipulation. In 1986, Ashkin and Dziedzic formed a *three-dimensional optical trap* for “high index” particles by focusing a single TEM_{00} laser beam (TEM_{00} beams have a Gaussian-shaped intensity profile, confer also Chapter V) with a high-numerical aperture microscope objective [Ashkin 1986]. The focused spot has a diameter of the order of the light wavelength or, in other words, is *diffraction-limited*. Since the intensity gradient is extremely steep in all the three dimensions around the diffraction-limited focus, the gradient force along the optical axis is of the same order of magnitude as the gradient force perpendicular to it. Thus, this force

overcomes both the gravitational and scattering forces and creates a stable optical trap. With *the single-beam gradient-force optical trap*, known also as *optical tweezers*, sub-micrometer and micrometer sized particles can be trapped in water and manipulated in three dimensions. Optical tweezers can generate forces up to a few hundred *piconewtons* ($1 \text{ pN} = 10^{-12} \text{ N}$). Such a force range is sufficient for efficient manipulation of colloidal dielectric particles or cells and bacteria. Further considerations about the design of optical tweezers are given in Chapter II.

1.3 *Theory of optical trapping*

Rayleigh and Mie regimes

Optical trapping of particles is theoretically well understood in two regimes. The *Rayleigh regime* corresponds to a particle radius a much smaller than the wavelength of the light ($a \ll \lambda$). The *Mie regime* (or ray optics regime) is valid for a particle radius much larger than the wavelength ($a \gg \lambda$). In both limits, significant simplifications can be made when calculating the force exerted by optical tweezers. However, for particles with a size comparable to the optical wavelength ($a \cong \lambda$), a complete wave-optical modeling of the particle light interaction is necessary for calculating the optical trapping forces. The situation becomes even more complicated for non-spherical or anisotropic particles. Such particles are of particular importance because most biological structures and crystals are non-spherical and often anisotropic. For the Mie limit $r \gg \lambda$, a purely ray optics model for optical trapping was developed by Ashkin [Ashkin 1992] following the formalism of Roosen [Roosen 1979]. In that model, each ray is assigned a proper intensity, direction and state of polarization. The propagation direction of a ray changes when it reflects and refracts, and changes polarization at dielectric interfaces. Diffractive effects are neglected. The light beam is treated as a bundle of individual rays directed toward a single focal point by the objective. If P is the power of a single ray propagating in a medium of refractive index n_{medium} , the corresponding momentum per second is:

ray optics model

$$p = \frac{n_{\text{medium}} P}{c} \quad (1.7)$$

The computation of the force exerted by the incident ray on the sphere is done by summing the contributions of the reflected ray of power PR and the

infinite number of emergent refracted rays (arising from multiple reflection inside the particle) of successively decreasing power PT^2 , PT^2R , PT^2R^2 , ... PT^2R^n . Here, the quantities T and R are the Fresnel transmission and reflection coefficients at the particle's surface and are both dependent on incidence angle and ray polarization. The total scattering and gradient force exerted by a highly convergent beam are given by the vector sums of the scattering and gradient force contributions of the individual rays of the beam. The total force acting in the trap is thus found as:

$$F_{trap} = F_{grad} + F_{scat} = Q \frac{n_{medium} P}{c} \quad (1.8)$$

Q is a dimensionless efficiency parameter resulting from summing F_{grad} and F_{scat} over all angles. This model is in relative a good agreement with the experimental data (within 20%) for particles larger than 10λ [Tlusty 1998]; other authors, for example Wright et al. [Wright 1994] and Saloma et al. [Saloma 1995], support the validity of this model for particles larger than $5 \mu\text{m}$, while it fails for smaller particles because the finite size of the beam is ignored. The geometric optics theory predicts that overfilling the back pupil of the objective leads to stronger trapping than just filling it. This can be understood when taking into account that rays with highest inclination angle towards the optical axis contribute most to the intensity gradient in axial direction. Using a ray optics approach, calculation were also done for the force acting on cylindrical micro-particles [Gauthier 1997, Ukita 1997]. Recently, a theoretical analysis of the force exerted on a red blood cell (which has the shape of a biconcave disk) by a dual-beam optical tweezers was presented by Grover et al. [Grover 2000]. The analysis is based on a ray-optics recursive algorithm.

Rayleigh model

If the particle is sufficiently small compared to the wavelength of light, the Rayleigh (or dipole) approximation can be applied to the computation of radiation pressure. In the Rayleigh limit, the electromagnetic field of light can be considered to be uniform over the whole extent of the particle. Therefore, the particle can be treated as an induced point dipole. Similarly to the Mie limit, the radiation pressure force can be decomposed into a scattering and gradient component. The harmonically oscillating electric field of light induces an oscillating electric field within the particle. Then the particle acts as an oscillating electric dipole which radiates secondary (or scattered) waves into all directions. The scattering changes the distribution of the energy flux of the electromagnetic wave, causing a momentum

transfer onto the particle. The resulting scattering force is given by:

$$\vec{F}_{scat}(\vec{r}) = \frac{n_{medium}}{c} C_{rp} \vec{S}(\vec{r}) \quad (1.9)$$

where C_{rp} is the cross section for the radiation pressure on the particle, $\vec{S}(\vec{r})$ is the time-averaged Poynting vector of the trapping light at the particle's position \vec{r} , n_{medium} is the refractive index of the medium, and c the velocity of light in vacuum [Vischer 1992a, Svoboda 1994, Harada 1996]. In the case of small dielectric particles in the Rayleigh regime, where the particle scatters the light isotropically, C_{rp} is equal to the scattering cross section C_{scat} , and is given by:

$$C_{rp} = C_{scat} = \frac{8}{3} \pi k_0^4 \left(\frac{m^2 - 1}{m^2 + 2} \right)^2 a^6 \quad (1.10)$$

with $m = n_{particle} / n_{medium}$ being the relative index of refraction, $k = 2\pi n_{medium} / \lambda$ is the wave number of the light, and a is the particle radius. The gradient component of radiation pressure is caused by the gradient of electric field energy density at the beam focus. This force is just the Lorentz force acting on a dipole in an electromagnetic field:

$$\vec{F}_{grad} = (\vec{p} \cdot \vec{\nabla}) \vec{E} + \frac{1}{c} \frac{d\vec{p}}{dt} \times \vec{B} \quad (1.11)$$

With $\vec{p} = \alpha \vec{E}$ the dipole moment, Eq. (1.10) can be rewritten as

$$\vec{F}_{grad} = \alpha \left((\vec{E} \cdot \vec{\nabla}) \vec{E} + \frac{1}{c} \frac{d\vec{E}}{dt} \times \vec{B} \right) \quad (1.12)$$

with α being the polarizability of the particle given by

$$\alpha = \frac{m^2 - 1}{m^2 + 2} r^3. \quad (1.13)$$

Using the vector identity

$$(\vec{E} \cdot \vec{\nabla}) \vec{E} = \vec{\nabla} \left(\frac{1}{2} E^2 \right) - \vec{E} \times \vec{\nabla} \times \vec{E} \quad (1.14)$$

and the Maxwell equation

$$\vec{\nabla} \times \vec{E} + \frac{1}{c} \frac{\partial \vec{B}}{\partial t} = 0 \quad (1.15)$$

Eq. (1.11) can be rewritten as

$$\vec{F}_{grad} = \alpha \left(\vec{\nabla} \left(\frac{1}{2} E^2 \right) \vec{E} + \frac{1}{c} \frac{\partial (\vec{E} \times \vec{B})}{\partial t} \right) \quad (1.16)$$

If a continuous wave laser is used, the time average of the second term in Eq. (1.16) is zero. Then the time-averaged gradient force on the spherical Rayleigh particle is:

$$\vec{F}_{grad} = n_{medium} \alpha \left(\frac{1}{2} \vec{\nabla} \langle E^2 \rangle \right) \quad (1.17)$$

In Eq. (1.17), E^2 is proportional to the electric energy density of the electromagnetic field. From Eq. (1.16) follows that, if $n_{particle} > n_{medium}$

($\alpha > 0$), the gradient force is directed towards region of high electric energy densities. Because induced dipoles always oppose the inducing field, the attractive force is independent of the field's polarization. If $n_{particle} < n_{medium}$, the gradient force pushes the particle out of that region. For stable trapping, $F_{scat} \leq F_{grad}$ is necessary. Increasing the numerical aperture decreases the focal spot size and consequently increases the strength of the gradient force, because the energy density gradient is steeper.

The geometric optics as well as the Rayleigh scatterer model work well only for the two limits of $a \gg \lambda$ and $a \ll \lambda$. Unfortunately, most of the applications of optical tweezers use spherical dielectric particles with a radius between 1 and 10 μm . In this intermediate regime, both the models fail in giving an accurate computation of the optical forces. To compute the interaction of a particle with a focused laser beam in the intermediate regime, many approaches have been developed. A possible strategy is: (1) find an expression for the electric field in the focal plane produced by the strongly focused incident beam. The exactly calculated spatial distribution of the electromagnetic field in object space near the laser focus by Richards and Wolf [Richard 1959] is usually used [Maia Neto 2000]. (2) Find an expression for the electric field scattered by the object. Lorentz-Mie scattering theory may be used [Maia Neto 2000], which is an analytical

*limitation of ray
optics and
Rayleigh models*

*calculation of
optical forces in
intermediate
regime*

method but is limited to isotropic homogeneous sphere illuminated by a plane wave. (3) The incident and the scattered fields give the total field in the region near the focus:

$$\vec{E} = \vec{E}_{incident} + \vec{E}_{scattered}; \vec{H} = \vec{H}_{incident} + \vec{H}_{scattered} \quad (1.18)$$

Subsequently, the time-averaged radiation pressure force is found by inserting the total field into the Maxwell stress tensor \vec{T} and integrating over the surface of the particle:

$$\langle \vec{F} \rangle = \left\langle \oint_S \vec{T} dS \hat{n} \right\rangle \quad (1.19)$$

with:

$$T_{ik} = \frac{1}{4\pi} \left(\epsilon_0 E_i E_k + B_i B_k - \frac{1}{2} (\epsilon_0 E^2 + B^2) \delta_{ik} \right) \quad (1.20)$$

*calculation of
optical forces in
intermediate
regime – the
T-matrix method*

An alternative approach expresses the incident field in terms of a sum of vector spherical harmonics. The expansion coefficients of the scattered field are found from the incident field by considering the boundary conditions at the surface of the scatterer. The most widely used of such approaches is the T-matrix method [Gahagan 1998, Nieminen 2001]. The T-Matrix method is applicable to calculating scattered fields for an arbitrarily shaped dielectric, although it is most frequently used to calculate scattering from axisymmetric dielectrics. The expansion coefficients of the scattered field are calculated from the coefficients of the incident beam by using the T(ransformation)-matrix, which contains all the information about the morphology of the particle. This method is computationally efficient and a number of computer codes implementing this technique are freely available.

In summary, candidates for optical trapping are:

- (1) dielectric particles with refractive index larger than that of the surrounding medium. The attractive gradient force allows stable trapping up to about 25 μm in diameter. For larger particles, the gravitational force overcomes both the scattering and gradient forces.
- (2) Rayleigh metallic particles with size up to about 40 nm [Svoboda 1994]: in this size range, the high polarizability of metallic particles produces a gradient force sufficiently strong to overcome the strong scattering.

Micrometer-sized metallic particles and dielectric particles with refractive index lower than the medium cannot be trapped with a single beam optical

tweezers. On one side, the scattering force on “Mie” metallic particles is too large compared with the gradient force, on the other side, the gradient force on “low-index” particles points into a direction opposite to the gradient. However, such particles can be trapped by using alternative trap configurations (see Chapter V). Light carries also an angular momentum associated with the polarization of light and with the phase structure of the beam. Rotation of trapped birefringent and absorptive particles can be induced by an elliptically or circular polarized beam (see Chapter V for further details about this topic).

1.4 *Applications of optical tweezers*

Optical trapping is a technique successfully employed in a wide range of applications, from cellular biology to colloidal sciences. Optical tweezers can be used as an effective micro-manipulator, with the advantage of capturing and moving objects without “true” mechanical contact that could contaminate and damage the sample. One of the most interesting features of optical tweezers is the possibility to exert and measure forces in the range of pN. Such a range is relevant at the scale of microscopic organisms. Starting from the pioneering trapping experiments by Ashkin on viruses, yeast cells, bacteria, and protozoa [Ashkin 1987a, Ashkin 1987b, Ashkin 1989, Ashkin 1990], optical tweezers are now an invaluable tool in cellular biology [Svoboda 1994, Schütze 1998]. Trapped silica or latex beads are often used in association with optical tweezers for exerting or sensing forces. By using optically trapped latex *handles*, micro-mechanical experiments can be performed on cells and microorganisms, both *in vivo* and *in vitro*. By exerting forces with trapped dielectric beads, the relationship between morphology and function in the membrane skeleton of cells was studied [Kusumi 1998, Sako 1998]. Other researchers investigated the formation of tethers and fences on membranes [Dai 1998, Dai 1999]. The torsional compliance and the torque-speed relationship of bacterial flagella [Block 1989, Block 1991, Berg 1993, Xiaobing 2000] were also studied. Optical tweezers allowed the measurement of the shear modulus and the elasticity of human erythrocyte in blood samples from patients with hemolytic disorders [Hénon 1999, Sleep 1999]. Further applications were the measurement of the swimming force of sperm [Colon 1992] and the use of optical manipulation for *in vitro* fertilization (in combination with the so-called

*applications in
cellular biology*

*laser-induced
photodamage of
samples*

optical scalpel for drilling the *zona pellucida* of an oocyte) [Schütze 1994b, Clement-Sengewald 1996]. Chromosomes and organelles inside the cell were also manipulated and sectioned *in vivo* [Ashkin 1990, Liang 1993, Felgner 1998a]. Optical tweezers were also used in cell sorting and screening [Buican 1987, Tashiro 1993, Shikano 1999, Ericsson 2000].

Since a huge flux of photons is directed onto an optically trapped specimen (for a power of 100 mW the energy density is 10^7 W/cm², with an associated flux of photons of 10^{26} photons/s·cm²), the possibility of photodamage due to high light intensity must be considered. As recognized early by Ashkin and Dziedzic [Ashkin 1989], the choice of near-infrared laser wavelengths is crucial to avoid the death of microorganisms and cells. The near-infrared region corresponds to a window of transparency, situated between the absorption band of many biological chromophores and the increasing absorption of water at longer wavelengths [Liang 1996; see also Chapter II]. Liu et al. [Liu 1995a, Liu 1996] investigated the heating of cells trapped with a beam at 1064 nm by using microfluorimetry. They observed a local increment of the temperature of 1°C for each 100 mW of output laser power. Since cells can be already trapped at an output power of a few tens of mW, the damage due to local transient heating is negligible. Multiphotons processes were also taken in account as a source of photodamage when short-pulse lasers are used, although pulsed lasers are not commonly employed in optical trapping [König 1995a, König 1995b, König 1996, Liu 1995a, Liu 1995b]. Neuman et al. [Neuman 1999] systematically investigated on *Escherichia coli* the wavelength dependency of photodamage by using a tunable Titanium-sapphire cw-laser. They found that the most harmless wavelengths are 970 and 830 nm, which are by about a factor of two less damaging than the 1064 nm wavelength of a Nd:YAG laser. In contrast, the region between 870 and 910 nm should be avoided. In these experiments, the lifetime of the bacterium linearly correlated to the laser intensity. This linear relationship suggested a one-photon mechanism of photodamage. The authors deduced that the toxic agent could be singlet oxygen, produced in the bacterium by a chromophore not yet identified.

*applications in
molecular
biology: motor
proteins*

In molecular biology, optical tweezers are playing a central role for the study of the so-called *motor proteins* (or *molecular motors*), like kinesin, dynein, and the myosin/actine system [Spudich 1990]. Such experiments are now generally called “optical trapping nanometry” [Ishijima 2001]. Kinesin is a “mechanochemical” enzyme that couples ATP hydrolysis to movement along microtubules (the major component of cellular organelles like mitotic spindle and cilia; it is thought to form the framework that organizes the

*applications in
molecular
biology: RNA
polymerase*

*applications in
molecular
biology:
rheology of DNA*

cell). In now classical experiments [Block 1990, Kuo 1993], single kinesin molecules were coupled to silica beads. A bead was individually manipulated with optical tweezers and brought directly onto a microtubule deposited on a coverslip. After blocking the laser, the motion of the bead along the microtubule was observed with video-microscopy. The force exerted by a single kinesin molecule was directly measured by finding the minimum laser power required for stopping the motion of the bead. By determining the displacement of the trapped bead with sub-nanometer resolution (by using an interferometric method), Svoboda et al. [Svoboda 1993] proved that kinesin moves stepwise along the microtubule. Recently, it was determined that the step length is 5.3 nm [Kitamura 1999]. With a similar approach, the force and displacement produced by myosin on an actin filament (myosin and actin are the proteins regulating the contraction of muscular tissues) was measured by several researchers [Nishizaka 1995, Tsuda 1996, Guilford 1997, Kawai 2000, Knight 2001]. Also dynein, a protein that powers flagellar motion, was investigated with optical trapping nanometry [Shingyoji 1998]. Several studies concentrate on the enzyme RNA polymerase (RNAP). RNAP is a true motor protein that generates considerable force (> 14 pN) and proceeds along DNA at the speed of 10 nucleotides per second. The force exerted on DNA by a single molecule of *Escherichia coli* RNAP during transcription was measured with optical trapping nanometry [Yin 1995, Wang 1998]. In these experiments, the enzyme was immobilized on the surface of a coverglass while the DNA template was linked to an optically trapped bead. Using interferometric position detection, the displacements of the DNA drawn through the polymerase were monitored during transcription (note that *in vivo*, the RNAP moves rapidly along the DNA template) and the involved force and velocity were calculated. In another work, a DNA filament linking two beads was stretched in a dual-beam optical tweezers. The displacement of a single RNAP along the DNA was then observed in real-time by fluorescence microscopy [Harada 1999]. An increasing number of works investigate the rheological and mechanical properties of a DNA filament, which has proven to be a useful model system to study the complex dynamical behavior of polymers. Again, the used approach is to attach a DNA filament to a latex bead, trapping it and analyzing the displacement of the bead from the trap's center produced by an external force acting on the DNA: the force on DNA can be exerted by hydrodynamic flow [Larson 1997, Hatfield 1999], by mechanical anchoring [Baumann 2000], or by the thermal motion [Meiners 2000].

*optical tweezers
used for
analytical assays*

Optical tweezers were also employed for performing sensitive analytical assays. An innovative technique was developed by Mammen et al. [Mammen 1996]: for evaluating the effect of polyvalent inhibitors of virus adhesion, latex beads were covalently coupled with viral proteins. Then, by using dual-beams optical tweezers, single beads and target cells were brought in contact with defined velocity. Through a statistical analysis of the contact-detachment events over a large number of cells, Mammen et al. were able to determine both the binding constant and the concentration of the inhibitor, down to femtomolar concentrations. Galneder et al. [Galneder 2001] presented an elegant analytical method that combines laser trapping with microelectrophoresis. With this method, the activity of the phospholipase enzyme PLC- δ was measured with high reliability. Silica beads with a diameter of 1 μm were coated with a phospholipid bilayer constituted by a mixture of phosphatidylcholine and the negatively charged phosphatidylinositol 4,5-bisphosphate, which is the substrate of the enzyme PLC- δ . In the experiment, a bead was trapped and an electric field applied to the solution. Since the spring constant of the optical trap was calibrated in advance, the dielectrophoretic force acting on the bead could be calculated by monitoring the displacement of the bead from the trap's center. After introducing the enzyme into the solution, hydrolysis of the phosphatidylinositol started, causing a dropping of the total negative charge on the bead's surface. The corresponding decrease of the dielectrophoretic force was measured by monitoring the bead's displacement with nanometer resolution. A fast quadrant photodiode was employed as position detector [Metha 1998; see also Chapter II for details on monitoring the motion of trapped beads with quadrant photodiodes]. With such a method, the enzyme kinetics could be obtained with high accuracy.

*optical tweezers
in the study of
colloidal systems*

Optical tweezers were also combined with a high-frequency electric field cage (so-called *micro field cage*). The dielectrophoretic force in the cage can be used for characterizing the laser trap [Fuhr 1998]. Recently, controlled rotation of micromachined elements was induced by the torque exerted by radiation pressure. These miniature rotating devices may find application as actuators in lab-on-a-chip technology, or for measuring local viscosity values [Galajida 2001, Higurashi 1994, Higurashi 1998, Ukita 1997, Luo 2000, Paterson 2001, Gauthier 1997, Gauthier 1999a, Gauthier 1999b, Friese 1998a, Friese 1998b, Friese 2001]. Optical tweezers have also proven to be extremely useful for studying colloidal systems. Colloidal probes, which are usually sub-micrometer particles, are trapped and their dynamic behavior is monitored. Important rheological parameters of a system (like its

viscosity or viscoelasticity) can be obtained by the “colloidal probe force spectroscopy” based on optical trapping. The applications of optical tweezers in colloids physics are further discussed in Chapter III.

1.5 Organization of this work

The core of this work is the application of optical tweezers as a sensitive force transducer capable of measuring tiny forces in the range of piconewtons, with nanometer spatial and millisecond temporal resolution. An optical tweezers set-up with such a performance was developed and applied to “colloidal probe force spectroscopy” as well as to measuring the topography of a cell membrane by scanning a trapped probe (“optical force microscopy”). Because the design and development of the system as described in Chapter II (**System development and methods**) is an integrating part of the whole work, there is no clear-cut separation between “Material and methods” and “Results”. Indeed, the development of the system is itself a result of this work. In Chapter III (**Optical tweezers as a force transducer: microrheology and surface scanning**), the viscosity of glycerin/water mixtures is measured through the analysis of the Brownian motion of a trapped bead. A new robust method for the analysis of the Brownian motion data is developed. In the same chapter, topography measurements of cellular membranes are performed by scanning and imaging a trapped probe. In Chapter IV (**Compact optical tweezers using aspherical optics**), a novel optical tweezers set-up is described. The set-up is extremely compact and uses a singlet aspherical lens as the focusing element. The use of an aspherical lens has many advantages over conventional microscope objectives. The most remarkable is the extra-long working distance of such lenses that allows optical trapping through very thick substrates. Trapping of micrometer-sized dielectric beads through 1 mm-thick glass slides is experimentally demonstrated. Possible applications of this set-up in the fields of micro-fluidics and lab-on-a-chip technology are discussed. Finally, in Chapter V (**Hollow-beam optical tweezers by using an axicon**), a new method for producing a hollow-beam optical tweezers is presented. The hollow beam allows trapping of both metallic particles in Mie regime as well as “low-index” dielectric particles.

References

- [Ashkin 1970] Ashkin A.
Acceleration and trapping of particles by radiation pressure.
Phys. Rev. Lett 24:156-159 (1970)
- [Ashkin 1971] Ashkin A., Dziedzic J.M.
Optical levitation by radiation pressure.
Appl. Phys. Lett. 19: 283-285 (1971)
- [Ashkin 1986] Ashkin A., Dziedzic J.M., Bjorkholm J.E. Chu S.
Observation of a single-beam gradient force optical trap for dielectric particles.
Opt. Lett. 11: 288-290 (1986)
- [Ashkin 1987a] Ashkin A., Dziedzic J.M.
Optical trapping and manipulation of viruses and bacteria.
Science 235: 1517-1520 (1987)
- [Ashkin 1987b] Ashkin A., Dziedzic J.M., Yamane T.
Optical trapping and manipulation of single cells using infrared laser beams.
Nature 330: 769-771 (1987)
- [Ashkin 1989] Ashkin A., Dziedzic J.M.
Optical trapping and manipulation of single living cells using infrared laser beams.
Ber. Bunsenges. Phys. Chem. 93: 254-260 (1989)
- [Ashkin 1989] Ashkin A., Dziedzic J.M.
Optical trapping and manipulation of single living cells using infrared laser beams.
Ber. Bunsenges. Phys. Chem. 93: 254-260 (1989)
- [Ashkin 1990] Ashkin A., Schütze K., Dziedzic J.M., Euteneuer U., Schliwa M.
Force generation of organelle transport measured in vivo by an infrared laser trap.
Nature 348: 346-348 (1990)
- [Ashkin 1992] Ashkin A.
Forces of a single-beam gradient laser trap on a dielectric sphere in the ray optics regime.
Biophys. J. 61: 569-582 (1992)
- [Baumann 2000] Baumann C. G., Bloomfield V. A., Smith S. B., Bustamante C., Wang M. D., Block S. M.
Stretching of single collapsed DNA molecules.
Biophys. J. 78: 1965-1978 (2000)
- [Berg 1993] Berg, H. C., Turner L.
Torque generated by the flagellar motor of Escherichia coli.
Biophys. J. 65: 2201-2216 (1996)
- [Block 1989] Block S.M., Blair D.F., Berg H.C.
Compliance of bacterial flagella measured with optical tweezers.
Nature 338: 514-518 (1989)
- [Block 1990] Block S.M., Goldstein L.S.B., Schnapp B.J.
Bead movement by single kinesin molecules studied with optical tweezers.
Nature 348: 348-352 (1990)

- [Block 1991] Block S.M., Blair D.F., Berg H.C.
Compliance of bacterial flagella measured with optical tweezers.
Nature 338: 514-518 (1989)
- [Buican 1987] Buican T.N., Smyth M.J, Crissman H.A., Salzman G.C., Carleton C.S., Martin J.C.
Automated single-cell manipulation and sorting by light trapping.
Appl. Opt. 26: 5311-5316 (1987)
- [Clement-Sengewald 1996] Clement-Sengewald A., Schütze K., Ashkin A., Palma G. A., Kerlen G., Brem G.
Fertilization of bovine oocytes induced solely with combined laser microbeam and optical tweezers.
J. Assisted Reproduction and Genetics 13: 259-265 (1996)
- [Colon 1992] Colon J. M., Sarosi P. G., McGovern P. G., Dziedzic J. M.
Controlled micromanipulation of human sperm in three dimensions with an infrared optical trap: effect on sperm velocity.
Fertil. Ster. 57: 695-698 (1992)
- [Dai 1998] Dai J., Sheetz M.P.
Cell membrane mechanics.
Methods in cell biology 55: 157-160 (1998)
- [Dai 1999] Dai J., Sheetz M.P.
Membrane tether formation from Blebbing cells.
Biophys. J. 77: 3363-3370 (1999)
- [Ericsson 2000] Ericsson M., Hanstorp D., Hagberg P., Enger J., Nystro T.
Sorting out bacterial viability with optical tweezers.
J. of Bacteriology 182: 5551-5555 (2000)
- [Felgner 1998] Felgner H., Grolig F., Müller O., Schliwa M.
In vivo manipulation of internal cell organelles.
Methods in cell biology 55: 195-202 (1998)
- [Frieze 1998a] Frieze M. E. J., T. A. Nieminen, N.R. Heckenberg, Rubinsztein-Dunlop H.
Optical torque controlled by elliptical polarization.
Opt. Lett. 23: 1-3 (1998)
- [Frieze 1998b] Frieze M.E.J., Nieminen T.A., Heckenberg N.R., Rubinsztein-Dunlop H.
Optical alignment and spinning of laser-trapped microscopic particles.
Nature 394: 348-350 (1998)
- [Frieze 2001] Frieze M. E. J., Rubinsztein-Dunlop H., Gold J., Hagberg P., Hanstorp D.
Optically driven micromachine elements.
Appl. Phys. Lett. 78: 547-549 (2001)
- [Fuhr 1998] Fuhr G., Schnelle Th., Müller T., Hintzler H., Monajembashi S., Greulich K.-O.
Force measurements of optical tweezers in electro-optical cages
Appl. Phys. A 67: 385-390 (1998)
- [Gahagan 1998] Gahagan K.T.
Optical manipulation of microparticles and biological structures.
Ph.D. Thesis – Worcester Polytechnic Institute, Faculty of Physics (1998)

- [Galajida 2001] Galajida P., P. Ormos
Complex micromachines produced and driven by light.
Appl. Phys. Lett. 78: 249-251 (2001)
- [Galneder 2001] Galneder R., Kahl V., Arbuzova A., Rebecchi M., Rädler J. O., McLaughlin S.
Microelectrophoresis of a bilayer-coated silica bead in an optical trap: application to enzymology.
Biophys. J. 80: 2298-2309 (2001)
- [Gauthier 1997] Gauthier R.C.
Theoretical investigation of the optical trapping force and torque on cylindrical micro-objects.
J. Opt. Soc. Am. B 14: 3323-3333 (1997)
- [Gauthier 1997] Gauthier R.C.
Theoretical investigation of the optical trapping force and torque on cylindrical micro-objects.
J. Opt. Soc. Am. B 14: 3323-3333 (1997)
- [Gauthier 1999a] Gauthier R. C., Ashman M., Frangioudakis A., Mende H., Ma S.
Radiation-pressure-based cylindrically shaped microactuator capable of smooth, continuous reversible and stepped rotation.
Appl. Opt. 38: 4850-4860 (1999)
- [Gauthier 1999b] Gauthier R.C., Ashman M., Grover C.P.
Experimental confirmation of the optical-trapping properties of cylindrical objects.
Appl. Opt. 38: 4861-4869 (1999)
- [Grover 2000] Grover S.C., Gauthier R.C., Skirtach A.G.
Analysis of the behaviour of erythrocytes in an optical trapping system.
OPTICS EXPRESS 13: 533-539 (2000)
- [Guilford 1997] Guilford H. W., Dupuis D. E., Kennedy G., Wu J., Patlak J. B., Warshaw D. M.
Smooth muscle and skeletal muscle myosins produce similar unitary forces and displacements in the laser trap.
Biophys. J. 72: 1006-10021 (1997)
- [Harada 1996] Harada Y., Asakura T.
Radiation forces on a dielectric sphere in the Rayleigh scattering regime.
Opt. Comm. 124: 529-541 (1996)
- [Harada 1999] Harada Y., Funatsu T., Murakami K., Nonoyama Y., Ishihama A., Yanagida T.
Single-molecule imaging of RNA polymerase-DNA interactions in real time.
Biophys. J. 76: 709-715 (1999)
- [Hatfield 1999] Hatfield J. W., Quake S. R.
Dynamic properties of an extended polymer in solution.
Phys. Rev. Lett. 82: 3548-3551 (1999)
- [Hénon 1999] Hénon S., Lenormand G., Richert A., Gallet F.
A new determination of the shear modulus of the human erythrocyte membrane using optical tweezers.
Biophys. J. 76: 1145-1151 (1999)

- [Higurashi 1994] Higurashi E., Ukita H., Tanaka H., Ohguchi O.
Optically induced rotation of anisotropic micro-objects fabricated by surface micromachining.
Appl. Phys. Lett. 64: 2209-2210 (1994)
- [Higurashi 1998] Higurashi E., Sawada R., Ito T.
Optically induced rotation of a trapped micro-object about an axis perpendicular to the laser beam axis.
Appl. Phys. Lett. 72: 2951-2953 (1998)
- [Ishijima 2001] Ishijima A., Yanagida T.
Single molecule nanobioscience.
TRENDS in Biochemical Sciences 26: 438-444 (2001)
- [Kawai 2000] Kawai M., Kawaguchi K., Saito M., Ishiwata S.
Temperature change does not affect force between single actin filaments and HMM from rabbit muscles.
Biophys. J. 78: 3112-3119 (2000)
- [Kitamura 1999] Kitamura, K.
A single myosin head moves along an actin filament with regular steps of 5.3 nanometres.
Nature 397: 129-134 (1999)
- [Knight 2001] Knight A. E., Veigel C., Chambers C., Molloy J.
Analysis of single-molecule mechanical recordings: application to acto-myosin interactions.
Progress in Biophysics & Molecular Biology 77: 45-72 (2001)
- [König 1995a] König K., Liu Y., Sonek G.J., Berns M.W., Tromberg B.J.
Autofluorescence spectroscopy of optically trapped cells.
Photochem. Photobiol. 62: 830-835 (1995)
- [König 1995b] König, K., Liang H., Berns M. W., Tromberg B. J.
Cell damage by near-IR microbeams.
Nature 377: 20-21 (1995)
- [König 1996] König K., Liang H., Berns M.W., Tromberg B.J.
Cell damage in near-infrared multimode optical traps as a result of multiphoton absorption.
Opt. Lett. 21: 1090-1092 (1996)
- [Kuo 1993] Kuo S.C., Sheetz M.P.
Force of single kinesin molecules measured with optical tweezers.
Science 260: 232-234 (1993)
- [Kusumi 1998] Kusumi A., Sako Y., Fujiwara T., Tomishige M.
Application of laser tweezers to studies of the fences and tethers of the membrane skeleton that regulate the movements of plasma membrane proteins.
Methods in cell biology 55: 174-192 (1998)
- [Larson 1997] Larson R. G., Perkins T. T., Smith D. E., Chu S.
Hydrodynamics of a DNA molecule in a flow field.
Phys. Rev. E 55: 1794-1797 (1997)
- [Liang 1993] Liang H., Wright W.H., Cheng S., Wei H. Berns M.W.
Micromanipulation of Chromosomes in PTK2 cells using laser microsurgery (optical scalpel) in combination with laser-induced optical force (optical tweezers).
Exper. Cell Res. 204: 110-120 (1993)

- [Liang 1996] Liang, H., Vu K. T., Krishnan P., Trang T. C., Shin D., Kimel S., Berns M. W.
Wavelength dependence of cell cloning efficiency after optical trapping.
Biophys. J. 70: 1529-1533 (1996)
- [Liu 1995a] Liu, Y., Cheng D. K., Sonek G. J., Berns M. W., Chapman C. F., Tromberg B. J.
Evidence for localized cell heating induced by infra-red optical tweezers.
Biophys. J. 68: 2137-2144 (1995)
- [Liu 1995b] Liu, Y., Sonek G. J., Berns M. W., König K., Tromberg B. J.
Two-photon fluorescence excitation in continuous-wave infrared optical tweezers.
Opt. Lett. 20: 2246-2248 (1995)
- [Liu 1996] Liu Y., Sonek G. J., Berns M.W., Tromberg B.J.
Physiological monitoring of optically trapped cells: assessing the effects of confinement by 1064-nm laser tweezers using microfluorometry.
Biophys. J. 71: 2158-2167 (1996)
- [Maia Neto 2000] Maia Neto P.A., Nussenzveig H.M.
Theory of optical tweezers.
Europhys.Lett. 50: 702 -708 (2000)
- [Mammen 1996] Mammen M., Helmerson K., Kishore R., Choi S.-K., Phillips W.D., Whitesides G.M.
Optically controlled collisions of biological objects to evaluate potent polyvalent inhibitors of virus-cell adhesion.
Chemistry & Biology 3: 757-763 (1996)
- [Mehta 1998] Mehta A.D., Finer J.T., Spudich J.A.
Reflections of a lucid dreamer: optical trap design considerations.
Methods in cell biology 55: 47-68 (1998)
- [Meiners 2000] Meiners J.-C., Quake S. R.
Femtonewton force spectroscopy of single extended DNA molecules.
Phys. Rev. Lett. 84: 5014-5017 (2000)
- [Neuman 1999] Neuman K.C., Chadd E.H., Liou G.F., Bergman K., Block S.M.
Characterization of photodamage to *Escherichia coli* in optical traps.
Biophys. J. 77: 2856-2863 (1999)
- [Nieminem 2001] Nieminen T.A., Rubinsztein-Dunlop H., Heckenberg N.R.
Calculation and optical measurement of laser trapping forces on non-spherical particles.
J. Quantit. Spectr. & Radiative Transfer 70: 627-637 (2001)
- [Nishizaka 1995] Nishizaka T., Miyata H., Yoshikawa H., Ishiwata S., Kinosita K. Jr.
Unbinding force of a single motor molecule of muscle measured using optical tweezers.
Nature 377: 251-254 (1995)
- [Paterson 2001] Paterson L., MacDonald M. P., Arlt J., Sibbett W., Bryant P. E., Dholakia K.
Controlled rotation of optically trapped microscopic particles.
Science 292: 912-914 (2001)
- [Richard 1959] Richards B., Wolf E.
Electromagnetic diffraction in optical systems.
Proc. R. Soc. A 253: 358- (1959)

- [Roosen 1979] Roosen G.
La levitation optique de sphere.
Can. J. Phys. 57: 1260-1279 (1979)
- [Sako 1998] Sako Y., Nagafuchi A., Tsukita S., Takeichi M., Kusumi A.
Cytoplasmic regulation of the movement of E-cadherin on the free cell surface as studied by optical tweezers and single particle tracking: corraling and tethering by the membrane skeleton.
J. of Cell Biol. 140: 1227-1240 (1998)
- [Saloma 1995] Saloma C., Cambaliza M. O.
Single-Gaussian-beam interaction with a dielectric microsphere: radiation forces, multiple internal reflections, and caustic structures.
Appl. Opt. 34: 3522-3528 (1995)
- [Schütze 1994] Schütze K., Clement-Sengewald A., Ashkin A.
Zona drilling and sperm insertion with combined laser microbeam and optical tweezers.
Fert. Ster. 61: 783-786 (1994)
- [Schütze 1998] Schütze K., Posl H., Lahr G.
Laser micromanipulation systems as universal tools in cellular and molecular biology and in medicine.
Cellular and Molecular Biology 44: 735-746 (1998)
- [Shikano 1999] Shikano S., Horio K., Ohtsuka Y.
Separation of a single cell by red-laser manipulation.
Appl. Phys. Lett. 75: 2671-2673 (1999)
- [Shingyoji 1998] Shingyoji C., Higuchi H., Yoshimura M., Katayama E., Yanagida T.
Dynein arms are oscillating force generators.
Nature 393: 711-714 (1998)
- [Sleep 1999] Sleep J., Wilson D., Simmons R., Gratzer W.
Elasticity of the red cell membrane and its relation to hemolytic disorders: an optical tweezers study.
Biophys. J. 77: 3085-3095 (1999)
- [Spudich 1990] Spudich J.A.
Motor molecules in motion.
Nature 348: 284-285 (1990)
- [Svoboda 1993] Svoboda K., Schmidt C.F., Schnapp B.J., Block S.M.
Direct observation of kinesin stepping by optical trapping interferometry.
Nature 365: 721-727 (1993)
- [Svoboda 1994] Svoboda K., Block S.M.
Biological application of optical forces.
Annu. Rev. Biophys. Biomol. Struct. 23: 247-285 (1994)
- [Tashiro 1993] Tashiro H., Uchida M., Sato-Maeda M.
Three-dimensional cell manipulator by means of optical trapping for the specification of cell-to-cell adhesion.
Opt. Eng. 32: 2812-2817 (1993)
- [Tlusty 1998] Tlusty T., Meller A., Bar-Ziv R.
Optical gradient forces of strongly localized fields.
Phys. Rev. Lett. 81: 1738-1741 (1998)
- [Tsuda 1996] Tsuda Y., Mashimo T., Yoshiya I., Kaseda K., Harada Y., Yanagida T.
Direct Inhibition of the actomyosin motility by local anesthetics in vitro. *Biophys. J.*, 71: 2733-2741 (1996)

- [Ukita 1997] Ukita H., Nagatomi K.
Theoretical demonstration of a newly designed micro-rotator driven by optical pressure on a light incident surface.
Opt. Rev. 4: 447-449 (1997)
- [Ukita 1997] Ukita H., Nagatomi K.
Theoretical demonstration of a newly designed micro-rotator driven by optical pressure on a light incident surface.
Opt. Rev. 4: 447-449 (1997)
- [Visscher 1992a] Visscher K., Brakenhoff G.J.
Theoretical study of optically induced forces on spherical particles in a single beam trap I: Rayleigh scatterers.
Optik 89: 174-180 (1992)
- [Wang 1998] Wang M.D., Schnitzer M.J., Yin H., Landick R., Gelles J., Block S.M.
Force and velocity measured for single molecules of RNA polymerase
Science 282: 902-907 (1998)
- [Wright 1994] Wright W.H., Sonek G.J., Berns M.W.
Parametric study of the forces on microspheres held by optical tweezers.
Appl. Opt. 33: 1735-1748 (1994)
- [Xiaobing 2000] Xiaobing C., Berg H.C.
Torque-speed relationship of the flagellar rotary motor of *Escherichia coli*.
Biophys. J. 78: 1036-1041 (2000)
- [Yin 1995] Yin H., Wang M.D., Svoboda K., Landick R., Block S.M., Gelles J.
Transcription against an applied force.
Science 270: 1653-1657 (1995)

2.1 Construction of optical tweezers

2.1.1 General optical trap design considerations

*optical tweezers
based on com-
mercial micro-
scopes*

*custom-
microscope opti-
cal tweezers*

The steep three-dimensional electric field gradient required for optical trapping is created by focusing a laser beam through a lens with high numerical aperture, usually a microscope objective. In order to take advantage of the imaging techniques conventionally used in microscopes, as for example *differential interference contrast* (DIC), *phase contrast* and *epifluorescence*, many optical tweezers are usually built by employing a conventional research level microscope (Fig. 2.1). In such configurations, the focusing and imaging optics are entirely integrated into the microscope. Microscope-integrated optical tweezers are particularly suited for biological applications, where high image quality is required. The trapping laser beam, expanded and, if necessary, reshaped for astigmatic correction, is usually coupled into the microscope through the epifluorescence port (Fig. 2.1). If high image quality is not a concern, building a custom optical tweezers set-up by assembling the different mechanical and optical elements on a damped anti-vibration table may be a convenient alternative. A principal advantage with a custom optical tweezers is that the loss of laser power associated with absorption or reflection by lenses, mirrors and other elements is minimized because only the optics necessary for trapping are used in the set-up. Additionally, a custom set-up allows for easy suppression of mechanical noise by improving the mechanical stability of the set-up.

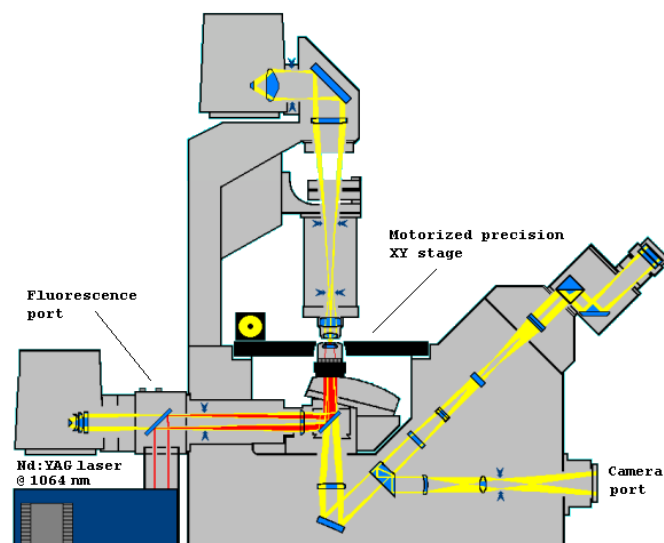


FIGURE 2.1 Commercial microscope-based optical tweezers.

The power required for optically trapping of micrometer or sub-micrometer dielectric particles ranges between 10 and 1000 mW, producing a huge energy flux between 10^6 and 10^8 W/cm² in the focal plane. In many cases the lasers used for trapping are continuous-wave lasers with a wavelength usually in the near infrared range, in order to avoid sample damage due to absorption. Indeed, it is well known that water has a reduced absorption in the wavelength range between 700-1000 nm (Fig. 2.1).

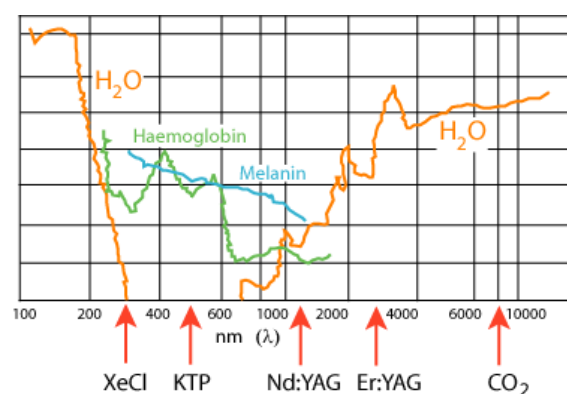


FIGURE 2.2 Optical absorption spectra of the main chromophores in biological tissues (water, haemoglobin, melanin). Different laser lines are also shown.

Moreover, the chromophores present in biological specimens, such as cells or bacteria, absorb in the UV and visible range, but much less in the near-infrared region, as also shown in Fig. 2.2.

choice of the laser

A list of lasers often employed in optical trapping is given in Table 2.1.

Laser type	TEM ₀₀ power	Wavelength
ND:YAG ND:YLF	100 mW-10 W	1064 nm 1047, 1057 nm
Ti:sapphire	2 W	650-1100 nm continu- ous tunable
Laser diode	5-250 mW	780-1020 nm

TABLE 2.1 Lasers and wavelengths used for optical trapping (adapted from SVOBODA 1994a).

Solid-state lasers provide good stability and a clean TEM₀₀ beam profile. The characteristic wavelength of 1064/1047 nm is sufficiently far away from the absorption bands of biological chromophores and the water absorption peaks, allowing to avoid optical damage of the samples. A good alternative to Nd:YAG or Nd:YLF lasers are diode lasers, which are inexpensive and compact. Typical wavelengths of these lasers are 785, 820, 900 nm. A disadvantage of diode lasers is the astigmatism and high divergence of the output beam. Therefore, correcting optics (like a pair of anamorphic prisms) is normally used to circularize the beam. Correction and collimation of a diode laser beam using a single aspheric lens is also reported in the literature [Bakker Schut 1993]. New laser diodes with high power (up to 150 mW) and integrated beam-correcting optics in the laser head are now available (for example CirculaserTM by BlueSky Research). The integrated correcting optics ensures a non-astigmatic and circular wavefront. Tunable Ti:sapphire lasers operating in the 700 nm through 1100 nm range are farther away from water absorption lines than the 1064 nm Nd:YAG laser. At a given power, they provide a stronger trap and reduced laser-induced cell damage relative to a Nd:YAG laser [Berns 1992], but are rarely used in optical trapping due to their high cost. Next to the laser, the choice of the objective lens is a critical point in designing optical tweezers. The laser beam must be focused to a diffraction-limited spot in order to achieve optical trapping. Thus, a very important parameter considered when choosing an objective is its numerical aperture (N.A.). The numerical aperture determines the light-gathering power of a lens and is defined as:

choice of the objective

$$\text{N.A.} = n \sin \alpha \quad (2.1)$$

effects of chromatic and spherical aberration

chromatic aberration

Where n is the refractive index of the working medium of the lens, and α is the half angle of the cone subtended by the lens as seen from the focus. The larger the angle α , the larger is the cone of light collected by the lens. The numerical aperture has to be as high as possible for optimal trapping efficiency. For oil-immersion objectives, N.A. values up to 1.56 are possible, while air-immersion lenses cannot have a N.A. larger than one. Slightly overfilling the back aperture of the objective by the Gaussian beam leads to a narrower focus and a steeper intensity gradient in all directions, which results in a stronger gradient force of the trap. Attention must also be paid to optical aberrations of the objective. Commercial microscope objectives are usually corrected for *spherical* and *chromatic aberration* in the UV and visible wavelength regions, but not in the infrared region of the spectrum. Consequently, a certain degree of both spherical and chromatic aberration will affect the quality of the focal spot produced by an infrared laser beam passing through an objective. Longitudinal *chromatic aberration* is the variation of focus (or image position) with wavelength. In general, the refractive index of optical materials is larger for short wavelengths than for long wavelengths. Hence, the short wavelengths are more strongly refracted at each surface of a lens, as shown in Fig. 2.3. The distance along the optical axis between the two focal points is called the longitudinal (or axial) chromatic aberration. An effect of chromatic aberration is that an infrared laser beam is focused at a position slightly above the image plane of the objective (Fig. 2.3). This has implications for the proper alignment of the optical trap: for perfectly aligning the trapping plane and the image plane in optical tweezers, the infrared laser beam should be made slightly divergent before being introduced into the objective.

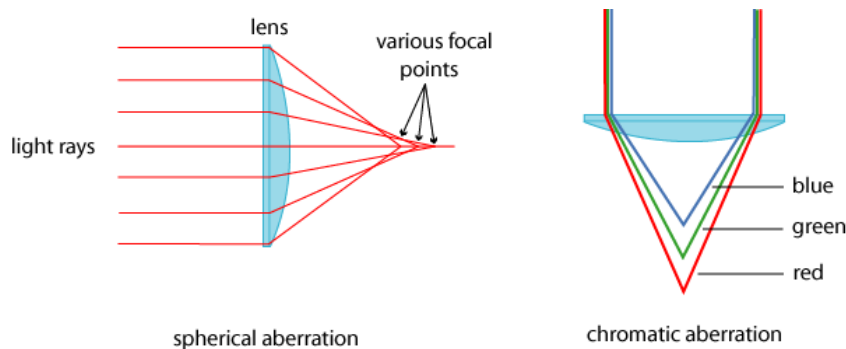


FIGURE 2.3

Effects of spherical and chromatic aberration.

spherical aberration

Spherical aberration (see Fig. 2.3) occurs when light rays passing through the periphery of a lens are focused at a different position than rays passing closer to the center. This is the case for spherical lenses. Modern high quality microscope objectives are well corrected for chromatic and spherical aberration at up to four wavelengths. The corrections available in different objective types are summarized in Table 2.2.

objective type	chromatic	spherical
achromat	blue red	blue red
plan achromat	blue red	blue red
fluorite	blue green red	blue green red
semiapochromat	blue green red	blue green red
apochromat	dark blue blue green red	dark blue blue green red

source: M.W.Davidson, M. Abramowitz - Optical microscopy - URL: www.microscopy.fsu.edu

TABLE 2.2 Aberration corrections of different objectives types.

The objective used in the set-up presented here is a Plan-Neofluar by *Zeiss* (100×, 1.4 N.A. oil immersion). This objective is a semiapochromat with fluorite optics, corrected at three wavelengths (blue, green, red) in both chromatic and spherical aberration. The objective has also flat field correction (*Plan*). Unfortunately, the objective is not corrected for spherical aberration in the infrared range. An undesirable effect of spherical aberration is that the focus spreads into a cylindrical shape along the optical axis, creating multiple traps along the axial direction [Rohrbach 2001]. This can lead to anomalous behavior when measuring the Brownian motion of a trapped microsphere (see Paragraph 3.2.4.3). Spherical aberration is particularly evident when imaging with oil-immersion objectives into a solution, due to the refractive index mismatch between the immersion oil ($n=1.55$) and the solution (usually water, $n=1.33$). Better focusing performance is obtained with water immersion objectives which provide a sharp diffraction-limited focus spot even far away from the glass/solution interface. An additional problem with standard objectives is the high loss of laser power, due to their limited light transmission (around 40% light loss) [Svoboda 1994] (see also Par. 2.2.1). Indeed, the lenses inside the objective have no anti-reflective coatings for light at infrared wavelengths.

2.1.2 Description of the optical set-up

A CAD draw of the optical tweezers set-up developed in this work is shown in Fig. 2.4. The set-up is built by assembling custom mechanical and optical components on an optical bench. It works similarly to an inverted microscope. As already mentioned in Paragraph 2.1.1, the advantage of a custom-assembled set-up is the better control of environmentally generated mechanical vibrations. The trapping laser (LCS-DTL-22, Laser Compact, Moscow) operates at a wavelength of 1064 nm and has a maximum cw output power of 320 mW. The beam has a TEM₀₀ propagation mode, a linear polarization, and its diameter is 1.8 mm at $1/e^2$ at the laser head exit.

The beam is directed towards a telescope system (Fig. 2.4 lenses **L1** and **L2**) by two gold mirrors (**M1** and **M2**) mounted on two adjustable holders at 45°. The 3× Galileian telescope system (details in Fig. 2.5) is constituted of a concave lens (**L1**, focal length = -40 mm) mounted on a XY-cage (LINOS Photonics, Germany) and an achromatic doublet lens (**L2**, focal length = 120 mm). The lenses are mounted on an optical rail system and their relative position can be shifted manually for coarse adjustment or by using a micrometer-screw for fine adjustment. The telescope expands the laser beam to a diameter of about 5.4 mm. After the telescope, the beam is not collimated but slightly divergent in order to compensate the effect of chromatic aberration (see Paragraph 2.1.1). During the alignment of the optical trap, the optimal beam divergency can be changed by varying the distance between **L1** and **L2**. The beam is subsequently brought to the rear pupil of the objective by a dichroic mirror (**DIC**) (660DRLP XF2023, Omega Opticals). The objective (Zeiss Neofluar, 100×, N.A. = 1.4, infinity corrected, oil immersion) is mounted on a piezoelectric focusing unit (PIFOC, Physik Instrumente, Germany - not shown in Fig. 2.4) which allows trap positioning along the optical axis with nanometer precision. The piezoelectric element itself is mounted on a mechanical precision translating stage (HV 60 12, Owis, Germany) used for coarse axial positioning of the trap. The objective focuses the laser beam into the microscope chamber containing the sample. Sample positioning within the *xy*-plane is accomplished by a precision mechanical motorized translation table (Märzhäuser, Wetzlar, Germany) not shown in Fig. 2.4). This *xy*-table can be manually controlled with a joystick or automatically through a personal computer.

The stage controller allows a (nominal) step resolution of 25 nm. In practice, reliable step resolution of 0.1 μm is achievable. The sample is imaged by a monochrome CCD videocamera (FK 7512 IQ, Pieper GmbH, Germany). The light from the objective is re-directed to the tube lens **L3** (achromatic doublet, focal length = 160 mm) by the cold mirror **CM2** (cold mirrors reflect visible and pass IR light), which forms a real image on the CCD-chip. The video signal from the camera is digitized by a frame-grabber (Scion Corporation) and visualized with the public domain video-processing software *Scion Image* (www.scion.com) (derived from the program *NIH Image*, originally written for Apple by the American National Institutes of Health). The laser light that is back-scattered by the sample passes the dichroic mirror **DIC** and is collected by the lens **L4** (focal length = 250 mm), which focuses the light onto a segmented position-sensitive photodiode (**PSD** – see Paragraph 2.1.4). Additional characteristics of the set-up are described in Chapter III.

2.1.3 Optical tweezers alignment procedure

Alignment of optical tweezers is straightforward: the laser beam is just expanded and injected into the objective, without using any steering system. Translation is accomplished by moving the sample, while the trap remains stationary. Nevertheless, despite the simplicity of the system, some critical steps like adjusting of the trap position in the image plane can be somewhat troublesome and tricky. Since the laser has a wavelength in the IR wavelength range, an IR-sensitive fluorescent card is used to visualize the beam. The first step is the alignment of the laser beam along the optical axis across the telescope system. To this end, the lenses **L1** and **L2** and the objective are removed and two iris diaphragms are introduced at the opposite sides of the optical rail system (after the mirror **M1** and before the mounting cube below the objective, respectively). Maintaining the iris half-opened, a rough beam alignment is done by moving the mirrors **M1** and **M2** that are mounted on two adjustable mirror holders. Next, the iris diaphragms are progressively closed and the beam alignment improved by moving the two mirrors until the beam is perfectly on-axis. Subsequently, the angle of the dichroic mirror **DIC** is set exactly at 45° with respect to the optical axis of the telescope. Precision adjustment of the dichroic mirror is achieved by replacing the objective with a custom designed aligning tool, an aluminum tube that is screwed on the objective holder, while its opposite side is connected with an iris diaphragm. The tube is about 300 mm long. Adjustment is further improved by

placing a 10× objective onto the objective holder and carefully adjusting the dichroic mirror holder until a perfectly symmetric spot appears on the fluorescent card placed over the objective. The same procedure is repeated with a 40× objective. Finally, the objective used for optical trapping is inserted, a drop of the immersion medium (immersion oil) is added on the front lens, and a cover-slip is placed on top. The trap alignment is now continued by using the CCD camera. By displacing the objective along the optical axis, a bright spot (corresponding to the laser focus) in the center of the image must appear on the monitor. The beam adjustment can be tested by moving the focus up and down and checking the symmetry of the image spot during focusing and defocusing. A residual spot asymmetry can be corrected by carefully moving the lens **L1** with the *xy*-cage. Subsequently, a diluted aqueous suspension of 10 μm -beads is added on the cover-slip for the final alignment. Attraction of the beads toward the focus and trapping should be now already observable, but the trapped beads will likely be out-of-focus at this stage. This means that the trapping and image plane do not yet coincide. This can be accomplished by slowly moving the tube lens **L3** until a sharp image of the trapped bead appears on the monitor. Alternatively, the distance between lenses **L1** and **L2** can be varied by carefully acting on the on-axis micrometer-screw connected with lens **L1** (Fig. 2.5). That changes the divergence of the expanded beam, resulting in a translation of the trap position along the optical axis. This is the most difficult step in trap alignment, an experience-requiring trial-and-error procedure.

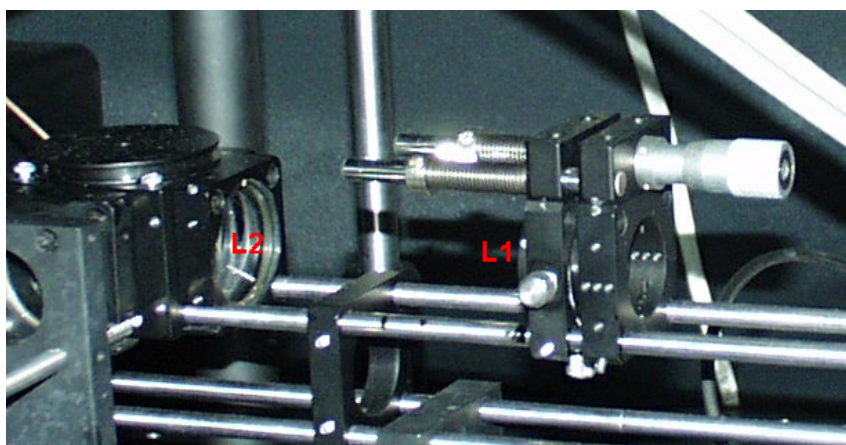


FIGURE 2.5

Telescope system.

2.1.4 High-resolution position measurement techniques

monitoring the position of a trapped probe with a CCD chip

Converting optical tweezers into a sensitive micromechanical force transducer that is capable of exerting and/or measuring forces in the pN range requires monitoring of the position of the probe with high spatial (nm range) and temporal (msec range) resolution. A feasible approach for achieving this is to image the probe onto a CCD-chip. Information about its position is extracted by digitizing each frame and using tracking algorithms [Crocker 1996]. However, this approach has some limitations. A CCD-camera is a digital device consisting of an array of closely spaced photodiodes. Light is recorded as an electric charge in each diode, and the accumulated charges are subsequently read out sequentially. The read-out frequency is in the range from some kHz up to several MHz. However, the temporal „bottle neck“ is actually determined by the so-called *frame rate*, which lies in the range between 30 and 100 frames/sec (corresponding to a temporal resolution of 10-30 msec/frame) for conventional CCD cameras, which is often insufficient for obtaining information about the mechanical properties of a system. Cameras with higher frame rate (up to 10^3 frames/sec) are also commercially available (for example from Photron Ltd., www.photron.com), but are by an order of magnitude more expensive than conventional CCD-cameras. A further constraint of CCD-cameras is their limited dynamic range.

position sensing detectors (PSDs)

An alternative to CCD-cameras are analog photodetectors, such as position-sensitive photodiodes. Position sensitive detectors (PSD's) are special *PIN silicon photodiodes* (Fig 2.6) that allow for a precise measurement of small positional changes of a light beam. Unlike discrete-element devices such as CCD-chips, PSD's are analog devices producing a continuous measurement signal which can be used to simultaneously monitor position and light intensity of a light beam. The advantages of PSD's are high spatial sensitivity, high intrinsic frequency bandwidth (in MHz range), high dynamic range, and good position linearity. Moreover, they are low-cost components and require only simple analog operating circuits. The most common applications of PSD's are in laser beam aligners, targeting and pointing devices, and displacement and vibration monitors. Noteworthy, PSD's are employed in scanning-probe microscopes to monitor the position of the cantilever, and also in the tracking systems of CD-players and CD-ROM optical pick-ups (see Chapter IV).

Types of position sensitive detectors. a) lateral-

There are two types of position sensitive detectors: *lateral-effect* PSD's and *segmented* (bi- and four-quadrants) PSD's.

effect PSD's

A *lateral-effect photodiode* uses a continuous, single-element doped disc of silicon with electrodes connected equidistantly around its perimeter. There are no gaps or dead areas on the photodiode's surface. When a light spot is imaged onto the surface of a lateral-effect PSD, an electric charge is generated that is proportional to the light energy at the position of incidence. The generated electric charge is transferred through the resistive *p*-layer and collected by electrodes: since the resistivity of the *p*-layer is uniform, the photocurrent measured by an electrode is inversely proportional to the distance between the incident position and the electrode (Fig. 2.6a). The number of electrodes is **two** in *mono-dimensional* PSD's (which can monitor displacements only along one axis) and **four** in *two-dimensional* PSD's (which allow displacement monitoring both along *x*- and *y*-axis).

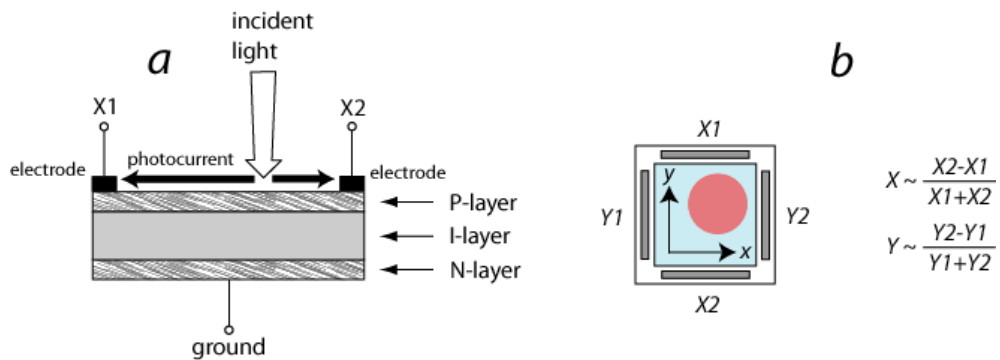


FIGURE 2.6 Monitoring x,y displacements with a duo-lateral PSD.

Lateral effect PSD's can determine light spot positions across the entire sensing area without any dead zones. The current output is directly proportional to the position of the part of the light spot that is imaged onto the active area of the detector. An important point is that the response of lateral effect PSD's is not influenced by the size or shape of the light image as long as this image remains within the active area of the detector. Moreover, operation far from the optical center (null point) of the system does not affect the accuracy of the position determination.

b) segmented PSD's

Segmented PSD's are a combination of two or four photodiodes separated by (typically) 30 μm wide gaps. The gaps are "dead areas", insensitive to incident light. Thus, the part of the light spot incident onto the gap region does not contribute to the photocurrent. A symmetric light spot centered on a four-quadrant photodiode will generate equal amounts of photo-current in each of the four sectors. If the beam is moved off the center of the PSD, the current from the four sectors changes. The *x*- and *y*-displacements relative to

the center can be estimated by processing the signal from each quadrant as outlined in Fig. 2.7. Signal processing can be performed by a software algorithm, or directly by a analog circuit as done in this work.

$$X = \frac{(Q1+Q4)-(Q2+Q3)}{Q1+Q2+Q3+Q4}$$

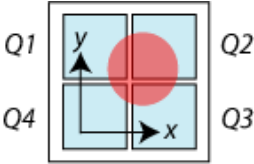
$$Y = \frac{(Q1+Q2)-(Q3+Q4)}{Q1+Q2+Q3+Q4}$$


FIGURE 2.7 Monitoring x,y -displacements with a segmented four-quadrant PSD.

When using a four-quadrant photodiode, some constraints have to be considered. First, the incident light spot must be smaller than the detector's total active area, but larger than the gap between individual active areas. Second, the total positional detection range is limited to the incident light spot size or the detector's active area, whichever is smaller. As illustrated in Fig. 2.8, the detection range increases with spot size, while positional accuracy decreases, because a given movement of a small spot creates a much bigger differential signal than the same movement of a larger spot. Segmented PSD usually show a very even responsivity of all their four segments. Due to this even responsivity, these PSD's have a higher accuracy than lateral-effect PSD's, and display excellent stability over time and with varying temperature. Moreover, since the positional resolution is independent on the SNR of the system, as it is in lateral-effect PSD's, light detection at very low intensity levels is possible.

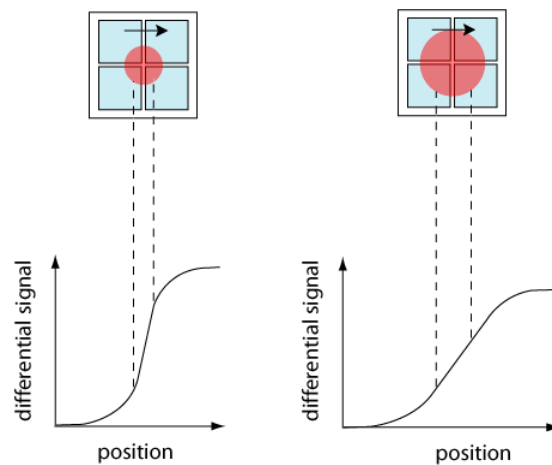


FIGURE 2.8 Detection range and positional accuracy vs. spot size.

With PSD's, high spatial (nm-range) and temporal (msec-range) resolution is achievable.

PSD's modes of operation

In general, a silicon photodiode can be operated either in *photoconductive* or *photovoltaic* mode (Fig. 2.9). A photodiode working in the photoconductive mode has a *reverse-biased voltage* (V_R), which is applied across the photo-sensitive element. In contrast, a photodiode working in the photovoltaic mode has no voltage potential across the element or, in other words, is *zero-biased*.

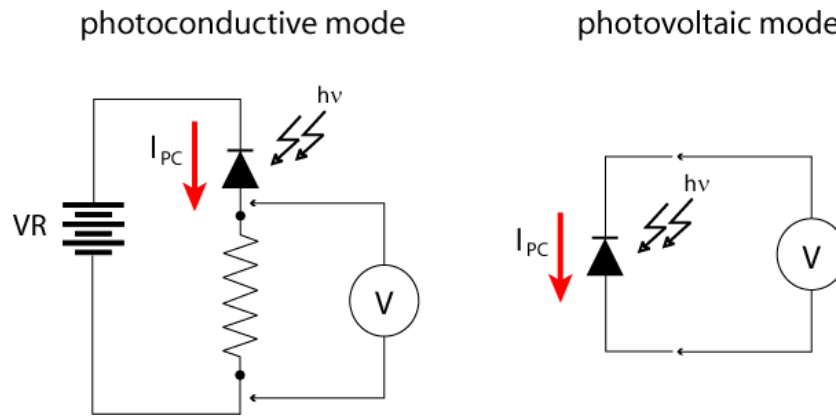


FIGURE 2.9

Typical silicon photodiode circuit modes of operation.

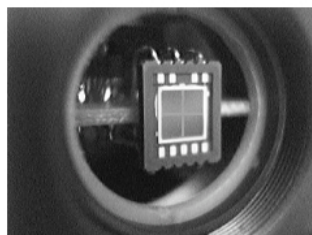
Each mode has its own advantages and disadvantages. When a reverse-biased voltage is applied across the photodetector, the width of the depletion region is reduced, which significantly reduces the *parasitic capacitance* (C_{PD}) of the photodiode. A reduced parasitic capacitance facilitates high speed operation. However, in photoconductive mode the generation of a dark current (I_d) in the form of *drift-current* is enhanced. In contrast, the dark current is minimal in the photovoltaic mode, constituted only by *Johnson* (or thermal) current due to thermal generation of carriers and surface leakage (see Paragraph 2.1.7). The photodiode operated in photovoltaic mode has better light sensitivity and photocurrent linearity. Thus, this mode is preferred for precision applications, whereas the photoconductive mode is employed particularly whenever a very fast response time ($>2.8 \mu\text{sec}$) is required. Further details on PSD's can be found in the technical documentation provided by Hamamatsu Photonics and UDT sensors (www.udt.com - photodiode characteristics; www.usa.hamamatsu.com).

In this work, a four-quadrant PSD was integrated into the optical tweezers

set-up. The detector (S5980, Hamamatsu – Fig. 2.10) has a wide spectral sensitivity ranging from 320 nm up to 1100 nm and is well suited for detecting the 1064 nm radiation emitted by the Nd:YAG laser (Fig. 2.10). Some relevant electrical and optical characteristics of this PSD are reported in Table 2.2. The PSD was operated in photovoltaic mode.

Parameter	Value
Active area	5 x 5 mm
Spectral response range (λ)	320 to 1100 nm
Peak sensitivity wavelength	960 nm
Bandwidth	20 MHz
Responsivity (\mathfrak{R})	0.72 Amps / Watt @ $\lambda=960$ nm

TABLE 2.2 Features of the segmented PSD S5980 from Hamamatsu.



Hamamatsu S5980

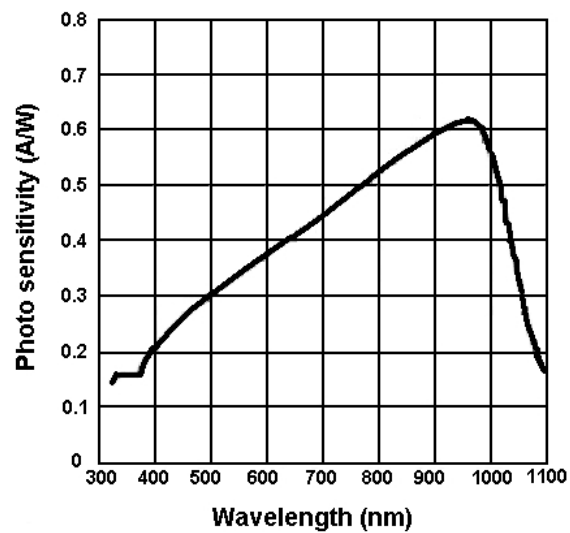


FIGURE 2.10 Spectral response of the S5980 from Hamamatsu.

2.1.5 PSD's signal conditioning

step (a): current-to-voltage converter

As seen in Paragraph 2.1.4, each of the four elements of the PSD converts the incident light into an electric current (photocurrent) in the range between 4-20 mA. Subsequently, these four photocurrents are processed as follows: (1) they are converted into voltage signals and amplified, then (2) processed by an analog circuit in order to yield the corresponding x -, y - and z -displacement values, and finally (3) digitized and recorded on a PC for data analysis. Steps (1) and (2) are accomplished by a custom-built analog electronics board. A preamplifier converts the photodiode current to a voltage (current-to-voltage converter). The current-to-voltage converter circuit is a critical part of a photo-sensing device, and its implementation has to take into account issues like noise control, stability, gain and bandwidth. The most straightforward approach for designing a precision photo-sensing circuit is to place the photodiode at the input of an operational amplifier (op-amp), putting a resistor (R_F) in the feedback loop. The basic configuration of such a circuit is shown in Fig. 2.11.

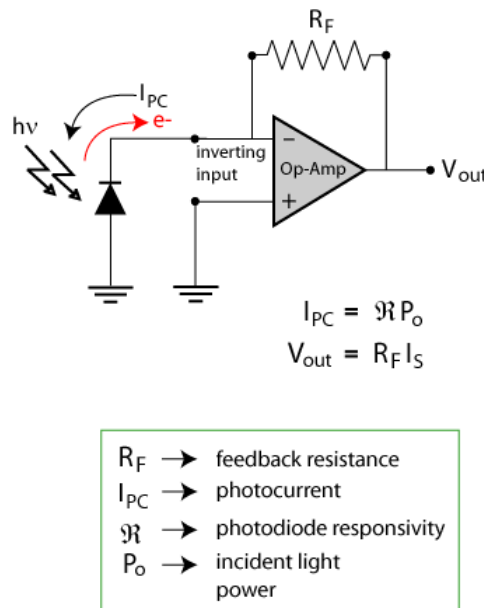


FIGURE 2.11 Photodiode current-to-voltage converter.

The incident light causes a current flow (I_{PC}) through the diode from the cathode to the anode (see Fig. 2.11). Since the input impedance of the inverting input of the op-amp is extremely high, the current generated by the photodiode flows through the feedback resistor, R_F . Therefore, a current-to-

preamplifier

voltage converter is also called a *transimpedance amplifier*. The op-amp keeps the inverting and the non-inverting input at the same potential; consequently, the output voltage changes proportionally to the voltage drop across the resistor, R_F , since the potential of the non-inverting input is zero (ground). The amplification system shown in figure Fig. 2.11 converts the current of the photodiode to a voltage proportional to:

$$V_{OUT} \propto -(R_F I_{PC}) \quad (2.1)$$

$$\text{with } I_{PC} = \Re P_0, \quad (2.2)$$

where:

V_{OUT} – is the voltage output of the operational amplifier (V);

R_F – is the feedback resistor in the amplifier circuit (Ω);

I_{PC} – is the photocurrent produced by the photodiode (A).

\Re – is the photodiode responsivity (A/W)

P_0 – is the incident light power (W)

preamplifier circuit imple- mentation

The current-to-voltage converter developed in this work was implemented on the basis of the op-amp LT1114 by Linear Technology, a quadruple FET input op-amp (each unit includes four single op-amps), which has very low voltage (typ. 16 nV/ $\sqrt{\text{Hz}}$) and current noise (typ. 0.08 pA/ $\sqrt{\text{Hz}}$). The circuit schematic of the current-to-voltage converter is shown in Fig. 2.12. All four feedback resistances have a value of 10 M Ω with a tolerance of 0.1%. The PSD output terminals (Q1, Q2, Q3, Q4) are connected with the circuit board by using short metal contacts instead of wires, in order to make the assembly as rigid as possible. This helps to control noise and drift caused by *triboelectric effects* (friction generated charges). The PSD is placed as close as possible to the op-amp input terminals (pins 2, 6, 9, 13, see Fig. 2.12 and Fig. 2.13), in order to minimize the influence of environmental noise caused by static electromagnetic fields.

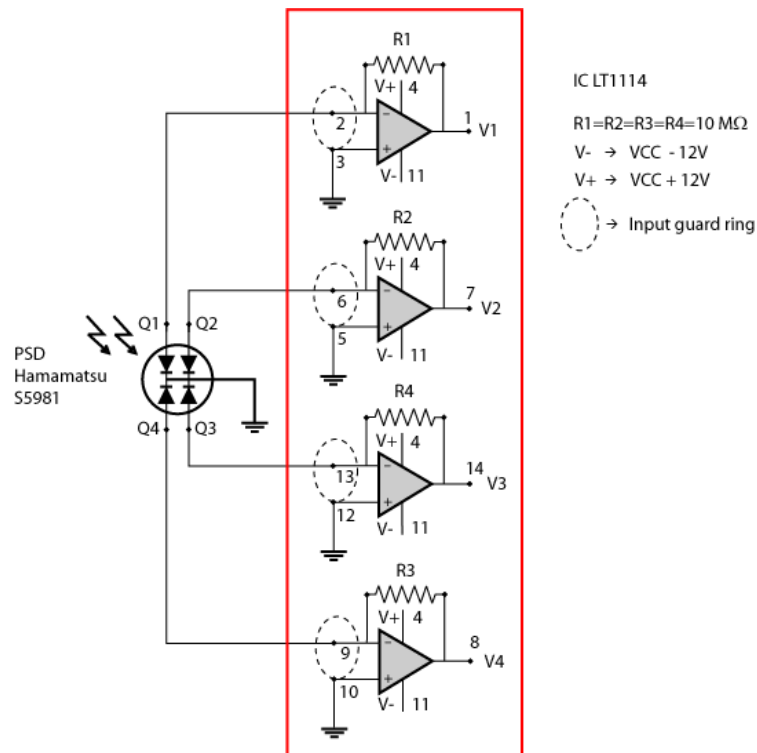


FIGURE 2.12 Schematic of the photodiode transimpedance amplifier based on LT1114 quad op-amp.

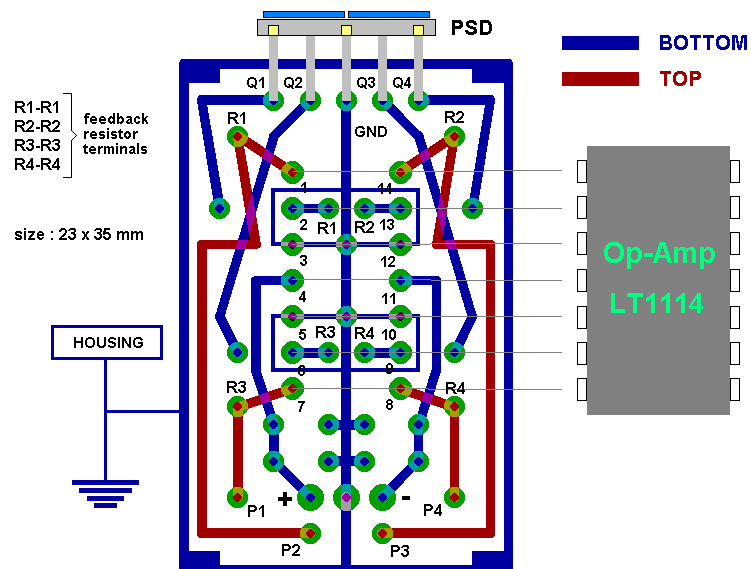


FIGURE 2.13 Transimpedance circuit board layout.

The whole assembly PSD/transimpedance amplifier is shielded by an electrically earth-grounded metal housing. The housing is mounted on a precision mechanical xy -stage, which allows for positioning of the PSD with micrometer precision (Fig. 2.14). More details concerning the circuit shielding from electrostatic fields and additional relevant stability and noise issues will be discussed in Paragraph 2.1.7.

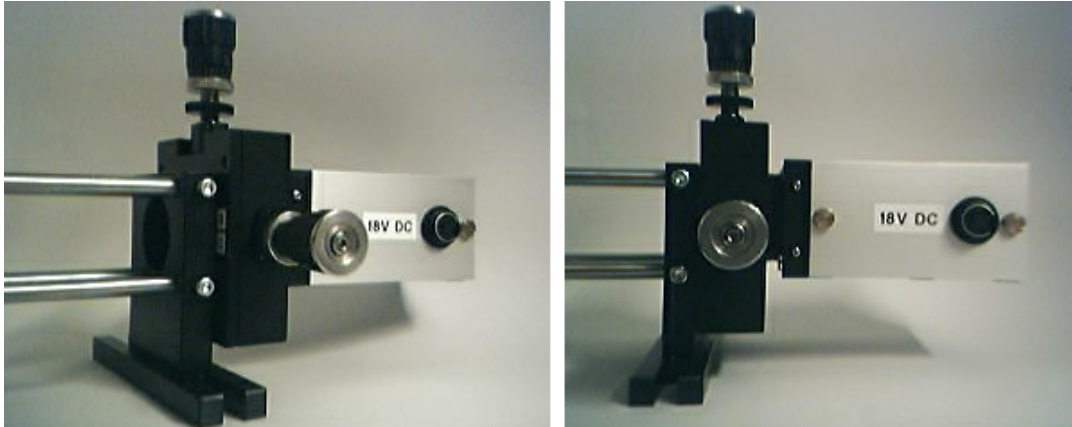


FIGURE 2.14 Transimpedance preamplifier circuit housing.

Step (b): nulling circuit

The amplified voltage signals at $V1$, $V2$, $V3$, $V4$ (see Fig. 2.12) are brought to a second circuit using a shielded cable. The aim of this second circuit is to convert the four voltage signals into three voltage signals proportional to the displacements of the light spot along the x - and y -direction (with respect to the PSD's center). This circuit is a typical *nulling circuit*. The circuit generates also the total intensity signal ($V_{SUM} = V1 + V2 + V3 + V4$) used for signal normalization. As discussed in Paragraph 2.2.2, V_{SUM} is also proportional to bead displacements along the z -axis (optical axis). The schematic of this second circuit is shown in Fig. 2.15.

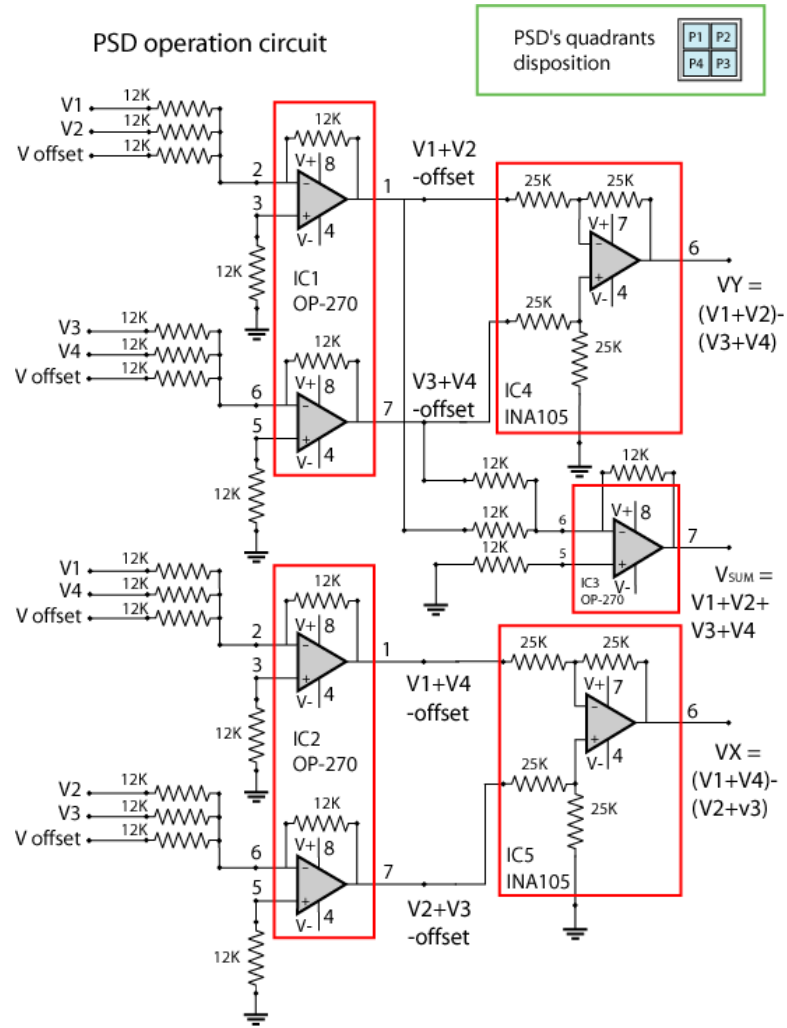


FIGURE 2.15 PSD processing circuit.

Basically, the circuit consists of a summing and a differential stage, and generates the following signals:

$$VX = (V1 + V3) - (V2 + V4) \quad (2.3)$$

$$VY = (V1 + V2) - (V3 + V4) \quad (2.4)$$

$$V_{SUM} = V1 + V2 + V3 + V4 \quad (2.5)$$

Additionally, a variable offset voltage (V_{offset}) can be subtracted from V_{SUM} . That avoids saturation of the op-amps in the circuit in case of too large amplification by the current-to-voltage converter. After digitization, the outputs are normalized as follows:

$$VX_{norm} = VX / V_{SUM} ; \quad VY_{norm} = VY / V_{SUM} \quad (2.6)$$

2.1.6 Data acquisition

step (c): signal digitization and recording -DAQ hardware

control and measurement software

Finally, the analog signals are digitized employing an analog-to-digital acquisition board (DAQ) (National Instruments, PCI-6024E) which is interfaced to a personal computer. Digitized data are then saved on hard disk. The board has a maximum sampling rate of 200 ksamples/sec and 12 bit resolution, digitizing the ± 500 mV input range with 0.24 mV resolution. Signal acquisition is controlled via a software interface written in Visual Basic that was developed during this work. The software uses the developer's DLL library of National Instruments. A screen capture of the software interface is shown in Fig. 2.15. The desired sampling rate and number of measurement points can be selected via that interface. The software allows also for controlling of the motorized xy -stage through the PC serial port (RS232) used particularly for PSD response calibration (see Paragraph 2.2.2, p. 33). The stage can be moved stepwise along the x - or y -axes, or a complete surface can be scanned. Manual control of the stage can be done with the Joystick-on/off buttons.

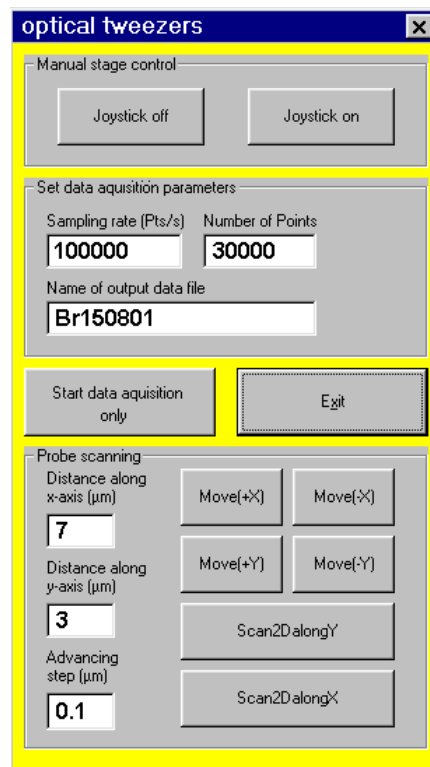


FIGURE 2.15 Screen capture of the interface of optical tweezers' control software.

2.1.7 PSD circuit: performance and electronic noise control

factors determining the circuit performance

The *circuit performance* of a transimpedance amplifier in terms of gain, bandwidth, stability and signal-to-noise ratio (SNR) depends on a complicated and nonlinear interplay of several factors (Graeme 1996, Burr-Brown 1994), the most relevant of which are:

- desired bandwidth (BW)
- desired gain factor (G)
- feedback resistor (R_F)
- feedback capacitance (C_F)
- gain-bandwidth product of the op-amp (GBP)
- op-amp voltage noise ($V_{noise}(amp)$)
- op-amp current noise ($I_{noise}(amp)$)
- op-amp input capacitance (C_{Amp})
- photodiode junction capacitance (C_{PD})
- photodiode shunt resistance (R_{Sh})

In the case of a photodiode transimpedance amplifier, the three circuit design variables are:

- the feedback loop
- the op-amp
- the photodiode

The circuit response, gain and stability are strongly affected by the non-ideal characteristics of these three elements. Their interplay in the actual circuit can be properly analyzed by using the model shown in Fig. 2.16.

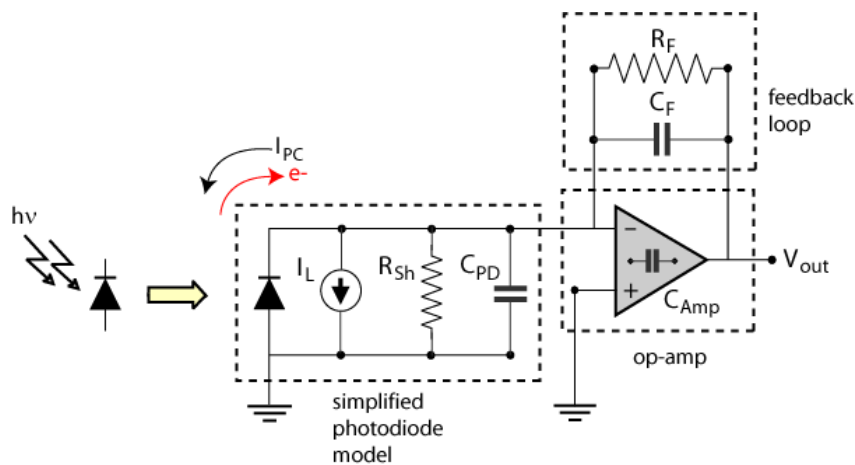


FIGURE 2.16 Simplified model for stability and noise analysis of the transimpedance amplifier with the PSD operating in photovoltaic mode.

*transimpedance
gain*

a) Feedback loop. In the feedback loop of the current-to-voltage converter, noise and bandwidth as well as gain are largely determined by the values of resistance (R_F) and capacity (C_F). An approximated estimation of the gain of the current-to-voltage converter is given by the *transfer function*:

$$G = \frac{V_{out}}{I_{PC}} = \frac{V_{out}}{\Re P_0} = R_F \quad (2.7)$$

where:

V_{OUT} is the voltage at the output of the operational amplifier in V;

I_{PC} is the photocurrent produced by the photodiode in A;

\Re is the responsivity of the photodiode in A/W;

P_0 is the incident light power in W.

For a resistance value of $R_F = 10 \text{ M}\Omega = 10^7 \Omega$ the gain is

$$G = 20 \log_{10}(10^7) = 140 \text{ dB} \quad (2.8)$$

voltage noise

The value of the noise originating from the feedback resistor, $V_{NOISE}(R)$ (unit V_{rms}), can be quickly calculated by using the relation

$$V_{NOISE}(R) = \sqrt{4K_B T R_F BW} \quad (2.9)$$

where:

$K_B = 1.38 \cdot 10^{-23} \text{ JK}^{-1}$ is Boltzmann's constant,

T is the temperature in Kelvin,

BW the system bandwidth in Hz.

Since the experimentally measured bandwidth of the amplifier is 110 kHz (see Paragraph 2.2.2), the noise caused by the feedback resistor is 0.134 mV_{rms}. Increasing the size of the resistor does not only increase the output noise in a square-root manner (Eq. (2.9)), but also increases the output signal in a linear manner (Eq. (2.7)). Thus, signal-to-noise ratio tends to increase with the square root of the resistance,

$$SNR \propto \sqrt{R_F} \quad (2.10)$$

Since the gain-bandwidth product (GBP) is a constant (for the op-amp LT1114 $GBP = 4.5$ MHz typ.), increasing the feedback resistance improves the gain and the SNR of the circuit, but limits the bandwidth.

b) op-amp. As already mentioned in Paragraph 2.1.5, the quadruple op-amp LT1114 is used in the current-to-voltage converter stage. Some relevant parameters of this integrated circuit are shown in Table 2.3.

Amplifier characteristics	Value
input noise voltage (V_n)	$1.8 \cdot 10^{-8} \text{ V}/\sqrt{\text{Hz}}$
input current noise (I_n)	$8.0 \cdot 10^{-15} \text{ A}/\sqrt{\text{Hz}}$
input bias current (I_b)	$1.5 \cdot 10^{-10} \text{ A}$
gain bandwidth product (GBP)	$4.5 \cdot 10^6 \text{ Hz}$
input offset voltage (V_{off})	$6.0 \cdot 10^{-5} \text{ V}$
input capacitance (C_a)	$4.0 \cdot 10^{-12} \text{ F}$

TABLE II.3 Specifications of the op-amp LT1114.

op-amp current noise The current noise generated by the op-amp flows through the feedback resistor and experiences the same gain as the signal current, leading to the additional noise component

$$V_{NOISE}(amp) = R_F I_{NOISE}(amp) \sqrt{BW} \quad [V_{rms}] \quad (2.11)$$

where R_F is the feedback resistance, I_{NOISE} is the total op-amp current noise, and BW is the system's bandwidth. For usual values of feedback resistance, current noises are negligible if op-amps with noise levels in the pA range are chosen.

op-amp voltage noise The contribution of op-amp voltage noise to the total noise is relevant only at low resistance levels (up to about 10 K Ω). Between 10 K Ω and 10 M Ω , resistor noise (expressed by Eq. (2.9)) is the dominant factor. At higher values of R_F , the op-amp noise becomes relevant again [Graeme 1996, Burr-Brown 1994].

bandwidth The bandwidth of the transimpedance amplifier can be obtained through the relation

$$BW = \frac{0.35}{t_r(amp)} \quad (2.13)$$

where $t_r(amp)$ is the rise time of the amplifier, defined as the time during which the signal rises from 10% to 90% of its final value. $t_r(amp)$ is expressed by:

$$t_r(amp) = \sqrt{(2.2R_F C_F)^2 + t_{PDr}^2} \quad (2.14)$$

with t_{PDr} being the rise time of the photodetector, approximated by

$$t_{PDr} = \frac{0.35}{f_{3dB}} \quad (2.15)$$

where f_{3dB} is the bandwidth of the photodetector.

Since $f_{3dB} = 20$ MHz, one obtains $t_{PDr} = 1.75 \cdot 10^{-8}$ sec. Taking $R_F = 10$ M Ω and $C_F = 1$ pF, it follows that the amplifier bandwidth is determined mainly by the time constant of the feedback loop $\tau = R_F C_F \cong 10^{-5}$ sec.

photodiode current noise

c) Photodiode. As seen in Paragraph 2.1.4, the PSD is operated in photo-voltaic mode, which means that no external voltage is applied to the photodiode (zero biasing). This implies that the dominating factor of the photodiode's current noise (called *dark current* or *leakage current*) is a diffusion current, and varies with the square root of the temperature. Such noise is also called *thermal* or *Johnson noise*, and its value is given by

$$I_{jn} = \sqrt{\frac{4K_B T (BW)}{R_{sh}}} \quad (2.16)$$

where R_{sh} is the parasitic resistance (or *shunt resistance*) of the photodiode. Its value typically exceeds 100 M Ω . The r.m.s. noise value is then given by

$$V_{NOISE}(PD) = I_{jn} R_F \sqrt{BW} = \Re \cdot NEP \cdot R_F \sqrt{BW} \quad [V_{rms}] \quad (2.17)$$

with

R_F the feedback resistance,

\Re the responsivity of the photodiode,

NEP the noise equivalent power.

NEP is defined as the amount of light power which generates a photocurrent equal to the noise current. For a photodiode with large active area, the *NEP* value is about 10^{-11} W $\sqrt{\text{Hz}}$. For the system used in this work, the calculated $V_{\text{NOISE}}(PD)$ is about 50 mV_{rms}.

Circuit capacitances have profound performance effects in terms of stability, bandwidth and noise. It is known that the input capacitance of an op-amp (C_{amp}) can cause instability when the op-amp is used with a feedback resistor. Particularly, the circuit will oscillate and display gain peaking. Stability is usually achieved by adding a capacitor C_F across the feedback resistor R_F (see Fig. 2.16).

The *photodiode junction capacitance* (C_{PD}) must also be taken into account when considering stability. C_{PD} is a by-product of the width of the depletion region between the *p*-type and *n*-type material of the photodiode. A wider depletion region, as found in PIN photodiodes, increases the magnitude of the junction capacitance. In the PSD S5981, the total capacitance from the four quadrants is 60 pF.

Considering C_{PD} and C_{amp} , the optimized value for C_F can be found through the equation [Graeme 1996]:

$$C_F = \sqrt{\frac{C_{PD} + C_{\text{amp}}}{2\pi R_F \text{GBP}}} \quad (2.18)$$

Applying Eq. (2.17), an optimal value of $C_F \cong 0.5$ pF is found for preventing oscillations in the current-to-voltage converter. In practice, the parasitic capacitance (about 0.1 pF) originating from on-board capacitive coupling and from parasitic capacitances is enough to avoid circuit oscillations. Therefore, it was decided not to add a feedback capacitance to the circuit, thus avoiding further bandwidth limitation without compromising stability.

Electromagnetic coupling. With its very high impedance, a current-to-voltage converter is extremely sensitive to noise coupling from low and radio frequency electromagnetic sources. These sources require excellent shielding, grounding, and “smart” relative arrangement of all components for preventing them to become dominant noise contributors. A very common noise source is *electromagnetic coupling* at power line frequency (60

Hz). This noise is coupled via the mutual capacitances that exist between any two objects. In order to avoid such coupling, the PSD is placed as close as possible to the op-amp's input terminals using short leads (Fig. 2.13). A further improvement is achieved by a metallic housing which is earth-grounded (Fig. 2.14).

2.2 System performance

2.2.1 Laser

When performing sensitive force measurements with optical tweezers, the performance of the trapping laser is of key importance. The laser employed in this work is a solid state diode-pumped Nd:YAG laser, generating a continuous-wave TEM₀₀ beam at a wavelength of 1064 nm. Laser diode pumping assures high output stability much superior than that of older flash-bulb-pumped lasers. The stability of the laser's output power is better than 2%/hour, and its noise between 10 Hz and 1 GHz is lower than 2% r.m.s. The laser is adequately cooled by heat conduction through the metal base, avoiding mechanical vibrations caused by ventilators.

2.2.2 Position and force detector

The aim of the position detection system is to monitor the displacements of a trapped particle with highest possible spatial and temporal resolution. As discussed in Chapter III, the analysis of the power spectrum of thermal oscillations of the particle allows both for the characterization of the optical trap (i.e. measurement of the trap's harmonic constant) and for getting information about the mechanical properties of the surrounding environment. As already mentioned in Paragraph 2.1.2-2.1.4, particle movements are observed by imaging the laser light that is scattered back from the particle onto the surface of the segmented photodiode. In order to obtain reliable data, the performance of the PSD electronic system in terms of bandwidth and noise had to be evaluated. Moreover, the PSD response curve (voltage signal vs. displacement, V/nm) had to be found.

*bandwidth of the
PSD system*

Bandwidth of the PSD system. The bandwidth of the PSD system can be experimentally measured by using the set-up schematically shown in Fig. 2.17. In that set-up, a square wave signal from a signal generator drives a red

LED placed in front of the PSD.

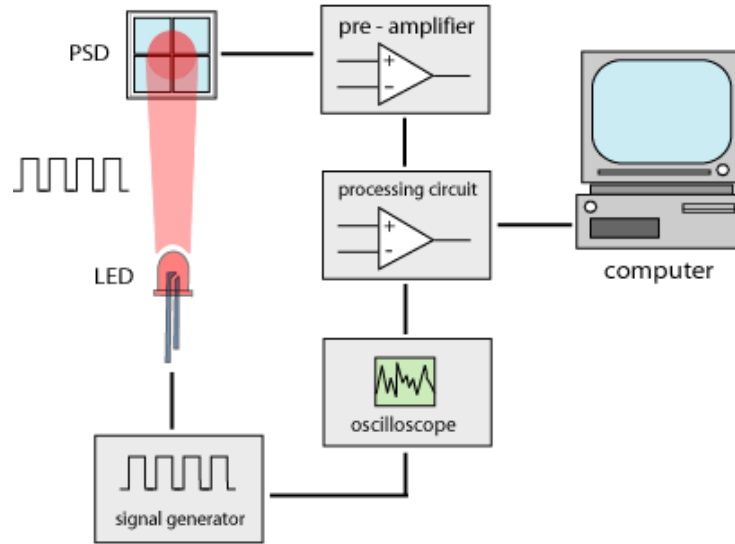


FIGURE 2.17 Determination of the bandwidth of the position measurement system.

The light from the LED illuminates the photodiode. The corresponding response of the PSD electronic system is monitored by an oscilloscope and simultaneously recorded on a PC for further analysis. The driving signal from the signal generator is also observed with the oscilloscope.

The current-to-voltage gain, expressed in *decibel*, is given by:

$$G(\text{dB}) = 20 \cdot \log_{10} \left(\frac{V}{V_{\max}} \cdot 10^6 \right) \quad (2.19)$$

where V_{\max} is the maximum response signal, and the value 10^6 is the maximal gain determined by the transimpedance value, $R_F = 1 \text{ M}\Omega$. The gain is then plotted against the blinking frequency of the LED (so called *Bode plot* – Fig. 2.18). The system's bandwidth is the frequency where the voltage gain drops down to about 70.7 % of its maximum value (that means a drop of -3 dB if the gain is expressed in decibel). As shown in Fig. 2.18, the measured bandwidth of the PSD system is about 100 kHz.

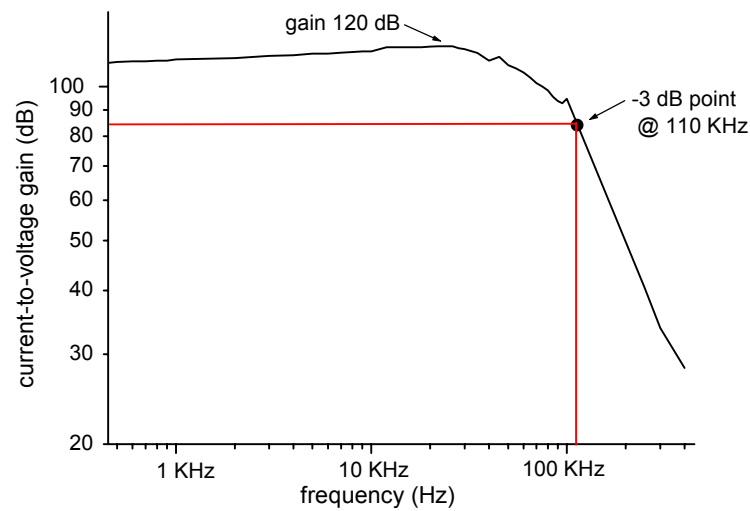


FIGURE 2.18 Bode plot displaying the bandwidth of the position measurement system.

dark noise

Noise of the PSD system. The instrumental and mechanical noise of the PSD system can be properly characterized in the frequency domain by comparing the *power spectral density* of the detector signal under various conditions. First of all, the voltage signal at no illumination (laser switched off) is measured (*dark noise*). Dark noise accounts for the electronic and *shot noise* affecting the detector. For this measurement the signal at the sum channel is recorded ($V_{SUM}=V1+V2+V3+V4$). The maximum dark noise amplitude occurs to be lower than the maximum digitization resolution of the analog-to-digital converter, corresponding to 0.24 mV for an input range of ± 0.5 V. The measured dark noise power spectrum is shown in Fig. 2.19. The origins of dark noise are clearly electronic, and probably due to the digital-to-analog-converter board itself. As evident from the spectrum, the dark noise frequency is 100 Hz. No 60 Hz-noise caused by power lines appears in the spectrum, which demonstrates the good circuit EM-shielding. Some higher harmonics of the 100 Hz signal are also visible.

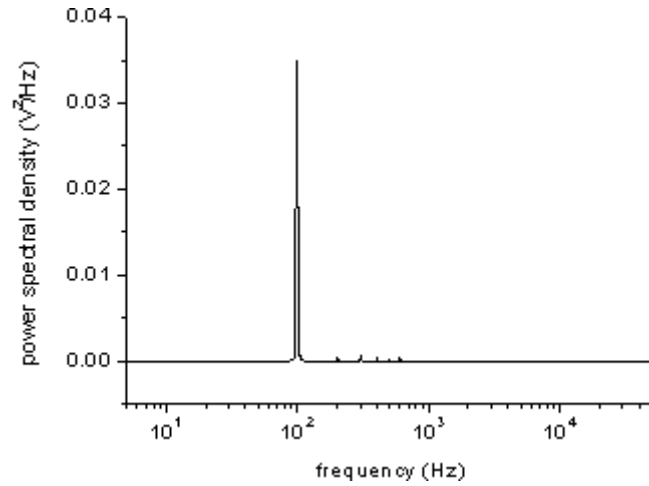


FIGURE 2.19 Dark noise power spectrum of the position sensing system.

Bright noise The *bright noise* is measured under experimental conditions similar to those used for trapping (laser switched on and focused inside the probe chamber, same laser power as used for trapping experiments), but with no trapped particle. PSD bright noise arises predominantly from variations of the laser light that is scattered back by the bottom glass interface of the probe chamber and can be attributed to low-frequency mechanical vibrations. Fig. 2.20 displays the power spectrum as measured on the differential channel $VX = V1 + V3 - V2 - V4$. The VX channel basically detects mechanical noise produced by lateral vibrations of the set-up. A strong peak at 25 Hz can be observed, flanked by smaller noise peaks at lower frequencies.

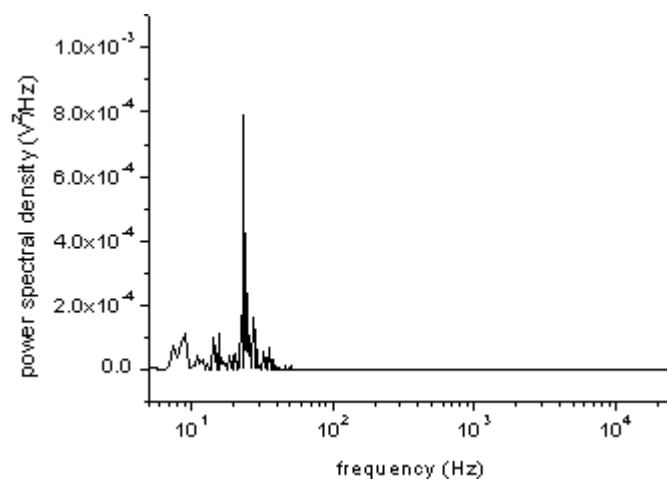


FIGURE 2.20 Bright noise power spectrum - differential signal $VX=(V1+V3)-(V2+V4)$. Laser power output 50 mW.

In contrast, the total intensity signal output $V_{SUM} = V1 + V3 + V2 + V4$ is sensitive to axial vibration modes of the set-up. In Fig. 2.21, the power spectra of VX and V_{SUM} are compared. It can be seen that the 25 Hz noise peak has a very high power density in the V_{SUM} -spectrum. A weaker peak at a noise frequency at 75 Hz does also appear. Comparing the two spectra, it can be concluded that the 25 Hz-noise results mainly from axial vibrations, and that the same frequency in the VX spectrum probably originates from cross-talk between the two channels (see also Fig. 2.26). Cross-talk is probably caused by an uneven illumination of the PSD's surface. Indeed, the bottom of the probe chamber is not perfectly flat on a micrometer scale. Therefore, small axial displacement produce tiny (but well detectable) lateral variations in the backscattered light, resulting in a non-zero signal on VX .

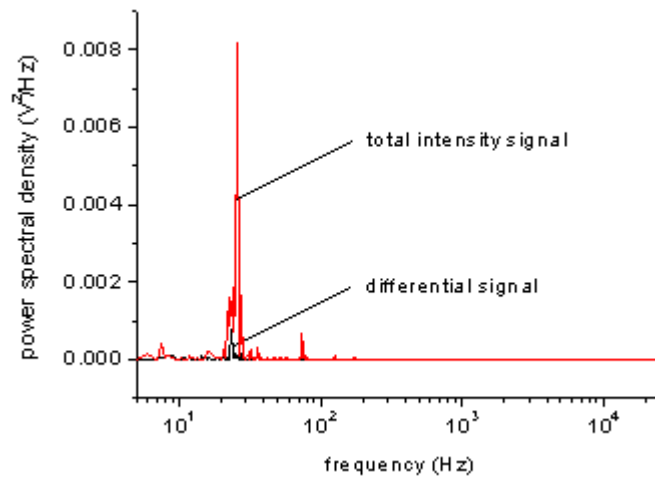


FIGURE 2.21 Bright noise power spectrum. Comparison between sum and differential signal.

Fixed bead noise The *fixed bead noise* assesses the mechanical noise detected by the position sensing system when the laser is focused on an immobilized bead. The bead can be fixed by adsorbing it to the surface of the microscope chamber (for example by drying a bead suspension within the chamber, adding afterwards water again), or alternatively by embedding it into a transparent matrix. In order to keep the experimental conditions as close as possible to those of a typical trapping experiment, the second approach was chosen, by embedding polystyrene beads (diameter of 0.908 μm) into an agarose gel matrix. To prepare the matrix, a 1% w/w suspension of agarose gel in water is heated to a temperature of about 50 $^{\circ}\text{C}$ until the agarose is completely dissolved, yielding a clear solution. Then, 50 μl of a bead/water suspension (2% w/w) is added, and the agarose solution is allowed to cool and solidify directly in the microscope chamber. The advantage of embedding the beads

in agarose gel is that the refractive index of the matrix is nearly the same as that of pure water, so that the position-detection conditions are closely reproduced. The fixed-bead noise signals as measured on V_{SUM} and VX are shown in Fig. 2.22. The fixed bead induces a dramatic increase of the back-scattered light, strongly enhancing mechanical-noise level as detected by the PSD. This can clearly be seen from the high amplitude of the oscillations in Fig. 2.22.

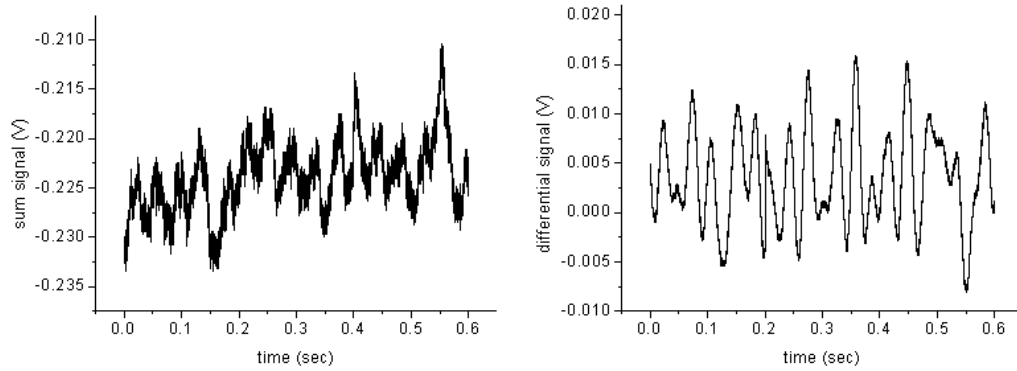


FIGURE 2.22 Fixed-bead noise detected by the PSD system. The total intensity signal ($V_{SUM} = V1+V2+V3+V4$) (left side) and the differential signal ($VX=(V1+V3)-(V2+V4)$) (right side) are displayed. Laser power output was 50 mW.

The fixed bead makes the lateral displacements of the set-up (measured at the differential output VX) very evident. The noise power spectra corresponding to V_{SUM} and VX are shown in Fig. 2.23.

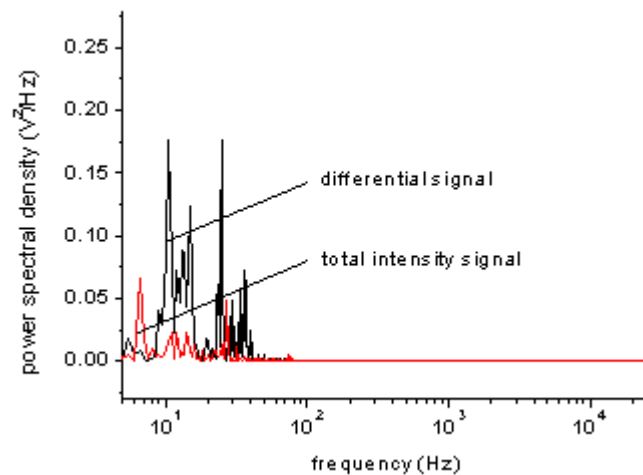


FIGURE 2.23 Fixed-bead noise power spectrum. Comparison between total intensity and differential signal.

Both spectra basically display the same frequencies noticed also in the bright-noise measurement. Low frequency oscillations at 10 and 15 Hz are evident, particularly in the VX spectrum.

Finally, the power spectrum produced by an optically trapped bead is displayed in Fig. 2.24. About 10 spectra from independent traces of the measured time series were averaged. In this case, the PSD system detects just the spontaneous thermal fluctuations (*Brownian motion*) of the particle immersed in the aqueous medium. The data were measured on beads with 0.91 μm diameter, using a laser power of 55 mW (as measured at the output of the laser head).

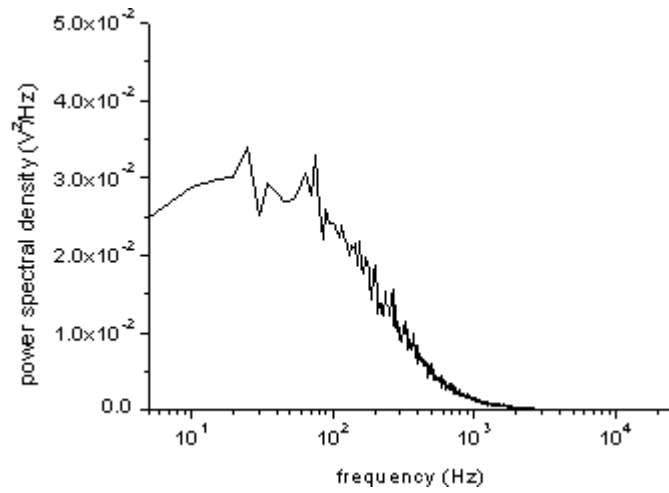


FIGURE 2.24 Power spectrum of a trapped bead (VX output) and its characteristic Lorentzian shape. Output laser power was 55 mW.

The power spectrum of the motion of a particle in an optical trap has a Lorentzian shape (Fig. 2.24) given by

$$\tilde{x}(\omega) = \frac{\sqrt{2D}}{i\omega + \kappa/\gamma} \quad (2.20)$$

where $\gamma = 6\pi\eta r$ is Stoke's hydrodynamic drag coefficient of a bead with radius r immersed in a medium of viscosity η ; the ratio $\kappa/\gamma = \omega_c$ corresponds to the so-called *corner frequency* of the trap (see Chapter III – Paragraph 3.2.2). At the corner frequency, the spectrum has decayed to one-half of its maximum value at $\omega = 0$. For a bead with 1 μm diameter, the drag coefficient γ is about $8 \cdot 10^{-9}$ kg/s. For the 1 μm bead, typical values of ω_c range between 100 and 300 Hz, depending on the trapping laser power.

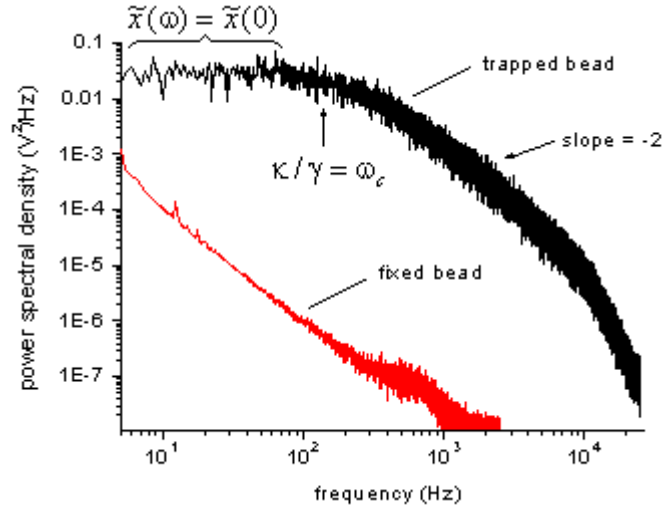


FIGURE 2.25 Comparison between trapped and fixed bead power spectra.

Thermal motion is the dominant noise source which limits the resolution in micro-mechanical measurements where forces and displacements are measured by a trapped probe. However, the analysis of the thermal fluctuations of a trapped bead (*thermal fluctuations spectroscopy*) can also give important information about the viscoelastic properties of the particle's (see Chapter III). In Fig. 2.25 the log-log plots of the power spectra of a fixed and trapped bead are compared. The trapped-bead spectrum is divided into two regions by the corner frequency ω_c : the low-frequency part of the spectrum ($\omega < \omega_c$) is approximately constant ($\tilde{x}(\omega) = \tilde{x}(0)$), and reflects the confinement of the particle inside the nearly harmonic potential well of the optical trap. The high-frequency part ($\omega > \omega_c$) is a line with slope value of -2 . This portion of the spectrum is characteristic for a free-diffusion process (ω_c falls off like $1/\omega^2$). This means that the particle „feels“ the trap potential only over time intervals longer than $1/\omega_c$. For shorter times, the particle's behavior is that of a free-diffusing object. Measuring ω_c allows the determination of the trap's force constant k (*trap stiffness* - see also Chapter III, Paragraph 3.2.2)

$$k = \gamma\omega_c \quad (2.21)$$

In the trapped-bead spectrum, a second decline with larger slope value can also be discerned at higher frequencies ($>10^4$ Hz).

PSD response calibration

For performing quantitative measurements of bead displacement, the PSD response with respect to bead position had to be calibrated. For doing this, the same immobilization protocol was used as already adopted for the fixed-bead noise measurements. As previously mentioned, beads with $0.908 \mu\text{m}$

diameter were fixed by embedding them in a hardened agarose gel matrix. By using the piezoelectric element connected with the objective, the focus of the trapping laser was moved vertically by 6 μm inside the microscope chamber. At this trap-surface distance, most of the subsequent experiments were performed (see Chapter III). By scanning the sample with the xy -stage, a bead was searched that was fixed at exactly 6 μm distance above the chamber's bottom surface. Next, the bead was precisely centered by searching the position giving zero VX and VY voltage signals.

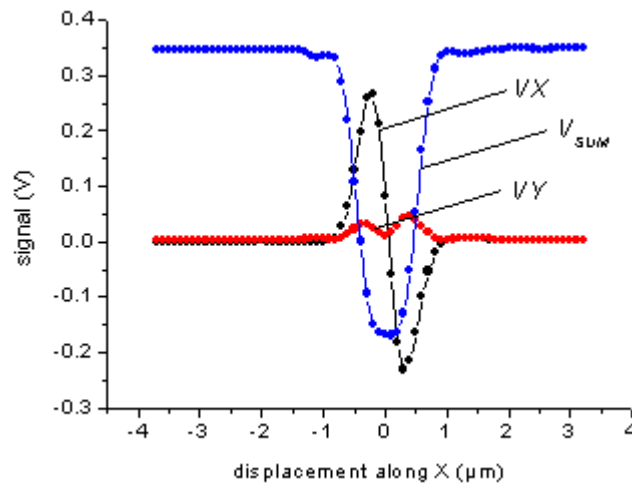


FIGURE 2.26 PSD calibration: VX , VY , V_{SUM} signals obtained by scanning a fixed bead along the x -axis.

By using the control program described in Paragraph 2.1.6, the bead was scanned along either the x - or the y -axis, and a calibration curve was measured. For most calibration curves, the scan step-size was set to 100 nm. Fig. 2.26 shows three curves representing the voltage signals (VX , VY , VZ) produced by the PSD during the scan of a 0.908 μm -bead along the x -direction. The VX calibration curve has an excellent signal-to-noise-ratio, whereas the VY -curve shows only small variation, except for some unavoidable cross-talk, whose amplitude is less than 10% of the VX -signal. For displacements between -300 and +300 nm from the trap's center, the PSD response is linear.

Since the maximum thermal fluctuations amplitude of a trapped bead does not exceed this linearity interval, only that range is evaluated for PSD calibration along both axes. When scanning along x - and y -direction, VZ displays a very strong variation, with a plateau of about 500 nm width, which corresponds to the linearity range along the x - and y -direction. The base-line voltage of VZ (in Fig. 2.26 at about 0.35 V) depends on the voltage-offset which is set by the processing circuit (Paragraph 2.1.5) in order to avoid op-amp saturation.

Fig. 2.27 shows the VX and VY signals arising from scanning along the Y -axis.

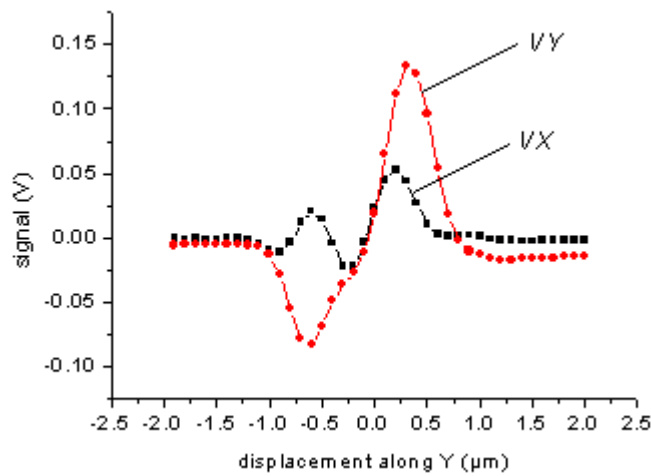


FIGURE 2.27 PSD calibration: VX , VY signals obtained by scanning a fixed bead along the y -axis.

*influence of
trapping laser
polarization on
PSD response
along Y*

Here, the interval of linearity is broader (about 800 nm) than that observed in the calibration curve along X , showing also a smaller gradient. Moreover, some non-linearity and cross-talk >40% between the VX and VY signals are observed. The poor performance of the position detection along the y -axis is basically due to the linear polarization of the trapping laser. For a linearly polarized input field, the intensity distribution in the focal plane is not rotationally symmetric, but has rather elliptic shape (Fig. 2.28) [Quabis 2001]. In our case, the minor axis of the ellipse coincides with the y -direction, resulting in a lower scattering intensity along that axis. A perfectly circular intensity distribution could be obtained by focusing laser beam with circular polarization.

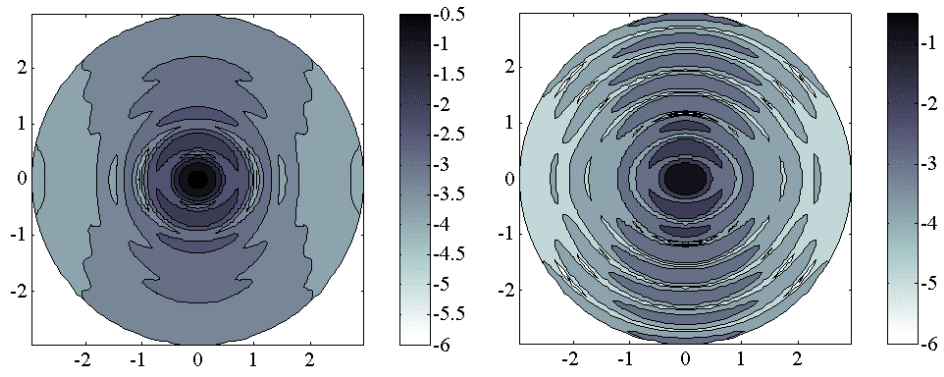


FIGURE 2.28 Calculated intensity distribution in the focal plane arising from a linearly polarized laser beam (left - the refractive index mismatch between oil and water was taken in account in the calculation; right - intensity distribution for an ideal focus).

PSD xy-two-dimensional response map

In order to obtain a two-dimensional picture of the PSD response, a surface of about $1 \mu\text{m}^2$ was scanned with a step size of $0.1 \mu\text{m}$. Fig. 2.29 shows a series of images of the light that is back-scattered by the bead during one single-line scanning along the X -axis. The frames were taken with a CCD-camera.

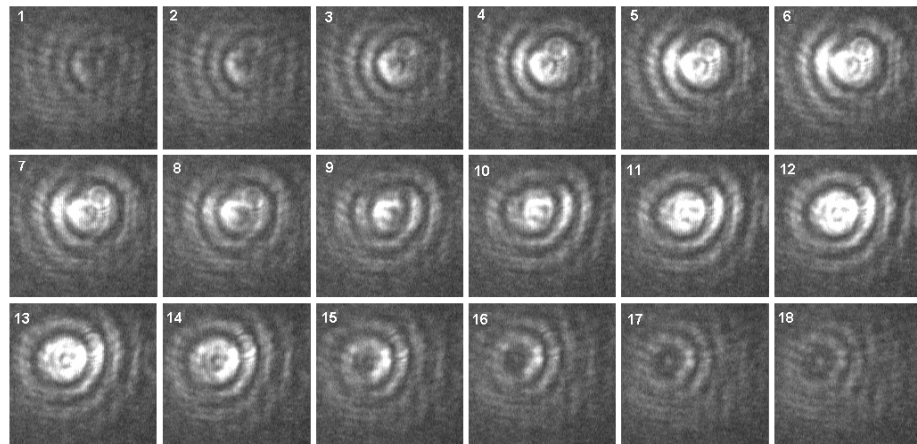


FIGURE 2.29 Light distribution of scattered light from a bead during x-scan.

The resulting two-dimensional map of the PSD response on the VX output is displayed in Fig. 2.29. Imaging was performed by scanning parallel lines along the y -direction. Line-to-line grid distortion and shifting caused by scanning-stage hysteresis were corrected with a software algorithm.

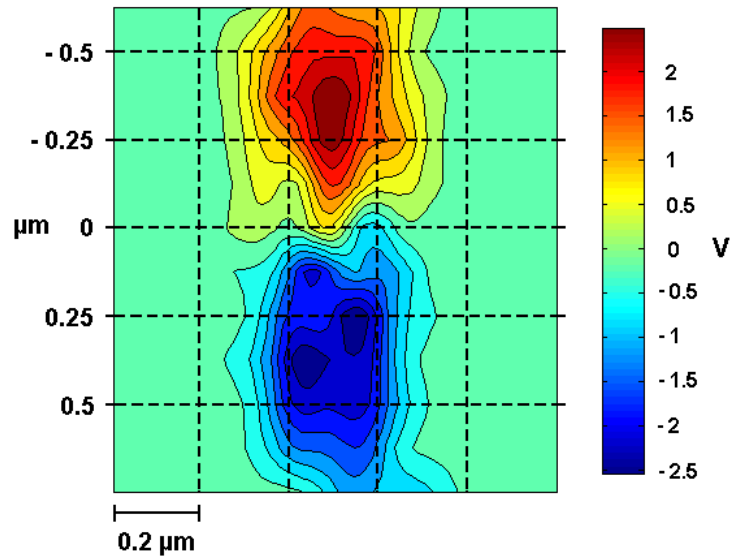


FIGURE 2.30 2D contour plot of the PSD voltage response (VX) when scanning a 0.9 μm bead.

In Fig. 2.31, a three-dimensional plot of the same PSD response is also shown.

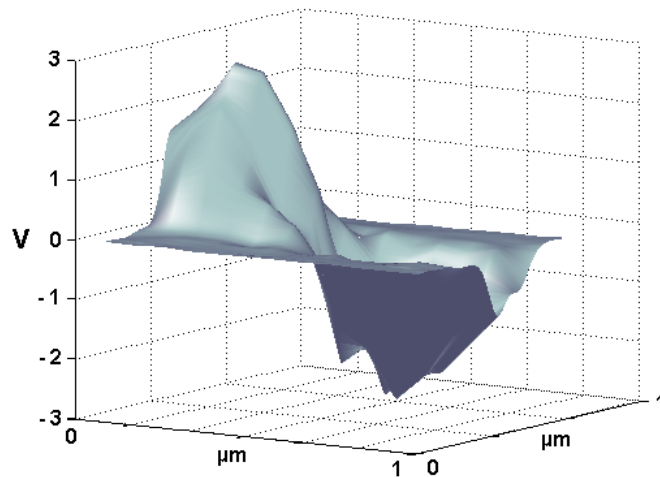


FIGURE 2.31 3D plot of the PSD voltage response (VX) by a 0.9 μm bead.

*calibration along
z-axis*

Finally, the PSD response along the z-axis was calibrated. Calibration was performed by stepwise displacing the laser focus along the optical axis with the piezoelectric focusing element (PIFOC, Physik Instrumente, Germany) over a fixed bead positioned at a distance of exactly 6 μm above chamber's bottom surface.

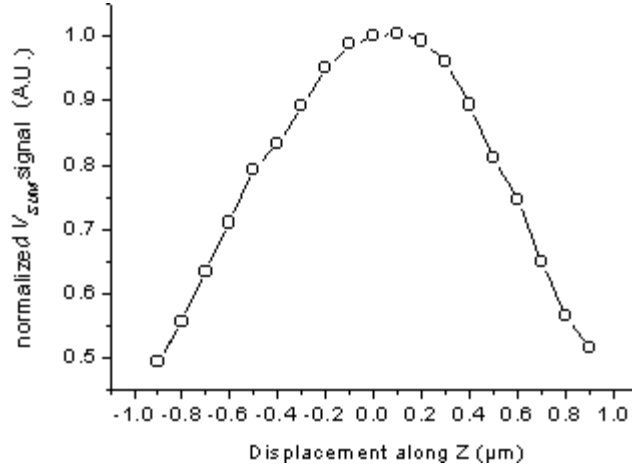


FIGURE 2.32 PSD calibration: V_{SUM} signal obtained by moving the laser focus across a fixed bead (normalized to max V_{SUM}).

Scan step size was again $0.1 \mu\text{m}$, and total scan range was $1.8 \mu\text{m}$. Fig. 2.32 shows the measured V_{SUM} curve. The curve is normalized to its maximum value, corresponding to $z = 0$ position of the focus (bead centered exactly in focus). The curve can be well fitted by a parabolic function

$$V_{SUM}(\text{normalized}) = a + b \cdot z^2. \quad (2.22)$$

Fig. 2.33 shows the histogram of the position fluctuations of a trapped bead (diameter $0.9 \mu\text{m}$) along the z -axis. Similarly to the z -calibration curve, the V_{SUM} signal is normalized to its maximum intensity. By comparing the histogram with the calibration curve, one can conclude that the bead is trapped about 450 nm above the focal plane.

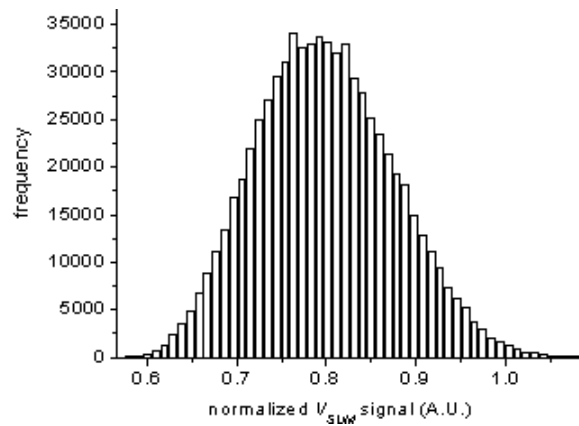


FIGURE 2.33 Histogram of the thermal position fluctuations of a trapped bead along Z -axis.

That means that a bead in an optical trap finds its stable axial equilibrium point in a position that is slightly shifted upwards with respect to the laser focus, due to the interplay between scattering and gradient forces. Therefore, in order to calibrate bead displacements along the z -axis, only half of the calibration curve is considered (Fig. 2.32) corresponding to positive displacement values.

Finally, Table 2.4 displays the calibrated r.m.s. amplitudes of the main noise sources.

Source	Noise (nm r.m.s.)
Bright noise (X)	0.26
Fixed bead noise (X)	5.50
Brownian motion (X)	23.3
Brownian motion (Y)	25.1
Brownian motion (Z)	129,8

TABLE 2.4 Comparison between r.m.s noise amplitude from different noise sources.

In Fig. 2.34, the calibrated x -signal of a trapped bead is compared with that obtained on a fixed bead noise.

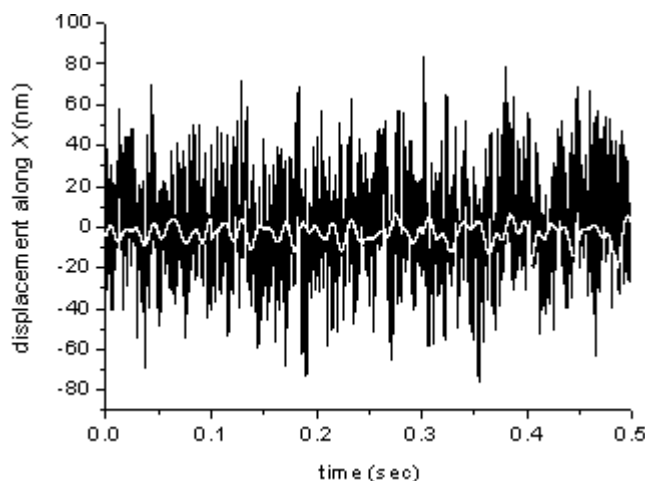


FIGURE 2.34 Comparison between trapped (black) and fixed bead (white) x -signal.

Unfortunately, the signal-to-noise ratio is not as high as previously reported in the literature, where a SNR of about 16 is given [Wuite 2000]. This will be a problem when measuring the Brownian motion of a particle suspended

in a high viscosity medium. This issue is further discussed in Chapter III. A better SNR can be achieved by improving the mechanical stability of the whole set-up.

References

- [Bakker Schut 1993] Bakker Schut T.C., Hesselink G., de Grooth B.G., Greve J.
Experimental and theoretical investigations on the validity of the geometrical optics model for calculating the stability of optical traps.
Cytometry 12: 479-485 (1991)
- [Berns 1992] Berns M.W., Aist J.R., Wright W.H., Liang H.
Optical trapping in animal and fungal cells using a tunable, near-infrared titanium-sapphire laser.
Exper. Cell Res. 198: 375-378 (1992)
- [Burr-Brown 1994] Burr-Brown Application Bulletin, AB-075
Burr Brown, Tucson, (1994)
- [Crocker 1996] Crocker J. C., Grier D. G.
Methods of digital video microscopy for colloidal Studies.
J. Colloid Interface Sci. 179: 298-310 (1996)
- [Graeme 1996] Graeme J.
Photodiode Amplifiers Op Amp Solutions.
McGraw-Hill, New York, ISBN 0-07-024237-X (1996)
- [Henderson 2001] Henderson S., Mitchell S., Bartlett P.
Position correlation microscopy: probing single particle dynamics in colloidal suspensions.
Colloids and Surfaces A 190: 81-88 (2001)
- [Quabis 2001] Quabis S., Dorn R., Eberler M., Glöckl O., Leuchs G.
The focus of light - theoretical calculation and experimental tomographic reconstruction.
Appl. Phys. B 72: 109-113 (2001)
- [Rohrbach 2001] Rohrbach A., Stelzer E. H. K.
Optical trapping of dielectric particles in arbitrary fields.
J. Opt. Soc. Am. A 18: 839-853 (2001)
- [Svoboda 1994] Svoboda K., Block S.M.
Optical trapping of metallic Rayleigh particles.
Opt. Lett. 19: 930-932 (1994)
- [Wuite 2000] Wuite G.J.L.
Single molecule studies of RNA and DNA polymerases using laser tweezers.
Dissertation - University of Twente, The Netherlands (2000)
ISBN 90-365 13944

Optical tweezers as a force transducer: microrheology and surface scanning

3.1 What is microrheology

Following the definition provided by the Society of Rheology, *rheology* is the science which studies deformation and flow of matter. Typical parameters measured in rheology are elasticity (elastic materials store energy like a spring when strain or shear is applied), viscosity (viscous materials dissipates mechanical energy under shear), and viscoelasticity. A material is termed *viscoelastic* if it has both elastic and viscous properties. Viscoelastic materials both store and dissipate energy as the material is stressed or sheared. The two optical techniques that are used for measuring rheological parameters in liquids are *dynamic light-scattering* (DLS) and *diffusing-wave spectroscopy* (DWS). Both DLS and DWS are “macroscopic” techniques that yield ensemble-averaged parameters. Each measurement requires at least several milliliters of substance. In contrast, *microrheology* [Mason 1995, MacKintosh 1999, Mukhopadhyay 2001] studies the rheological properties of fluids on a microscopic length scale. The underlying idea of microrheology is to optically monitor the thermal motion of colloidal beads with high spatial resolution. The principal advantages of microrheology compared with “macroscopic” optical techniques are the small strain values involved ($\sim K_B T$), the possibility to measure in extremely small volumes (< 1 ml), and the extended frequency range. Microrheology is essential for the study of the mechanical properties of biologic materials, such as actin-filament networks [Xu 1998], which are available only in small quantities and can be damaged by large strains. The minimum invasivity of the technique allows also the study of the cytoskeleton in living cells [Yamada 2000]. One of the most powerful techniques that are used in microrheological measurements is the so called

single particle tracking (SPT). In SPT, the trajectory of a Brownian particle is monitored by video microscopy [Crocker 1996, Crocker 2000, Valentine 2001 or by detecting, with a segmented photodiode, the light that is scattered by the particle [Mason 1997, Allersma 1998, Yamada 2000]. The latter approach is also called *laser deflection particle tracking* (LDPT). The key parameter obtained by SPT/LDPT experiments is the time-dependent mean square displacement of the particle. From this parameter, quantitative information about the loss and storage moduli can be obtained [Mason 1995, Mason 1997].

3.2 *Microrheology with optical tweezers*

3.2.1 Introduction

A special variation of SPT/LDPT employs optical tweezers. As was shown in Chapter I-II, optical tweezers can be used as a sensitive force transducer for measuring forces on a piconewton force scale. When using optical tweezers in association with a position-monitoring device such as a quadrant photodiode, forces up to several hundred pN can be applied and measured with high temporal (kHz range) and spatial (nm range) resolution. This makes optical tweezers a powerful tool for applying and measuring local forces in colloidal systems [Grier 1997]. Several applications of the combination of optical tweezers and SPT were reported in the literature. Valentine et al. [Valentine 1996, Hough 1999] measured the local viscosity of a polymer solution using rapidly oscillating optical tweezers. A particularly elegant method uses double-beam optical tweezers for positioning two colloidal particles very closely one to another. By *blinking* the optical tweezers, and monitoring the trajectories of the particles with videomicroscopy, the relative diffusion coefficient between the two particles can be measured [Crocker 1997]. With similar approaches, the interaction forces between two particles in electrolytic solutions [Sugimoto 1997], and the hydrodynamic coupling of two particles in water [Meiners 1999, Bartlett 2001] were measured. Verma et al. and Lin et al. [Verma 1998, Verma 2000, Lin 2001] measured the depletion (entropic) interactions between two particles in a solution of DNA and in suspensions of rods, respectively. The

influence of proximal surfaces on the diffusion of particles was studied with optical tweezers [Lin 2000, Clapp 2001]. The combination of optical tweezers and single-particle tracking was also applied to the investigation of biological systems. Peters et al. [Peters 1999] observed *in vivo* the trajectory of a transmembrane adhesion protein by bonding protein molecules to a colloidal bead and bringing it onto the cell membrane by optical manipulation. The trajectory of the membrane-anchored particle was subsequently monitored by measuring the deflection of the trapping beam with a segmented photodiode. The method allowed the measurement of the forces necessary to move the proteins through the membrane. Similar experiments were performed by Sako et al. [Sako 1998].

A particularly straightforward approach for measuring the local mechanical response of a fluid is monitoring the thermal motion (or Brownian motion) of an optically trapped particle [Florin 1998, Pralle 1998]. This approach was successfully applied for measuring the viscosity within a membrane lipid raft of a living cell [Pralle 2000]. In that work, a membrane protein was attached to a microsphere, captured by an optical trap and brought in contact with the cell membrane. By monitoring the motion of a microsphere confined within the trap, it was possible to measure the local viscosity within the raft and to deduce the protein's diffusion coefficient.

3.2.2 Brownian motion in a harmonic potential

Following the theoretical model proposed by Tlusty et al. [Tlusty 1998], for a small particle with radius smaller than 0.5 μm , the trapping gradient force is given by:

$$\vec{F}_{grad} = k \cdot r \exp\left(-\frac{r}{2\omega}\right) \quad (3.1)$$

where k is a constant depending on the polarizability of the particle, the particle's radius, and the laser beam waist ω ; and r is the distance of the particle's centre from the geometrical focus. In the vicinity of the focus ($r \approx 0$), the trapping potential is harmonic:

$$U_{grad} = \frac{1}{2}kr^2; \quad \vec{F}_{grad} = k \cdot \vec{r} \quad (3.2)$$

Consider now a Brownian particle moving within a one-dimensional harmonic potential. Its motion is described by a Langevin equation:

$$\frac{dx}{dt} = -\frac{k}{\gamma}x + \sqrt{2D}v \quad (3.3)$$

where x is the position coordinate of the particle, k is the force constant (or spring constant) of the potential, v is a Gaussian stochastic variable with the average value $\langle v(t) \rangle = 0$ and the variance $\langle v(t)v(t') \rangle = \delta(t-t')$, the constant γ is the drag coefficient of the particle, and the square-root term is a factor accounting i.a. for the strength of the thermal fluctuations of the embedding medium. The diffusion constant D is connected with the drag coefficient γ via the Einstein-Stokes equation, $D = k_B T / \gamma$, where k_B is the Boltzmann constant and T the absolute temperature of the medium. Associated with the above Langevin equation is a Fokker-Planck equation describing the temporal evolution of the probability density $P(x, t)$ for finding the particle at position x at time t :

$$\frac{\partial P}{\partial t} = \frac{\partial}{\partial x} \left(\frac{k}{\gamma} x P \right) + D \frac{\partial^2 P}{\partial x^2} \quad (3.4)$$

Thus, in the absence of the harmonic potential ($k = 0$), the particle's motion is that of a freely diffusing particle with diffusion constant D . Generally, if the particle is at a given position x_0 at initial time $t = 0$, the solution of the Fokker-Planck equation reads:

$$P(x, t | x_0) = \sqrt{\frac{\kappa}{2\pi D [1 - \exp(-2\kappa t)]}} \exp \left[-\frac{\kappa}{2D} \frac{[x - x_0 \exp(-\kappa t)]^2}{1 - \exp(-2\kappa t)} \right] \quad (3.5)$$

where the abbreviation $\kappa = k/\gamma$ was introduced. In the long-time limit, this solution approaches the stationary Boltzmann distribution:

$$P_{st}(x) = \sqrt{\frac{k}{2\pi k_B T}} \exp \left(-\frac{kx^2}{2k_B T} \right) \quad (3.6)$$

There are several ways of extracting values for the ratio $\kappa = k/\gamma$ from a measurement of the particle's motion. The two methods used most often are the corner frequency method and the autocorrelation method. In the corner frequency method, the power spectrum of the positional fluctuations of the particle is calculated. By applying a Fourier transform to Eq. (3.5), one directly finds the expression for the Fourier amplitude $\tilde{x}(\omega)$ at frequency ω :

$$\tilde{x}(\omega) = \frac{\sqrt{2D}}{i\omega + k/\gamma} \quad (3.7)$$

where it was taken into account that the Fourier amplitude of the Gaussian stochastic variable v is unity for all frequencies ω . Thus, the power spectrum $S(\omega)$ of the positional fluctuations is given by:

$$S(\omega) = \frac{2D}{\omega^2 + (k/\gamma)^2} \quad (3.8)$$

and the so called corner frequency ω_c , where this spectrum has decayed to one-half of its maximum value at $\omega = 0$, is equal to the ratio k/γ . Alternatively, the autocorrelation method calculates the autocorrelation function $g(t) = \langle x(t'+t)x(t') \rangle_{t'}$, where the brackets denote averaging over all possible time values t' . Using the results of Eq. (3.5, 3.6), this autocorrelation is theoretically given by:

$$g(t) = \int dx \int dx_0 x x_0 P(x, t | x_0) P_{st}(x_0) = \frac{k_B T}{k} \exp(-\kappa t) \quad (3.9)$$

showing that κ is the exponential decay factor of the positional autocorrelation. Recently [Henderson 2001], an alternative approach was proposed for finding κ , which will be called histogram method in the following sections. It involves histogramming the positional changes $\Delta x(\tau) = x(t+\tau) - x(t)$ at varying delay times τ . Using Eq. (3.5), these histograms are given by:

$$H(\Delta x, \tau) = \int dx_0 P(x_0 + \Delta x, \tau | x_0) P_{st}(x_0) \\ = \sqrt{\frac{\kappa}{4\pi D [1 - \exp(-\kappa\tau)]}} \exp\left[-\frac{\kappa}{4D} \frac{\Delta x^2}{[1 - \exp(-\kappa\tau)]}\right], \quad (3.10)$$

representing Gaussian distributions with variance σ defined by:

$$\sigma^2(\tau) = \frac{2D}{\kappa} [1 - \exp(-\kappa\tau)] \quad (3.11)$$

so that κ can be extracted from the temporal evolution of $\sigma^2(\tau)$. This is the most straightforward way of analyzing the data, not involving calculations such as a Fourier transformation or an autocorrelation.

3.2.3 Set-up

A detailed description of the experimental set-up is given in Chapter II. Fig. 3.1 shows a principle scheme of the set-up. Optical trapping is achieved using the infrared beam of a diode-pumped Nd:YAG laser (Laser Compact Ltd., wavelength 1064 nm, linearly polarized, max power 300 mW). The beam is expanded by a Galileian telescopic system and focused by an oil immersion microscope objective with high numerical aperture (Zeiss Neofluar, 100x and 1.3 N.A., oil immersion).

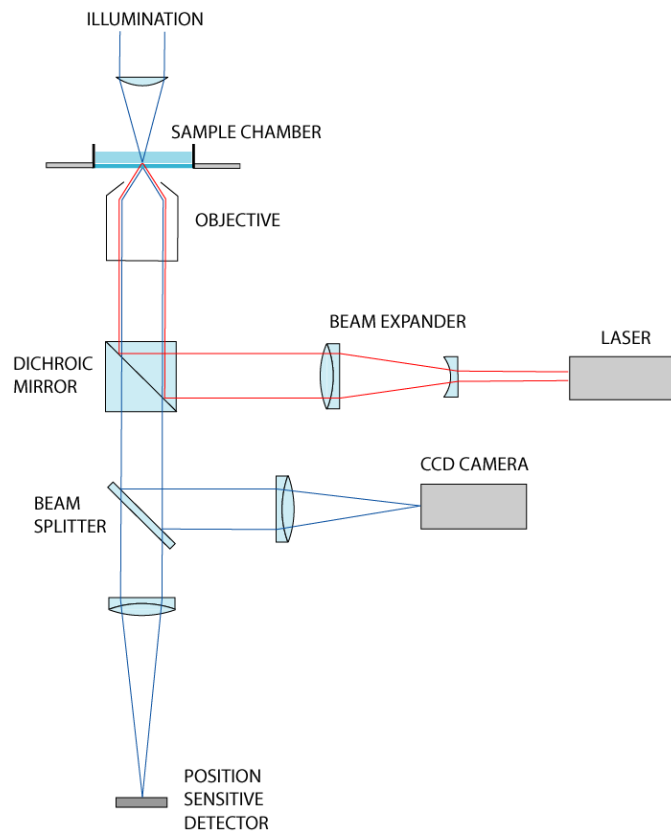


FIGURE 3.1 Set-up used for Brownian motion analysis.

The sample chamber is built by „sandwiching“ a disk-shaped cover-slip (diameter 50 mm, thickness 170 μm) between two aluminium rings. The upper ring constitutes also the chamber walls. Its external side is threaded, allowing the whole system to be firmly screwed to the xy -stage of the set-up (Fig. 3.2 and Fig. 3.3).

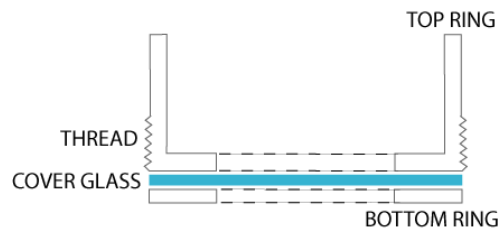


FIGURE 3.2 Scheme of the sample chamber.

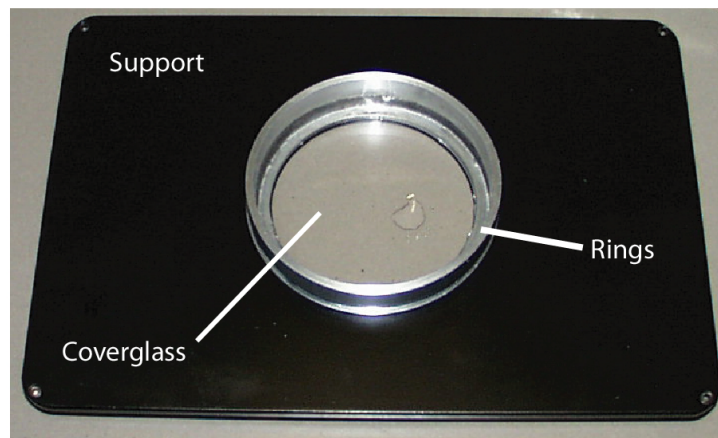


FIGURE 3.3 Mounted sample chamber.

The whole set-up was placed on a vibration-free optical bench, allowing a better control of environmental mechanical noise. A 2.5 % suspension of polystyrene beads with 0.91 μm diameter (Polysciences, Germany) were added at a 1:1000 ratio to mixtures of glycerine in water. For each measurement, a single bead was captured by the laser and brought to a distance of 6 μm above the cover-slip using a piezoelectric actuator (P721.00, Physik Instrumente, Germany). The three-dimensional position of the bead was continuously monitored by imaging the back-scattered light

onto a four-quadrant photodiode (S5981, Hamamatsu). The voltages generated by each quadrant were amplified, and processed further by using custom developed electronics (see Chapter II).

Finally, the signals were digitalized by an A/D-converter (National Instruments) with a sampling frequency of 100 kHz and stored on the hard disc of a PC. During measurements, the sample was kept at a constant temperature of 30 ± 0.5 °C by using a custom heating system that covers the sample chamber (Fig. 3.4).

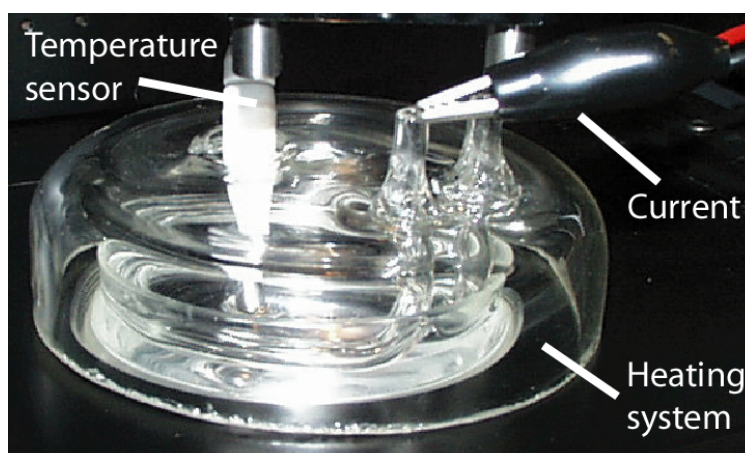


FIGURE 3.4 Temperature control system.

3.2.4 Measurements

First, the stiffness of the optical trap was calibrated in water. Subsequently, the viscosity values of well characterised Newtonian fluids (glycerine/water solutions) were measured by monitoring the Brownian motion of trapped polystyrene beads within optical tweezers. Measurements were made for increasing values of glycerine concentration, and the obtained viscosity values are compared with literature values. Three different data evaluation (corner frequency, autocorrelation analysis and histogram method) were applied and checked for their accuracy and efficiency.

3.2.4.1 *Trap stiffness*

The stiffness of the optical trap at increasing laser powers (from 45 to 70 mW) was fitted from the Brownian motion of a trapped bead by applying the histogram method. The diameter of the beads was $0.91\ \mu\text{m}$. According to Eq. (3.1), in the limit $r \approx 0$ a linear relationship between stiffness and laser power could be verified. The linear fit of the stiffness values along the x -axis is shown in Fig. 3.5.

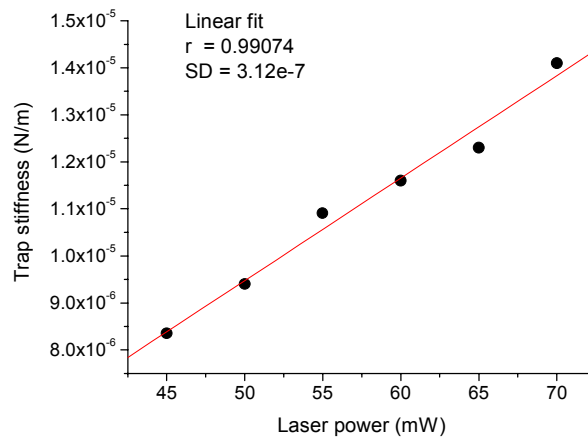


FIGURE 3.5 Measurement of the stiffness of the optical trap along the x -axis at different laser powers.

At a laser output power of 55 mW (power used for the viscosity measurements), the trap stiffness is $1.09 \cdot 10^{-5}$ N/m.

3.2.4.2 *Viscosity of glycerine/water mixtures*

Measurements were performed for the following values of glycerine concentration (% w/w): 0, 10, 15, 20, 25, 30, 40, and 50. Every measurement lasted for one second, generating 10^5 data points. For every glycerine concentration, fifteen measurements were made and evaluated. When evaluating the Brownian motion of the bead, only one transversal axis of motion, parallel to one side of the four-quadrant photodiode, was analyzed. It was assumed that the position of the bead along the chosen direction is directly proportional to the voltage difference between the corresponding photodiode quadrants. For every measurement, it was checked that the Boltzmann distribution obtained by histogramming the computed voltage differences can be indeed fitted by a Gaussian distribution, as shown in Fig. 3.6 for a typical measurement.

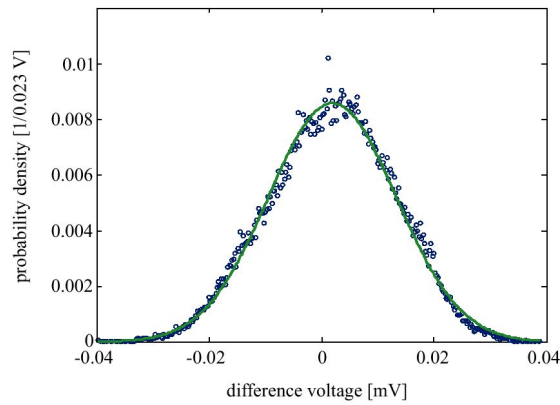


FIGURE 3.6 Histogram of the position values (as voltage differences between opposite halves of the photodiode) of a typical measurement (glycerine concentration 20%, measurement time = 1 s yielding 10^5 position values). Solid line is a fit of a Gaussian distribution to the histogram.

This check verified the assumption of a linear dependence between voltage difference and position as well as the assumption of a quadratic trapping potential. Next, values of $\kappa = k/\gamma$ were calculated by using all three methods described in the theoretical section (corner frequency, autocorrelation, position change histogramming). For all three methods, a non-linear Nelder-Mead simplex algorithm was used for numerical fitting [Nelder 1965]. A typical result for the corner frequency method is shown in Fig. 3.7.

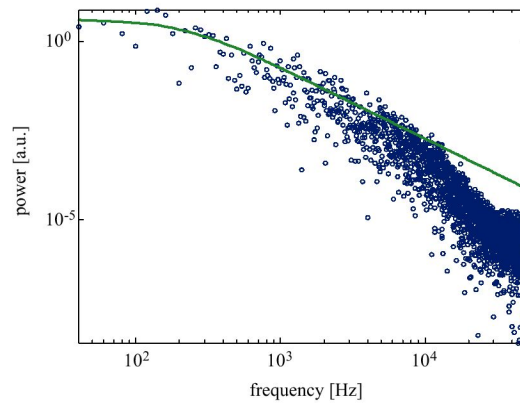


FIGURE 3.7 Power spectrum of the position-versus-time data for the same sample as being used in Fig. 3.5. Solid line is a fit according to Eq. (3.8).

The fit quality is relatively poor, showing large deviations between fit and data at higher frequencies, which was seen for all measurements. A possible explanation for the poor fit quality is the presence of broad-band mechanical

vibrations in the experimental set-up, although no distinct vibration resonances can be discerned in Fig. 3.6. In contrast, the autocorrelation function is fitted much better by its theoretical curve, as demonstrated in Fig. 3.8.

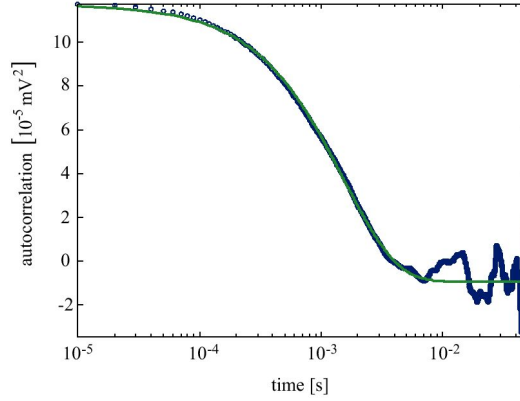


FIGURE 3.8 Semilog-plot of the position-versus-time autocorrelation for the same sample as being used in Fig. 3.5. Solid line is a fit according to Eq. (3.9).

The same is true for the histogram method. Fig. 3.9 shows the position change histograms and the corresponding Gaussian fits for several delay times ($\tau = 2^j \times 10\text{ms}$, $j = 1, \dots, 10$).

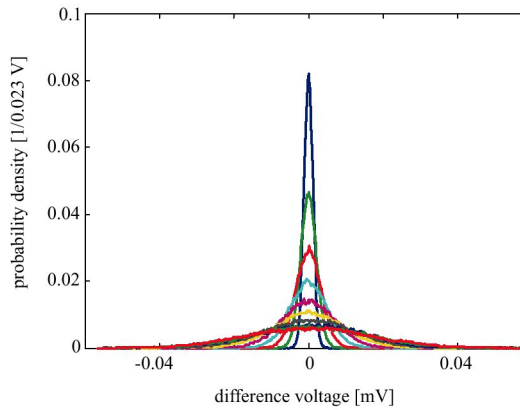


FIGURE 3.9 Histogram of the position changes for different delay times $\tau = 2^j \times 10 \mu\text{sec}$, $j=1, \dots, 10$, for the same data as used in the previous figures. For increasing delay time, the distributions become flatter and broader, reaching a stationary shape for large delay times.

The temporal evolution of the corresponding square variance values $\sigma^2(\tau)$ of these distributions is shown in Fig. 3.10, together with the fitted theoretical curve, see Eq. (3.11).

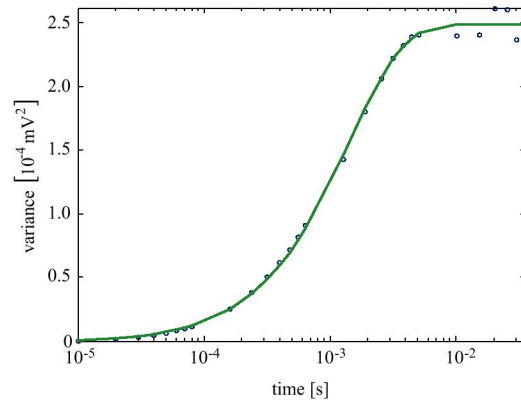


FIGURE 3.10 Temporal evolution of the mean square deviation of the histograms from the previous figure. The solid line is a fit according to Eq. (3.11).

The main fit parameter in all three methods is the frequency $\kappa = k/\gamma$. The calculated mean values of κ for all measured glycerine concentrations and for all three data evaluation methods are presented in Fig. 3.11. As can be seen, the autocorrelation and the histogram method give similar numerical values, whereas the values obtained from the corner frequency method are considerably larger.

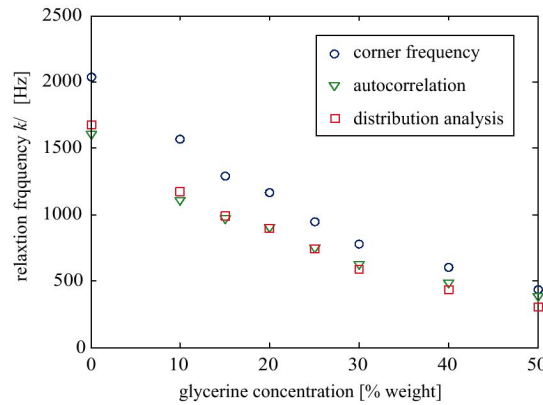


FIGURE 3.11 Mean values of the frequency $\kappa = k / \gamma$ as computed by three different data evaluation methods. For each glycerine concentration, fifteen measurements were made.

In Fig. 3.12, the mean square deviations are shown for all measured glycerine concentrations, given separately for every of the three applied methods. The corner frequency shows the largest deviations of κ from its mean value, and the histogram method the smallest, working best at all measured concentrations.

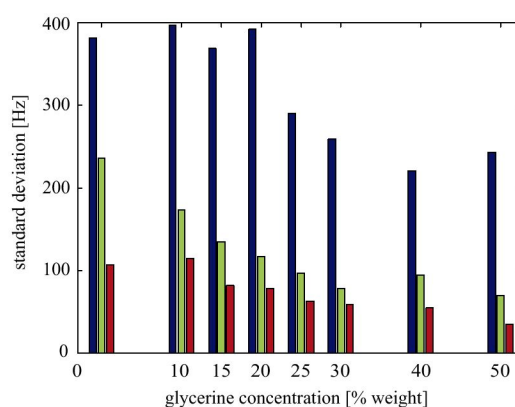


FIGURE 3.12 Mean square deviations of the κ -values when using the three different data evaluation methods. The first bar on the left refers to the corner frequency method, the second bar to the autocorrelation frequency method, and the third bar to the histogram method. For each glycerine concentration, fifteen measurements were used for computing the mean square deviation.

Knowing the values of κ for the different glycerine concentrations, viscosity values were derived while using the values for pure water as reference values. The resulting viscosity curve is shown in Fig. 3.13. For comparison, literature values of the viscosities are also shown (obtained from the Dow Chemical Company, www.dow.com/glycerine).

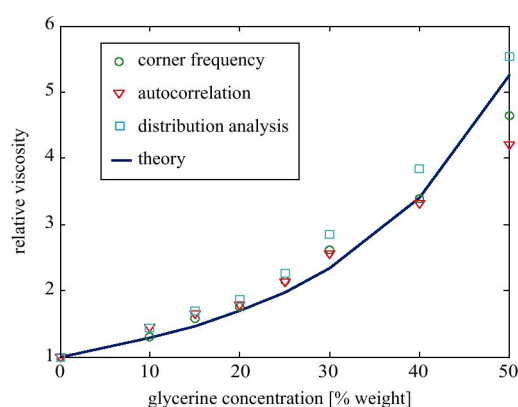


FIGURE 3.13 Viscosity values of the glycerine/water mixtures derived from the mean κ -values as shown in Fig. (3.10). For comparison, literature values of the viscosity are also shown (solid line). For computing absolute viscosity values, the experimental and theoretical values for pure water were used as a reference point.

When calculating the viscosity values, it was assumed that the strength of the optical trap does not change when varying the glycerine concentration. However, a more correct approach has to take into account that the

refractive index of a glycerine/water solution slightly increases with increasing glycerine concentration. In the simple point-dipole description of an optical trap (Paragraph 3.2.2), the trapping force is proportional to the polarizability of the particle (α). For a spherical particle within a homogeneous electric field, the value of α and thus the strength of the optical trap is proportional to

$$(n_{bead}^2 - n_{medium}^2) / (n_{bead}^2 + 2n_{medium}^2), \quad (3.12)$$

where n_{bead} is the refractive index of the bead and n_{medium} that of the surrounding solution. Fig. 3.14 shows the calculated viscosity values when taking into account that the strength of the trap changes according to Eq. (3.12). The necessary values n_{medium} for the various glycerine concentrations were taken from the Dow Chemical Company (www.dow.com/glycerine).

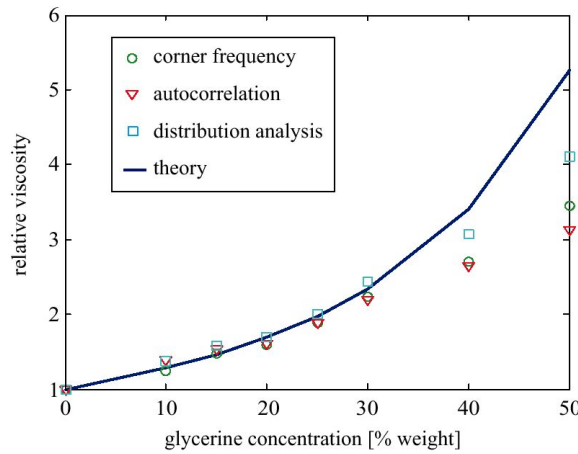


FIGURE 3.14 Same as Fig. 3.12 but taking into account that the strength of the optical tweezers, k , is changing with increasing glycerine concentration as given by Eq. (3.12).

3.2.4.3 Discussion

In summary, an optical trapping set-up was developed for conducting microrheological experiments in solutions. The performance of the set-up was tested by measuring the local viscosity in mixtures of glycerine and water. The results were compared with bulk values obtained from the literature. Two established methods for evaluating the Brownian motion in an optical trap, namely the computation of the “corner frequency” and of the autocorrelation function were compared with a new approach called here the “histogram method”. It was verified that the histogram method is the most robust method for evaluating the Brownian motion of a trapped particle

within an optical trap, whereas the corner frequency shows large errors in fitting the experimental data. As can be seen by comparing Fig. 3.12 and Fig. 3.13, the trap-strength corrected values fit the literature values much better at low glycerine concentrations, showing that even small changes in the refractive index of the solution have to be taken into account for correctly evaluating optical trap data. This is especially important when applying the method for measuring the viscosity in complex media such as living cells. The viscosity values of the glycerine solutions that were derived from the experimental data agree well with the literature values at glycerine concentrations below 30 %. Remarkably, at glycerine concentrations larger than 30 %, the derived viscosity values are systematically larger than their actual values. A possible explanation is that the trap geometry becomes more complicated for larger glycerine concentrations: In the experimental set-up, laser focusing was done with an oil-immersion objective with 1.4 N.A. at a distance of ca. 6 μm above the glass surface. It is well known that the resulting light intensity distribution shows several maxima along the optical axis, due to the refractive index mismatch between the immersion oil/glass and the glycerine/water solution (Fig. 3.15) [Török 1997, Dogariu 1999, Enderlein 2002]. For larger glycerine concentrations, the trapping force gets smaller which may cause the bead to switch between the two strongest intensity maxima, making its motion more complicated than that within a simple square potential. Such a switching would not necessarily be discernible from the Boltzmann distribution, which could still resemble a Gaussian distribution. The deviation of the measured viscosity values from the literature data at larger glycerine concentration could also be explained by considering that at larger viscosity values, the amplitudes of environmental mechanical noise may become comparable to that of the Brownian motion itself (see also Chapter II – Fig. 2.22, about the “fixed-bead noise”), so that spurious displacements are introduced into the measurement. Thus, further improvements in the set-up should include (1) a better isolation from environmental noise, (2) substituting the oil-immersion objective used for trapping with a water-immersion objective, avoiding the negative effects due to the refractive index mismatch. The work presented in this chapter is a first step towards the measurement of viscoelastic properties in more complex systems like the cytoplasm of a cell. The developed histogram method for data evaluation will be of great use in such applications.

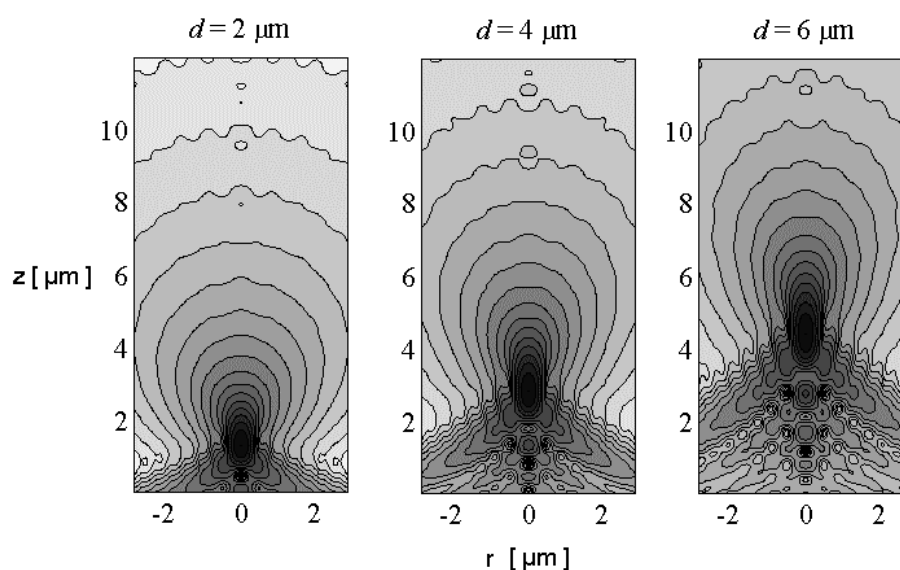


FIGURE 3.15 Calculated light intensity distribution in the focal region for increasing distances from the chamber's bottom. The refractive index mismatch between the immersion oil and the solution produces multiple foci at $d = 6 \mu\text{m}$.

3.3 *Scanning probe microscopy with optical tweezers*

3.3.1 Introduction

The term *scanning probe microscopy* refers to several related technologies (about two dozens) for imaging and measuring surface properties on a microscopic to nanoscopic scale, down to the level of molecules and groups of atoms. The first scanning probe microscope was the *scanning tunneling microscope* (STM) invented by Gerd Binnig and Heinrich Rohrer [Binnig 1982]. Binnig and Rohrer were awarded the Nobel Prize in Physics in 1986 for their development of the STM. In 1986, Binnig developed also the *atomic force microscope* (AFM) [Binnig 1986]. With AFM, non-conductive samples can be imaged down to atomic resolution. Since 1986, several techniques closely related to STM and AFM have been developed (see Amato 1997 for the history of the development of SPM techniques). SPM technologies share the concept of scanning an extremely sharp tip (3-50 nm radius of curvature) across the object's surface. The tip is mounted on a flexible cantilever. When the tip moves in proximity to the investigated

object, forces of interaction between the tip and the surface influence the movement of the cantilever. These movements are detected by suitable sensors. Various interactions can be studied depending on the probe sensors used. The ability of SPM to image at atomic resolution, combined with its ability to image a wide variety of samples under a wide variety of conditions, has created a great deal of interest in applying it to the study of biological structures. In the literature, images of DNA, single proteins, structures such as gap junctions, and living cells can be found [for a review see Hoh 1992]. Unfortunately, SPM techniques cannot image all samples at atomic resolution. The apex radii of available tips restricts atomic resolution to flat, periodic samples such as silica or graphite. In addition, because biological structures are soft, the tip-sample interaction tends to distort or destroy them. Soft samples are often severely damaged by the AFM-tip when scanning in contact mode, even in an aqueous environment. Adhesive tracking forces, which can exceed 20 nN [Bushell 1999], and the cantilever mechanical stiffness can induce displacement or distortion of surface structures. Such problems can be partially avoided when applying the so-called *tapping mode*. Nonetheless, only stiff structures like the cytoskeleton are visible when imaging with an SPM apparatus.

Recent studies [Ghislain 1993, Florin 1996, Florin 1997, Stout 1998, Friesen 1999, Hörber 2000, Pralle 2000] show that an optically trapped probe can be used for imaging of soft biological samples. In the so-called “optical force microscope” (OFM), the mechanical cantilever used in SPM is replaced by the gradient force, and the SPM-tip by a trapped probe. A OFM probe is generally a dielectric microsphere with diameter between 0.2 and 1 μm . Nanometer-sized metallic particles were also employed [Kawata 1994, Sugiura 1997, Sugiura 1998]. The advantage of an optical force microscope over SPM is the very low trap stiffness in comparison to mechanical cantilevers. The stiffness of the trap is typically in the range of $10^{-5} - 10^{-6}$ N/m against a typical cantilever stiffness of 10^{-1} N/m, so that sample damage is definitely avoided during scanning.

In this work, an optical-force microscope set-up featuring back-scattered light feedback control and fluorescence detection was developed. Preliminary experiments on cells were conducted.

3.3.2 Set-up

The set-up (Fig. 3.16) is very similar to the system previously described in Chapter II and in this chapter.

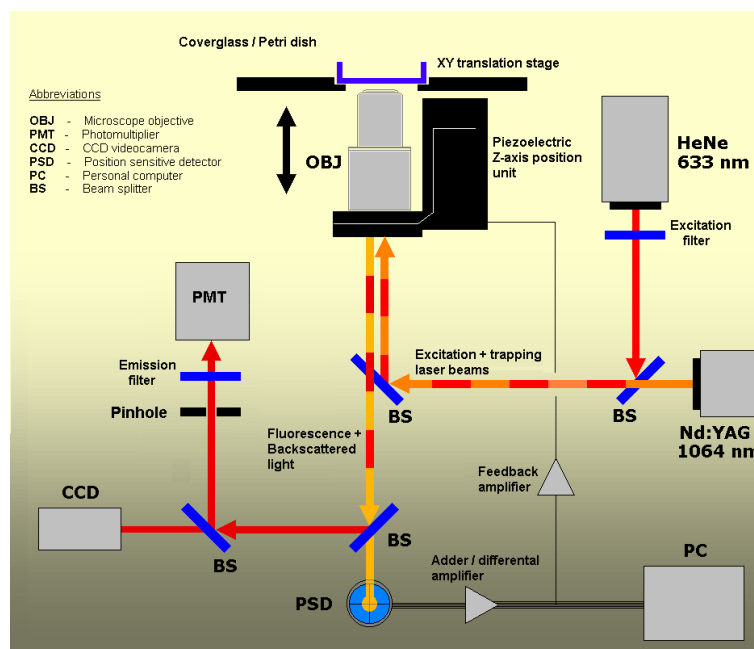


FIGURE 3.16 Optical force microscope set-up.

The same objective that is used for trapping is also employed for collecting the IR-light which is scattered back by the trapped probe. The light is directed toward a four-quadrant position-sensitive photodiode operating in photovoltaic mode. The sum of the voltage values which are coming from each of the four quadrants is proportional to the position of the probe along the optical axis. A precision mechanical *xy*-stage (Märzhäuser, Wetzlar, Germany) with a maximum step resolution of 0.1 μm is used for scanning the sample. Moreover, a He-Ne laser with a wavelength of 633 nm is coupled into the objective, allowing fluorescence excitation of molecules labelled with chromophores absorbing in the red region of the spectrum. Fluorescence emission is recorded by a high-sensitive CCD-camera. Confocal detection of fluorescence is also possible. The principle of the back-scattered light feedback control is shown in Fig. 3.17. The sum-signal from the photodiode is processed by a dedicated analogue feedback circuit (alternatively signal-processing is digitally performed by an acquisition

routine written in Visual Basic) and coupled to the piezoelectric focusing unit, closing a negative-feedback loop which restores the desired back-scattered light level while the xy -stage advances. Since the piezoelectric focusing unit is calibrated, the voltages applied during feedback is directly proportional to the bead displacement.

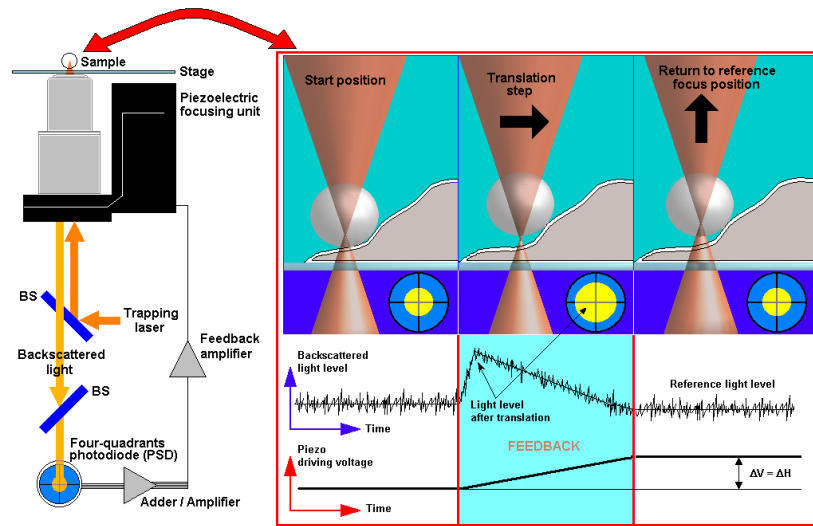


FIGURE 3.17 Principle of back-scattered light feedback control.

Fig. 3.18 shows the principle of the scanning of the trapped probe over the membrane of a cell. The probe is placed on the membrane at a starting position and scanned along parallel lines. The step resolution of the line scanning was $0.1 \mu\text{m}$ for most of the experiments.

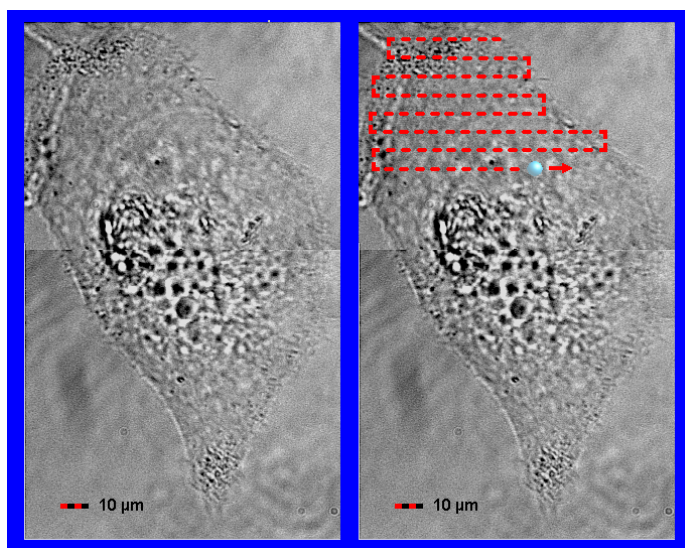


FIGURE 3.18 Surface scanning of a cell membrane with the trapped probe.

3.3.3 Measurements

The experiments were conducted on erythroleukemia cells immersed in PBS saline buffer. The cells were cultured in special plastic Petri-dishes (PetriPermTM) with an about 120 μm -thick bottom, or in the sample chamber developed for the microrheology experiments (see Paragraph 3.2.3). In order to reduce the sticking of the probe on the membrane (due both to the roughness of the surface and to cellular adhesion proteins), 10 to 50 μl of fish-skin protein (Aldrich) were added to the medium. The frame sequence shown in Fig. 3.19 shows the probe positioning before starting the scan routine on the cell surface. In a typical experiment, the probe (a polystyrene bead with a diameter of 900 nm) is trapped with the maximum laser power available (300 mW) and brought close to the cell membrane (first and second frame). Subsequently (third frame), the optical trap is translated several micrometers along the z -direction, in order to reach the surface level of the cell (typically, the thickness of the cells used for the experiments is 25-30 μm). Once the probe is located on the cell membrane, scanning is started (last frame).

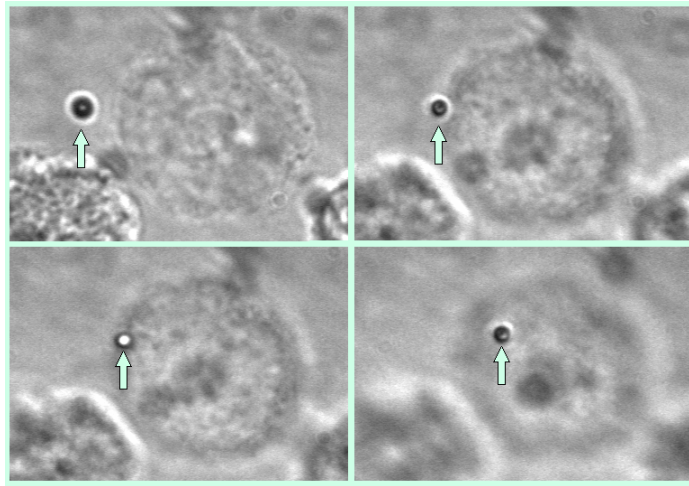


FIGURE 3.19 Initial positioning of the probe on the cell membrane.

The surface topography of the cell membrane across a small area ($5\ \mu\text{m}$ long, $0.2\ \mu\text{m}$ wide) is shown in Fig. 3.20.

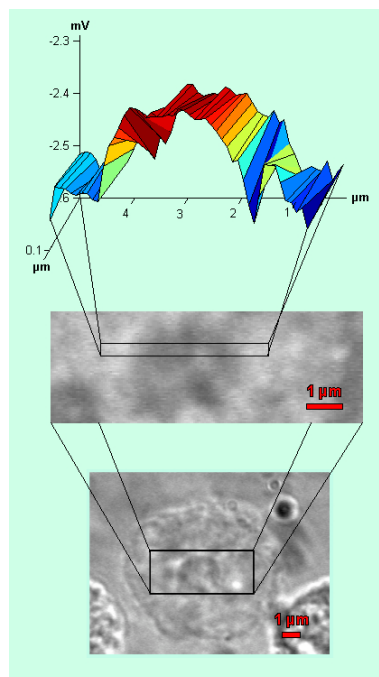


FIGURE 3.20 Surface scanning of a cell membrane with the trapped probe.

The scanning of this tiny section of the membrane highlights a protrusion rising outward from the cell surface for about two micrometers (probably the cell nucleus). The same feature can be observed two-dimensionally with

the optical microscope. In this preliminary experiments the feedback system was not applied, hence only the response signal from the photodiode is recorded (z-axis position). A common problem that arises during scanning of the membrane is that the adhesion forces between the probe and the surface are often stronger than the trapping force, so that the probe eventually escapes from the optical tweezers, interrupting the scanning. Unfortunately, this problem could not be satisfactorily solved by adding an anti-sticking substance such as fish-skin protein or bovine serum albumine (BSA). Therefore, only imaging of small areas of the membrane (typically few μm^2) was successfully achieved in this work.

3.3.4 Discussion

The potentials and limitations of scanning probe microscopy based on optical tweezers (optical force microscope) were studied in this chapter. At present, the principal limitation of this new technique is that the imaging of biological specimens is severely hampered by non-specific adhesion between the probe and the sample leading to the loss of the probe during scanning. On one side, the extremely weak load exerted by an optically trapped probe avoids the damages and artifacts produced by conventional SPM techniques when measuring on soft materials. On the other side, the trapping forces are often too weak to overcome the non-specific adhesion between the probe and the sample. The spatial resolution of OFM, i.e. the size of the smallest structure discernible is related to the diameter of the trapped probe (from some ten nanometer for a metal particle up to hundreds of nanometers for a latex bead). Thus, the resolution of OFM is near the resolution of non-contact SPM (Fig. 3.21).

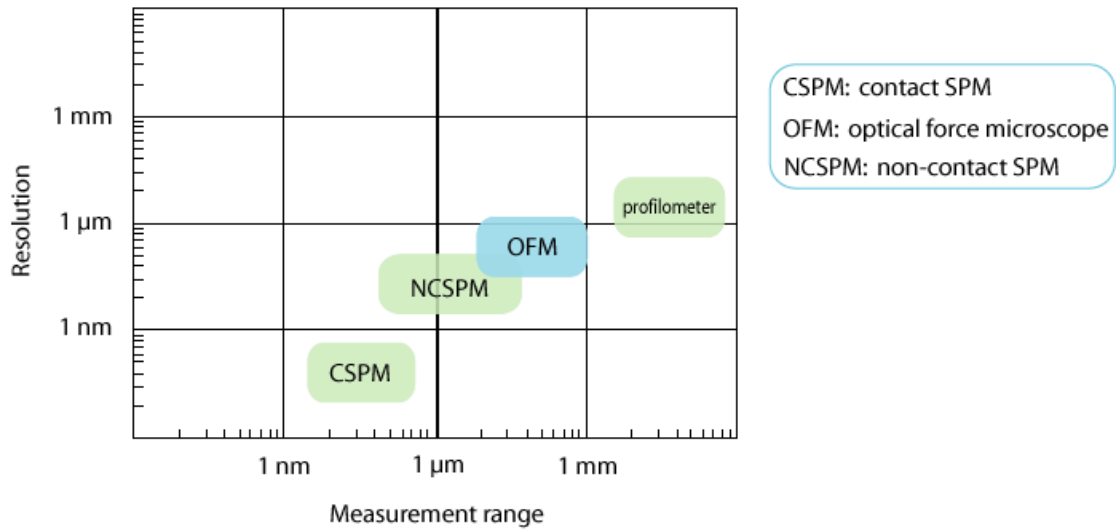


FIGURE 3.21 Comparison between the spatial resolution of OFM and that of different scanning techniques.

The experiments clarified that the detection of back-scattered light (as done in this work) can induce artifacts in the measurements, due to the inhomogeneous refractive index of most biological samples. The same problem arises when detecting the forward-scattered light, as done by Pralle et al. [Pralle 2000]. Ideally, the tracking beam should be reflected by the trapped probe without traversing the sample. Thus, optical tweezers based on an upward-microscope configuration should be preferred for OFM experiments. Alternatively, a second illuminating beam separated from the trapping laser may be used.

A decisive technical advancement for optical force microscopy would be the association of a magnetic field force to the gradient force of light [Sacconi 2001]. The gradient force stabilizes the particle laterally, while the magnetic field produces an additional axial stiffness, which should overcome the sticking of the probe at the surface. Obviously, one would have to use dielectric particles with paramagnetic properties as the probe.

References

- [Bartlett 2001] Bartlett P., Henderson S. I., Mitchell S. J.
Measurement of the hydrodynamic forces between two polymer-coated spheres.
Phil.Trans.R.Soc.Lond. A 359: 1-13 (2001)
- [Binnig 1982] Binnig, G., Rohrer, H., Gerber C., Weibel E.
Surface studies by scanning tunneling microscopy.
Phys. Rev. Lett. 49: 57-61 (1982)
- [Binnig 1986] Binnig, G., Quate, C.F., Gerber, Ch.
Atomic force microscope.
Phys. Rev. Lett. 56(9), 930-933 (1986)
- [Bushell 1999] Bushell G. R., Cahill C., Clarke F. M., Gibson C. T., Myhra S., Watson G. S.
Imaging and force-distance analysis of human fibroblasts in vitro by atomic force microscopy.
Cytometry 36:254-264 (1999)
- [Clapp 2001] Clapp A. R., Dickinson R. B.
Direct measurement of static and dynamic forces between a colloidal particle and a flat surface using a single-beam gradient optical trap and evanescent wave light scattering.
Langmuir 17: 2182-2191 (2001)
- [Crocker 1996] Crocker J. C., Grier D. G.
Methods of digital video microscopy for colloidal studies.
J. Colloid Interface Sci. 179: 298-310 (1996)
- [Crocker 1997] Crocker J.C.
Measurement of the hydrodynamic corrections to the brownian motion of two colloidal spheres.
J. Chem. Phys. 106: 2837-2840 (1997)
- [Crocker 2000] Crocker J. C., Valentine M. T., Weeks E. R., Gisler T., Kaplan P. D., Yodh A. G., Weitz D. A.
Two-point microrheology of inhomogeneous soft materials.
Phys. Rev. Lett. 85: 888-891 (2000)
- [Dogariu 1999] Dogariu A., C. R. Rajagopalan
Optical traps as force transducers: the effects of focusing the trapping beam through a dielectric interface.
Langmuir 16: 2770-2778 (2000)
- [Enderlein 2002] Enderlein J., Böhmer M.
Calculation of the light collection efficiency function in fluorescence correlation spectroscopy.
J. Opt. Soc. Am. A, submitted
- [Florin 1996] Florin E.-L., Hörber J.K.H., Stelzer E.H.K.
High-resolution axial and lateral position sensing using two-photon excitation of fluorophores by a continuous-wave Nd:YAG laser.
Appl. Phys. Lett. 69: 446-448 (1996)
- [Florin 1997] Florin E.-L., Pralle A., Hörber J.K.H., Stelzer E.H.K
Photonic force microscope based on optical tweezers and two-photon excitation for biological applications.
J. Struct. Biol. 119: 202-211 (1997)

- [Florin 1998] Florin E.-L., Pralle A., Stelzer E.H.K., Hörber J.K.H.
Photonic force microscope calibration by thermal noise analysis.
Appl. Phys. A: (1998)
- [Frieze 1999] Frieze M.E.J., Truscott A.G., Rubinsztein-Dunlop H., Heckenberg N.R.
Three-dimensional imaging with optical tweezers.
Appl. Opt. 38: 6597-6603 (1999)
- [Ghislain 1993] Ghislain L.P., Webb W.W.
Scanning-force microscope based on an optical trap.
Opt. Lett. 18: 1678-1680 (1993)
- [Allersma 1998] Allersma M.W., Gittes F., deCastro M.J., Stewart R.J., Schmidt C.F.
Two-dimensional tracking of ncd motility by back focal plane interferometry.
Biophys. J. 74: 1074-1085 (1998)
- [Grier 1997] Grier D.G.
Optical tweezers in colloid and interface science.
Curr. Opin. Colloid Interface Sci. 2: 264-270 (1997)
- [Hoh 1992] Hoh, J.H. Hansma, P.K.
Atomic force microscopy for high-resolution imaging in cell biology.
Trends Cell Bio. 2, 208-213 (1992)
- [Hörber 2000] Hörber H., Florin E.-L., Stelzer E.
Photonische Kraftmikroskopie.
Physikalische Blätter 56: 41-44 (2000)
- [Hough 1999] Hough L.A., Ou-Yang H.D.
A new probe for mechanical testing of nanostructures in soft materials.
J. Nanoparticle Res. 1: 495-499 (1999)
- [Kawata 1994] Kawata S., Yasushi I., Sugiura T.
Near-field scanning optical microscope with a laser trapped probe.
Jpn. J. Appl. Phys. 33: L1725-L1727 (1994)
- [Lin 2000] Lin B., Yu J., Rice S. A.
Direct measurements of constrained Brownian motion of an isolated sphere between two walls.
Phys. Rev. E 62: 3909-3919 (2000)
- [Lin 2000b] Lin B., Yu J., Rice S. A.
Diffusion of an isolated colloidal sphere confined between flat plates.
Colloids and Surfaces A: Physicochemical and Engineering Aspects 174: 121-131 (2000)
- [Lin 2001] Lin K., Crocker J. C., Zeri A. C., Yodh A. G.
Colloidal interactions in suspensions of rods.
Phys. Rev. Lett. 87: (2001)
- [MacKintosh 1999] MacKintosh F.C., Schmidt C.F.
Microrheology.
Curr. Op. in Coll. Interf. Sci. 4: 300-307 (1999)
- [Mason 1995] Mason T. G., Weitz D. A.
Optical measurements of frequency-dependent linear viscoelastic moduli of complex fluids.
Phys. Rev. Lett. 74: 1250- (1995)

- [Mason 1997] Mason, T. G. Ganesan K., van Zanten J. H., Wirtz D., Kuo S. C.
Particle Tracking Microrheology of Complex Fluids.
Phys. Rev. Lett. 79: 3282-3285 (1997)
- [Meiners 1999] Meiners J.-C., Quake S.R.
Direct measurements of hydrodynamic cross correlations
Between two particles in an external potential.
Phys. Rev. Lett. 82: 221-2214 (1999)
- [Mukhopadhyay 2001] Mukhopadhyay A., Granick S.
Micro- and nanorheology
Curr. Op. in Coll. Interf. Sci. 6: 423-429 (2001)
- [Nelder 1965] Nelder J. A., Meade R.
Comput. J. 7: 308- (1965)
- [Peters 1999] Peters I.M., van Kooyk I., van Vliet S.J., de Grooth B.G., Figdor
C.G., Greve J.
3D single -particle tracking and optical trap measurements on
adhesion proteins.
Cytometry 36: 189-194 (1999)
- [Pralle 1998] Pralle A., Florin E.-L., Stelzer E.H.K., Hörber J.K.H.
Local viscosity probed by photonic force microscopy.
Appl. Phys. A 66: 71-73 (1998)
- [Pralle 2000] Pralle A., Florin E.-L., Stelzer E. H. K., Hörber J. K. H.
Photonic force microscopy: a new tool providing new methods to
study membranes at the molecular level.
Single Mol. 1: 129-133 (2000)
- [Sacconi 2001] Sacconi L., Romano G., Ballerini R., Capitanio M., De Pas M.,
Giuntini M.
Three-dimensional magneto-optic trap for micro-object
manipulation.
Opt. Lett. 26: 1359-1361(2001)
- [Sako 1998] Sako Y., Nagafuchi A., Tsukita S., Takeichi M., Kusumi A.
Cytoplasmic regulation of the movement of E-cadherin on the free
cell surface as studied by optical tweezers and single particle
tracking:
corralling and tethering by the membrane skeleton.
J. of Cell Biol. 140: 1227-1240 (1998)
- [Stout 1998] Stout A.L., Webb W.W.
Optical force microscopy.
Methods in cell biology 55: 99-115 (1998)
- [Sugimoto 1997] Sugimoto T., Takanashi T., Itoh H., Sato S., Muramatsu A.
Direct measurement of interparticle forces by the optical trapping
technique.
Langmuir 13: 5528-5530 (1997)
- [Sugiura 1997] Sugiura T., Okada T.
Gold-bead scanning near-field optical microscope with laser-force
position control.
Opt. Lett. 22: 1663-1665 (1997)
- [Sugiura 1998] Sugiura T., Kawata S., Okada T.
Fluorescence imaging with a laser trapping scanning near-field
optical microscope.
J. Microscopy 194: 291-294 (1999)

- [Tlusty 1998] Tlusty T., Meller A., Bar-Ziv R.
Optical gradient forces of strongly localized fields.
Phys. Rev. Lett. 81: 1738-1741 (1998)
- [Török 1997] Török P., Varga P.
Electromagnetic diffraction of light focused through a stratified medium.
Appl. Opt. 36, 2305-2312 (1997)
- [Valentine 1996] Valentine M.T., Dewalt L.E., Ou-Yang H.D.
Forces on a colloidal particle in a polymer solution: a study using optical tweezers.
J. Phys. Condens. Matter 8: 9477-9482 (1996)
- [Valentine 2001] Valentine M. T., Kaplan P. D., Thota D., Crocker J. C., Gislser T., Prud'homme R. K., Beck M., Weitz D.A.
Investigating the microenvironments of inhomogeneous soft materials with multiple particle tracking
Phys. Rev. E 64: (2001)
- [Verma 1998] Verma R., Crocker J. C., Lubensky T. C., Yodh A. G.
Entropic colloidal interactions in concentrated DNA solutions.
Phys. Rev. Lett. 81: 4001-4004 (1998)
- [Verma 2000] Verma R., Crocker J. C., Lubensky T. C., Yodh A. G.
Attractions between hard colloidal spheres in semiflexible polymer solutions.
Macromolecules 33: 177-186 (2000)
- [Xu 1998] Xu J., Palmer A., Wirtz D.
Rheology and microrheology of semiflexible polymer solution.
Macromolecules 31: 6486-6492 (1998)
- [Yamada 2000] Yamada S., Wirtz D., Kuo S.C.
Mechanics of living cells measured by laser tracking microrheology.
Biophys. J. 78: 1736-1747 (2000)

Compact optical tweezers using aspherical optics

4.1 Introduction

4.1.1 Motivation: why compact optical tweezers

The design and implementation of conventional optical tweezers are affected by several technical constraints. One constraint is the large size of the set-up, usually comprising of a laser, optics for expanding and steering the beam, and a microscope. Other limitations are imposed by the properties of the high-numerical-aperture objectives employed in optical trapping. Such objectives have a very short working distance (around 250 μm) and are designed to work only in association with an immersion medium (generally oil or water). Furthermore, their imaging and focusing properties are optimized only for a defined cover-slip thickness (generally 170 μm). Consequently, optical trapping of objects within chambers with thicker bottoms (like the 1 mm thick plastic petri-dishes usually employed in biology) is not achievable with conventional optical tweezers. Special reservoirs and chambers with very thin walls must often be purchased or fabricated. Thus, improving optical tweezers towards trapping samples through thick substrates or deep into a reservoir could greatly enhance the utility of this technique. For bypassing the constraints of conventional optical tweezers, several alternative set-ups were proposed in the literature. In all the described systems, optical confinement and trapping of micrometer-sized particles was achieved by using optical fibers for focusing the laser beam onto the sample. By using two coaxially aligned optical fibers, Constable et al. [Constable 1993] developed a new version of the

*optical fiber
laser tweezers*

*disadvantages of
optical fiber
tweezers*

original dual-beam optical trap configuration of Ashkin [Ashkin 1970a]. In the dual-beam approach, a particle is trapped at the position where the scattering forces exerted by two counter-propagating Gaussian laser beams balance each other. In the work of Constable, two-dimensional optical confinement and translation of micrometer-sized dielectric particles was successfully demonstrated employing two laser beams emerging from two exactly aligned fiber ends. In order to improve the efficiency of the dual-fiber trapping set-up, tapered and hemispherically lensed fibers were also employed [Lyons 1995]. With a lensed optical fiber, a micro-object can be more easily trapped and manipulated in comparison to a cleaved fiber, because of the stronger transversal trapping efficiency [Lyons 1995; Taguchi 1997]. Two-dimensional translation of micro-objects by using a single lensed optical fiber was also reported [Taguchi 2001]. Optical trapping in three-dimensions was demonstrated by using a multiple optical fiber system [Taguchi 2000]. Although optical-fiber tweezers help to avoid some constraints of conventional optical tweezers, particularly those imposed by the high N.A. objectives (like limited working distance and very thin chamber walls), some disadvantages of this approach limit its use in routine applications, particularly in biology. The first disadvantage is that the procedure required for aligning and fixing the fibers is difficult, although an improved set-up accomplished with micromachining techniques has been recently proposed [Collins 1999]. Second, optical trapping inside a hermetically sealed and sterile environment (which is one of the most remarkable advantages of optical trapping over mechanical micro-manipulation techniques) cannot be achieved, because the fiber assembly has to be introduced into the chamber each time. Third, only trapping in two dimensions can be easily done, and even the set-up proposed by Taguchi et. al. [Taguchi 2000] does not allow feasible three-dimensional manipulation of the trapped particle. Thus, alternative methods would be desirable for circumventing the limitations of conventional optical tweezers in order to miniaturize its size and to further extend its applicability. A promising approach is substituting the microscope objective that is conventionally used in optical tweezers with a single aspherical lens. Aspherical lenses are employed as focusing elements in household CD and CD-ROM drives, which have seen impressive advancements both in miniaturization and performance during the last two decades. Particularly, the optics employed in optical pick-ups of CD-ROM and CD-players has been optimized for focusing the reading laser beam to a spot that maintains diffraction-limited

*using optics
from compact
disk technology*

quality even after traversing very thick (1.2 mm) plastic substrates. In this work, such a CD aspherical objective lens is used for building a new compact optical tweezers.

4.1.2 The optical pickup of a compact disc drive

Household compact disc drives are sophisticated devices featuring an amazing interplay of complex electronics and precision optics. A CD-drive consists of five core components: 1. Disc drive system, 2. Laser pickup system, 3. Servo system, 4. Data decoding, 5. Control and display system. In Fig. 4.1 a simplified schematic of a typical CD-drive system is shown.

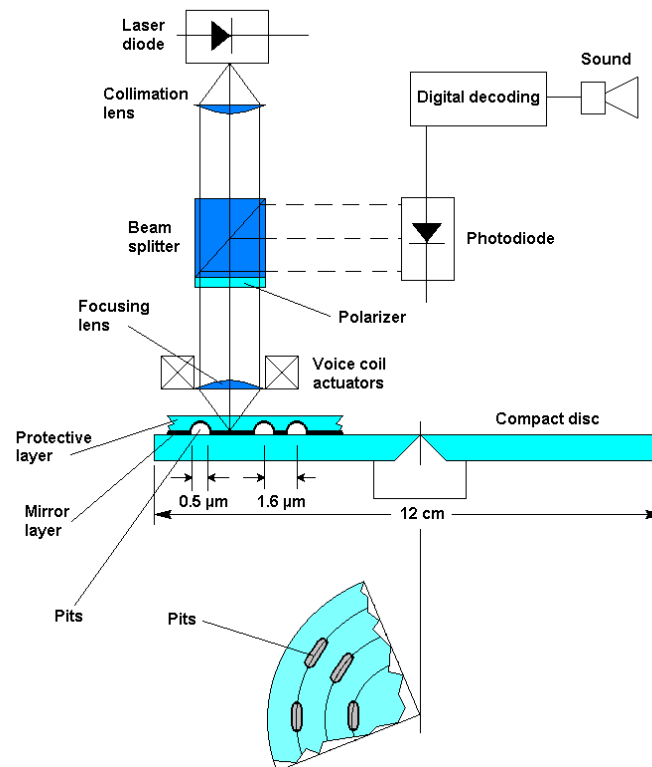


FIGURE 4.1 Typical compact-disc system.

characteristics of CD reading unit The most important component of a compact disc drive is the optical pickup, which reads the information encoded by the “lands” and “grooves” on the surface of the disk (Fig. 4.1). Basically, the optical imaging principles of a CD pickup are very similar to those of a confocal scanning microscope that uses coherent illumination. The CD reading unit must be able to distinguish single grooves that have a width of approximately $0.5\ \mu\text{m}$, a

length of 0.83 through 3.56 μm , and an optical height of $\lambda/8$. Moreover, the grooves are placed on different tracks separated by only 1.6 μm one from each other. The read-out of the disk is accomplished by scanning the spirally recorded track with a focused laser beam generated by a diode laser. The beam has usually a wavelength of 780 nm and optical power of less than 1 mW. During scanning, a photodiode array placed at the image plane of the focusing lens detects the light reflected by the grooves (bit 1) and lands (bit 0). Subsequently, the signal generated by the photodiodes is further processed by the digital decoding electronics. A tracking servo system is employed for maintaining the laser spot in focus and on the center of the disk track. Since the far-field diffraction pattern generated by the disk surface is asymmetric when the laser spot is positioned out of focus, a segmented photodiode (see also Paragraph 2.1.4) can be used to drive the tracking system with the help of a closed loop feedback control system. In other words, when the beam is properly focused, it projects a round beam onto the segmented photodiode, resulting in a zero bias voltage. On the contrary, when the disk is out of focus, an elongated spot is projected on the detector producing a non-zero bias voltage. Many CD players use three-beam scanning for correct tracking. A so-called “voice-coil” actuator (which has a bandwidth of several kHz) keeps the beam focused and on-track by precisely shifting the objective lens axially (focus adjustment) and laterally (spot centering). A close view of a widespread CD optical pickup (the KSS361A from Sony) is shown in Fig. 4.2. Further details about CD technology can be found in the specialized literature [Bouwhuis 1985; Goldwasser2001].

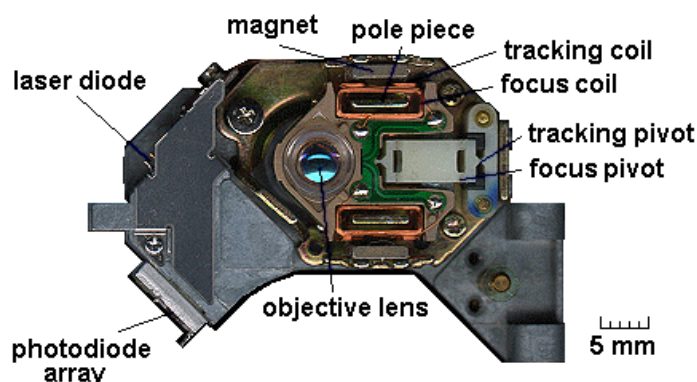


FIGURE 4.2 Sony KSS361A compact disc optical pickup (top view).

Aspherical plastic objective lenses have been widely used in optical pickups because they can replace a number of optical spherical elements and minimize spherical aberration. For spherical lenses, as the ratio of the focal length to the incident laser beam diameter decreases, the phenomenon of spherical aberration produces a broadening of the focal spot. This limits the minimum spot size that can be achieved with a lens with only spherical surfaces. By using aspherical lenses, it is possible to reach the fundamental diffraction limited spot size. An aspherical surface can be described numerically with an expression consisting of two parts – a conical section departure from a sphere, and aspherical deviations corresponding to higher polynomial terms. The expression determines the sag Z of the surface at any point h , where h is the height from the optical axis:

$$Z = \frac{ch^2}{1 + \sqrt{1 - \epsilon c^2 h^2}} + Ah^4 + Bh^6 + Ch^8 + Dh^{10} + \dots \quad (4.1)$$

where c is the curvature (1/radius) of the base sphere (at the optical axis or vertex), ϵ is the conic constant, and A, B, C, D are the aspherical coefficients of the 4th, 6th, 8th, 10th order respectively. Note that only even powers appear because of axial symmetry.

Injection molding is nowadays the most commonly method used for producing plastic objectives for optical drives [Kawai 1997]. The polymeric material preferentially used is poly(methyl methacrylate) (PMMA) which has a refractive index of 1.492. The focusing performance of such inexpensive plastic-molded lenses is comparable with that of a standard microscope objective with a numerical aperture of 0.45-0.60. These lenses can focus the monochromatic and coherent light of the laser diode into a diffraction-limited spot with a diameter of about 1.7 μm . The ideal diameter of the spot, corresponding to the full-width at half-maximum center of the Airy disk pattern can be easily calculated with the equation:

$$d = \frac{\lambda}{N.A.} \quad (4.2)$$

The aspherical surface profile of the lens is optimized for focusing the laser at distance of approximately 4 mm, including 1.2 mm thickness of the transparent polycarbonate protection layer of a compact disc (refractive index 1.551). Standard CD drive lenses have also an antireflective coating

optimized for a wavelength of 780 nm, usually emitted by diode lasers adopted in CD-drives. CD optics have already been integrated in other experimental systems, for example in optical profilometry systems [Tiribilli 1999].

4.2 *Compact optical tweezers*

4.2.1 Testing set-up

In this work, a new compact optical tweezers set-up based on an aspherical lens was built. First, the feasibility of achieving optical trapping by replacing a conventional microscope objective with such a focusing element was investigated with a testing set-up. The employed lens was obtained from a commercial compact disc optical pickup (Sony KSS361A). Relevant parameters of the lens are shown in Table 4.1.

Parameter	Value
Material	Poly(methyl methacrylate) (PMMA)
Material refractive index	1.492
Numerical aperture	0.45
Focal length	3.23 mm
Image-object distance	24.2 mm
Lateral magnification	5

TABLE 4.1 Relevant parameters of the objective lens from the pickup KSS361A of Sony. (source: Sony Corporation)

The geometrical design parameters of the lens are shown in Table 4.2. The lens has an aspherical surface on both its back and front sides. The material of the lens is PMMA.

Surface	Radius (mm)	Thickness (mm)	Glass	Conic ϵ	A	B	C	D
Front	2.3123	2.55	PMMA	-0.96223	0.1e-2	-0.31266e-4	-0.26893e-4	-0.31001e-5
Back	-3.86797			-7.96526	0.13604e-2	-0.31097e-4	-0.99255e-4	0.19701

TABLE 4.2 Design parameters of the aspherical lens (from HUNG 2000)

*description of
the testing set-up*

The testing set-up employed in the experiments is shown schematically in Fig. 4.3. The laser beam emitted by a diode-pumped solid state Nd:YAG laser (LCS-DTL-22, Laser Compact, Moscow, wavelength 1064 nm) is focused by using a 10× objective (Zeiss Achrostatigmat 10×, N.A. 0.25, infinity corrected). The diverging beam that propagates from the focal plane of the objective is subsequently focused onto the sample by the aspherical lens. The lens is placed approximately at a distance $f_{\text{objective}} + f_{\text{back}}$ away from the objective (where $f_{\text{objective}}$ and f_{back} are the focal length of the objective and the back focal length of the aspherical lens, respectively). Fine adjustment of the distance between the objective and the lens is achieved through a precision mechanical translation holder and through the voice coil actuator of the pickup. For optical trapping experiments, polystyrene or glass beads dispersed in a drop of water on a conventional microscope glass slide (thickness ca. 1 mm) were used. A very small amount of the surfactant Tween 20 was added to the suspension in order to prevent sticking of the beads to the surface of the slide.

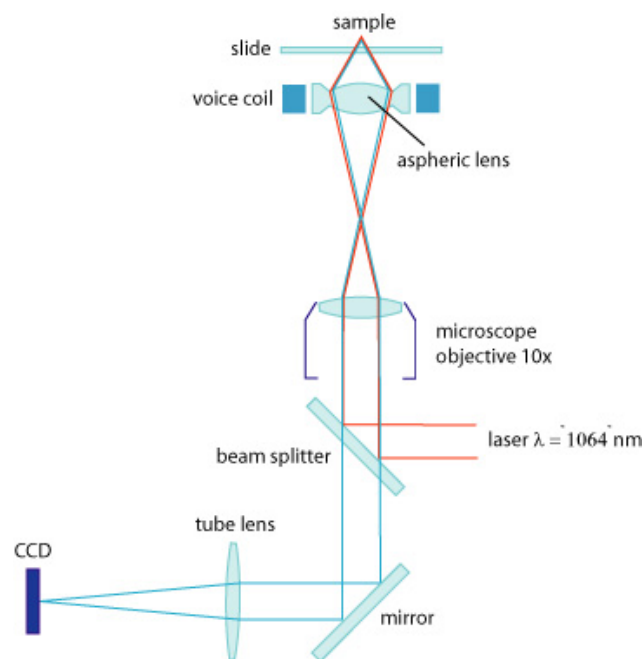


FIGURE 4.3 Preliminary set-up of aspherical-lens based optical tweezers.

A close view of the aspherical lens integrated in the set-up is shown in Fig. 4.4.

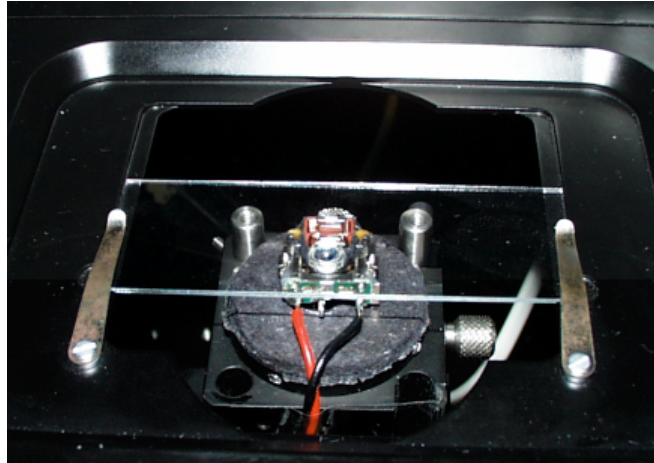


FIGURE 4.4 Close view of the aspherical lens and of the microscope slide.

Imaging of the sample is accomplished by using the same optics employed for focusing. The intermediate image produced by the aspherical lens is further magnified by the 10 \times objective. The light emerging from the objective, focused to infinity, is then re-focused by the tube lens ($f = 160$ mm), which forms the image onto the CCD chips (Fig. 4.3). Fig. 4.5 shows polystyrene beads with a diameter of 10 μm imaged with the set-up.

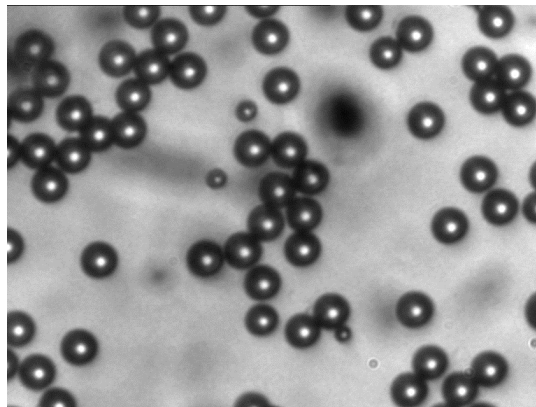


FIGURE 4.5 10 μm -beads imaged with the aspherical lens.

*spherical
aberration in the
system*

The focusing and imaging performance of the aspherical lens are predominantly degraded by spherical aberrations [Nutter 1997] that originate from the propagation of a non-collimated optical wavefront (the focused field) through the substrate (in this case the 1 mm-thick glass microscope slide). Due to spherical aberrations, rays travelling through the

aperture of the lens at different radii are focused at different points along the optical axis, resulting in a broadening of the focal spot. The effects of aberrations on the focusing performance of the aspherical lens can be evaluated by analyzing the *point spread function* (PSF) of the system. Since a direct experimental measurement was not possible, the PSF of the system consisting of the aspherical lens and the glass slide was calculated with the optical design software OSLO LT™, inserting the parameters from Table 4.1 and Table 4.2. The result of the raytracing is shown in Fig. 4.6.

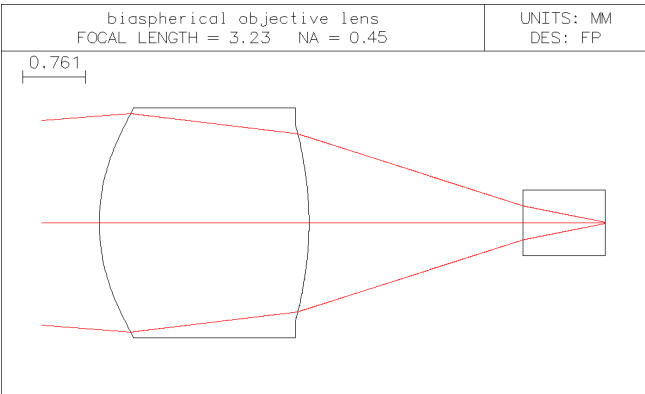


FIGURE 4.6 Ray propagation through the aspherical lens and the microscope slide.

In Fig. 4.7 the PSF of the aspherical lens focusing through a BK7 glass substrate ($n = 1.511$) is compared with the PSF of the same lens focusing through a polycarbonate substrate ($n = 1.551$).

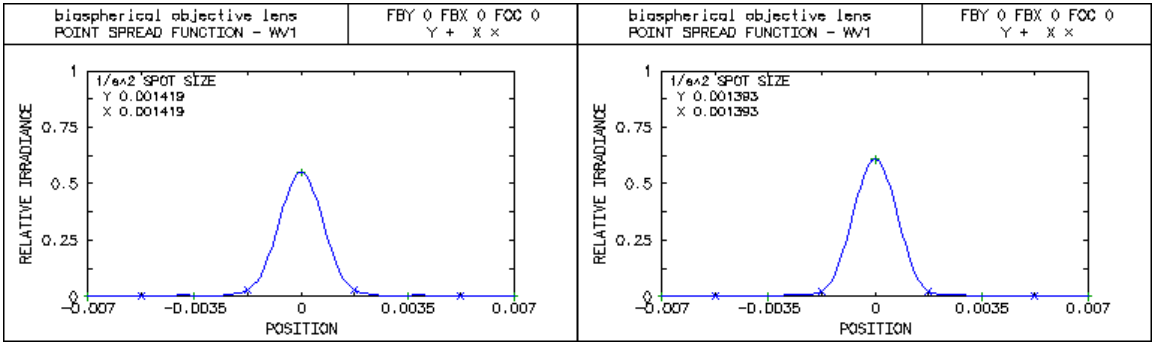


FIGURE 4.7 Comparison between the point spread function of the aspherical lens when focusing through a BK7 glass substrate (left) and when focusing through a polycarbonate substrate (right).

The PSF calculation confirms that substantially the focusing performance of the aspherical lens is not degraded when replacing the usual polycarbonate substrate (for which the lens is designed) with a glass microscope slide (glass BK7, refractive index 1.511, thickness 1 mm).

With the set-up described in this paragraph, stable optical trapping of polystyrene 10 μm -beads was already achieved at an optical power of 20 mW. The frames in Fig. 4.8 illustrate the translation of a trapped bead with the tweezers. The light scattered by the bead is also visible in the picture.

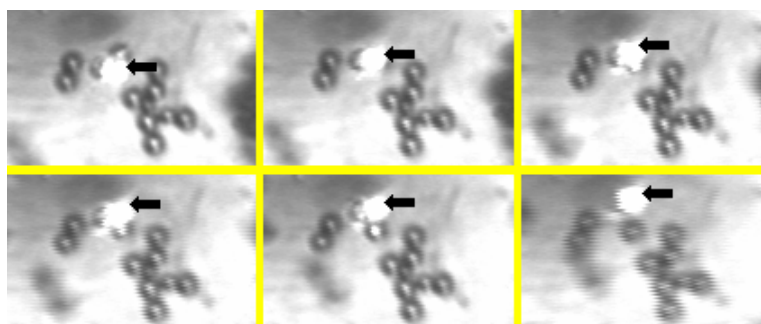


FIGURE 4.8 Translation of a polystyrene 10 μm -bead trapped with the aspherical lens-laser tweezers.

After these promising preliminary trapping experiments, a prototype of a compact optical tweezers was developed, as described in the next paragraph.

4.2.2 Compact optical tweezers prototype

The prototype of compact optical tweezers developed in this work includes a laser source, focusing and imaging optics, all within a single miniaturized unit. A semiconductor laser was chosen for integration into the prototype, because of its reduced size, the available high power, and its low price. Since conventional CD aspherical lenses are optimized for a wavelength of 780 nm, the diode laser DL7140-201 from Sanyo was chosen. The characteristics of this diode laser are given in Table 4.3.

Laser diode parameters (**Sanyo DL7140-201**)

Lasing wavelength	785 nm
Max optical output power	80 mW
Beam divergence (FWHM) θ_{\parallel}	7.0°
Beam divergence (FWHM) θ_{\perp}	17°

TABLE 4.3 Characteristics of the semiconductor laser Sanyo DL7140-201

The laser, together with a dichroic mirror and the aspherical lens, are assembled within a compact metallic housing. This module constitutes the trapping unit. The trapping unit, was assembled similarly to the original CD pickup in order to achieve maximum efficiency. The trapping unit is connected to the imaging unit which contains the relay optics necessary for imaging the sample onto the surface of a CCD. As relay optics, a 10× microscope objective was employed as described in Par. 4.2.1. The whole system is shown schematically in Fig. 4.9.

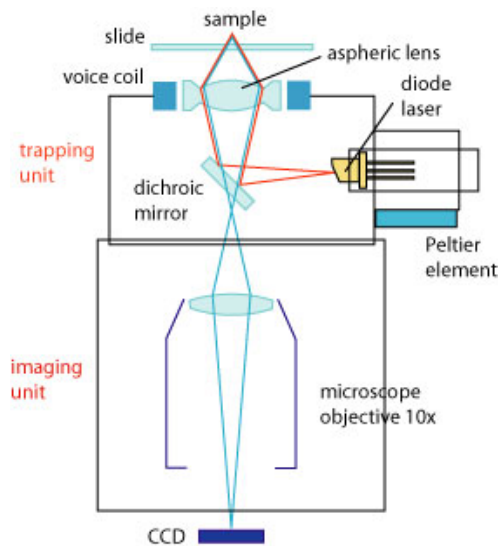


FIGURE 4.9 Set-up of compact optical tweezers.

The temperature of the laser diode is maintained by a Peltier element.

External electronics (Thorlabs LD1255) control the output power (up to 80 mW). The dichroic mirror, reflective at a wavelength of 780 nm, was taken from the same CD pickup as the aspherical lens.

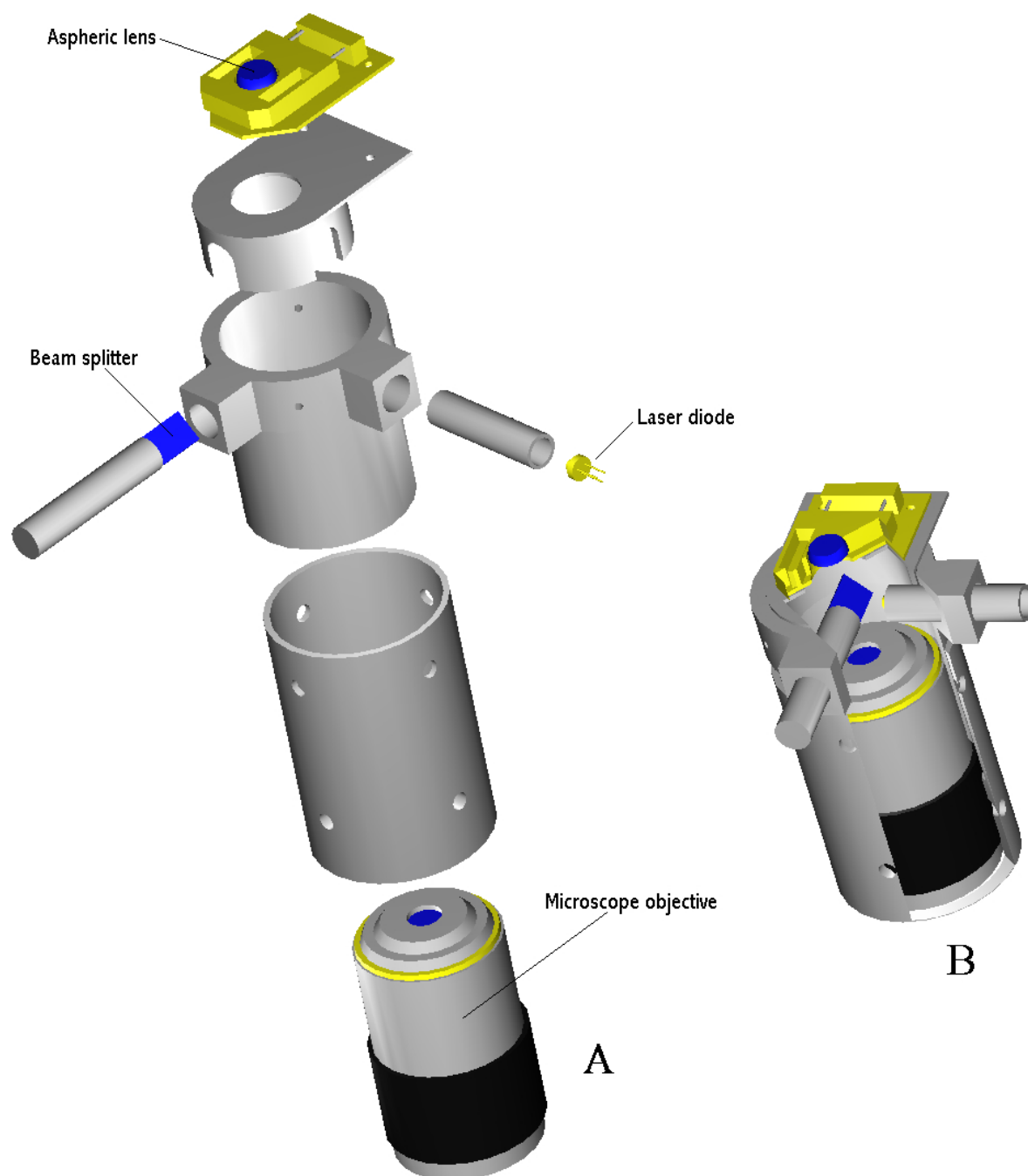


FIGURE 4.10 CAD rendering of the compact optical tweezers. (A) exploded view, (B) comprehensive view.

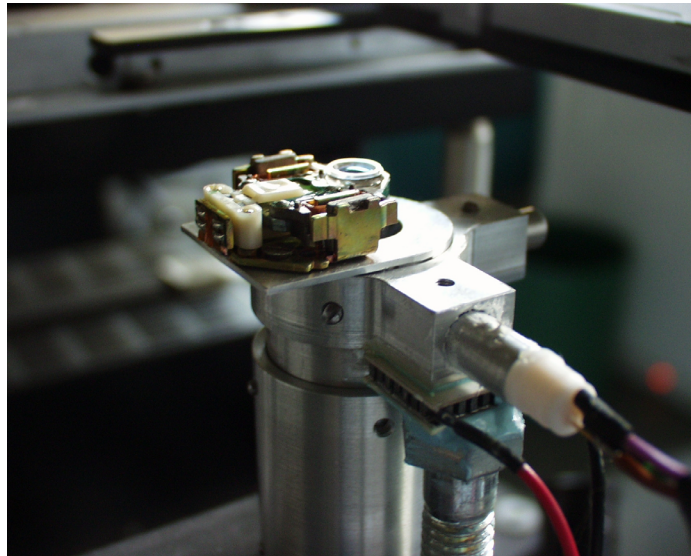


FIGURE 4.11 Compact optical tweezers (side view).

As illustrated by Fig. 4.10 and Fig. 4.11, the size of the whole assembly comes close to that of a conventional microscope objective. With this prototype, optical trapping of polystyrene beads in a suspension contained in a conventional plastic Petri dish was successfully achieved, as demonstrated in Fig. 4.12.

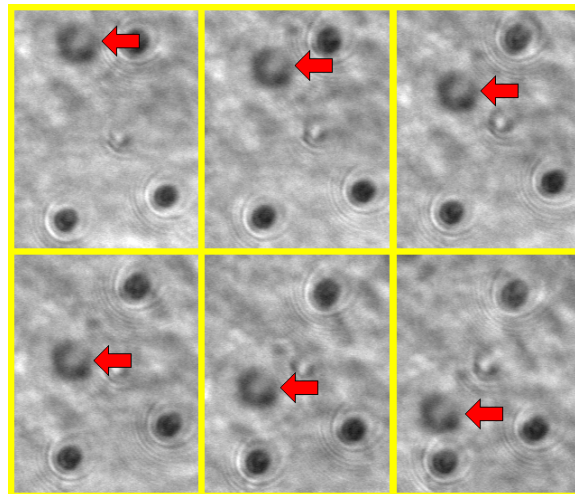


FIGURE 4.12 Trapping of a polystyrene bead inside a Petri dish.

The trapped particles can be translated within a plane by moving the mechanical xy-stage. Translation along the optical axis is accomplished by displacing the trap's focus with the voice-coil actuator.

4.3 *Discussion*

In this chapter, the design and development of a new compact optical trapping system based on a single aspherical lens was described. One of the aims of this work was to overcome the limitations of conventional optical tweezers, providing a versatile tool for optical manipulation of single particles and living cells. The prototype presented here allows easy and reliable micromanipulation of such specimens and hopefully constitutes a further step toward an instrument “as compact and easy to operate as, for example, a fluorescence illumination system” [Weber 1992]. The use of a plastic-molded aspherical lens from the CD technology has several advantages over conventional microscope objectives. An obvious advantage is the extremely low price of such mass-produced elements. A second advantage is that the construction of a very compact focusing unit is possible. Third, such lenses have a very long working-distance and are specifically designed for focusing a beam to a diffraction-limited spot even after traversing a thick and birefringent plastic substrate. As demonstrated in this work, the aspherical lens allows optical trapping through 1 mm-thick glass microscope slides and inside conventional plastic Petri dishes. Such features will greatly expand the field of application of optical tweezers, particularly in biotechnology. Indeed, optical tweezers are the technique of choice for disposing living cells in defined patterns on microstructured bio-compatible surfaces (which is essential for the development of cell-based biosensors). However, the constraints imposed by conventional optical tweezers are often incompatible with fast production and automation procedures as required by large scale applications. The introduction of a versatile and compact optical tweezers could help to bypass such problems simplifying the production of biochips. The field of microfluidic devices can also benefit from compact optical tweezers. The goal of the so-called *lab-on-a-chip* technology is the miniaturization of complex chemical equipment down to the scale of postage-stamp-sized microchips. A network of etched micrometer-sized channels and reaction chambers in association with miniaturised sensors and actuators provide the hardware necessary to

perform the basic operations in chemistry: mixing, diluting, heating, separating. The key point for the success of such devices is the capability to process tiny volumes of liquids, down to nanoliters, moving them along micro-channels, positioning them in different chambers, and controlling the temperature of different reaction chambers independently. The accomplishment of these goals requires the development of reliable micro-pumping mechanisms. The gradient force exerted by optical tweezers can reliably induce rotation of micro-machined objects, which are particularly suited to be used in micro-pumps [Galajda 2001; Gauthier 1997; Gauthier 1999a; Gauthier 1999b; Higurashi 1994; Higurashi 1998; Luo 2000; Ukita 1997]. The rotor speed can be easily adjusted by varying the laser power. Adopting miniaturized optical tweezers, many micro-pumps could be independently activated within a single micro-fluidic device. Additionally, miniature rotating devices may find application for measuring the properties of microscopic systems, for example to determine the torsional elasticity of biological polymers or measure local viscosity in micro-channels. For all these purposes, the availability of a compact, flexible and cheap optical trapping system will be of decisive importance.

A patent application on the compact optical tweezers prototype described here has been submitted to the German Patent Office [Pampaloni 2001] and is currently under examination.

References

- [Ashkin 1970a] Ashkin A.
Acceleration and trapping of particles by radiation pressure.
Phys. Rev. Lett 24:156-159 (1970)
- [Bouwhuis 1985] Bouwhuis G., Braat J., Huijser A., Pasman J., van Rosmalen G., Schouhamer K.
Principles of optical disc systems.
Immink Editions (Hilger, Boston 1985)
- [Collins 1999] Collins S.D., Baskin R.J., Howitt D.G.
Microinstrument gradient-force optical trap.
Appl. Opt. 38: 6068-6074 (1999)
- [Constable 1993] Constable A., Kim J., Mervis J., Zarinetchi F., Prentiss M.
Demonstration of a fiber-optical light-force trap.
Opt. Lett. 18: 1867-1869 (1993)
- [Galajda 2001] Galajda P., P. Ormos
Complex micromachines produced and driven by light.
Appl. Phys. Lett. 78: 249-251 (2001)
- [Gauthier 1997] Gauthier R.C.
Theoretical investigation of the optical trapping force and torque on cylindrical micro-objects.
J. Opt. Soc. Am. B 14: 3323-3333 (1997)
- [Gauthier 1999a] Gauthier R. C., Ashman M., Frangioudakis A., Mende H., Ma S.
Radiation-pressure-based cylindrically shaped microactuator capable of smooth, continuous reversible and stepped rotation.
Appl. Opt. 38: 4850-4860 (1999)
- [Gauthier 1999b] Gauthier R.C., Ashman M., Grover C.P.
Experimental confirmation of the optical-trapping properties of cylindrical objects.
Appl. Opt. 38: 4861-4869 (1999)
- [Goldwasser2001] Goldwasser S. M.
Notes on the Troubleshooting and Repair of Compact Disc Players and CDROM Drives.
Web document: http://www.repairfaq.org/REPAIR/F_cdfaq.html
- [Higurashi 1994] Higurashi E., Ukita H., Tanaka H., Ohguchi O.
Optically induced rotation of anisotropic micro-objects fabricated by surface micromachining.
Appl. Phys. Lett. 64: 2209-2210 (1994)
- [Higurashi 1998] Higurashi E., Sawada R., Ito T.
Optically induced rotation of a trapped micro-object about an axis perpendicular to the laser beam axis.
Appl. Phys. Lett. 72: 2951-2953 (1998)
- [Hung 2000] Hung K. M.
Effects of an asymmetrically molded plastic objective lens on the push-pull tracking error signal in an optical disk drive.
Appl. Opt. 39: 1309-1314 (2000)
- [Kawai 1997] Kawai H., Suzuki M., Yoshida A.
Birefringence-free acrylic resin for precision plastic optics.
Proc. SPIE 3135: 42-51 (1997)

- [Luo 2000] Luo Z.-P., Yu-Long S., Kai-Nan A.
An optical spin micromotor.
Appl. Phys. Lett. 76: 1779-1781 (2000)
- [Lyons 1995] Lyons E.R., Sonek G.J.
Confinement and bistability in a tapered hemispherically lensed optical fiber trap.
Appl. Phys. Lett. 66: 1584-1586 (1995)
- [Nutter 1997] Nutter P.W.
Image formation in the scanning optical microscope.
PhD Thesis, The Manchester School of Engineering - Division of Electrical Engineering (1997)
- [Pampaloni 2001] Pampaloni F., Böhmer M.
Compact optical tweezers.
Aktenzeichen des Deutschen Patentamts 1D1 43 637.8
- [Taguchi 1997] Taguchi K., Ueno H., Hiramatsu T., Ikeda M.
Optical trapping of dielectric particle and biological cell using optical fibre.
Electr. Lett. 33: 413-414 (1997)
- [Taguchi 2000] Taguchi K., Atsuta K., Nakata T., Ikeda M.
Levitation of a microscopic object using plural optical fibers.
Opt. Comm. 176: 43-47 (2000)
- [Taguchi 2001] Taguchi K., Atsuta K., Nakata T., Ikeda M.
Single laser beam fiber optic trap.
Opt. Quant. Electr. 33: 99-106 (2001)
- [Tiribilli 1999] Tiribilli B., Bartoli A., Quercioli F.
Surface inspection using a compact disc reading head.
Proceedings of ODIMAP II (Pavia, May 20-22, 1999)
- [Ukita 1997] Ukita H., Nagatomi K.
Theoretical demonstration of a newly designed micro-rotator driven by optical pressure on a light incident surface.
Opt. Rev. 4: 447-449 (1997)
- [Weber 1992] Weber et al.
Int. Rev. Cytol. 133 : 1-41 (1992)

Hollow beam optical tweezers by using an Axicon

5.1 Hollow beam laser traps

5.1.1 Limitations of Gaussian-beam optical traps

The gradient force experienced by a dielectric particle in a Gaussian-beam optical trap (which uses a laser with TEM₀₀ propagation mode) is proportional to the difference between the refractive index of the particle and that of the surrounding medium (see also Chapter I):

$$\langle F_{grad}(\vec{r}, t) \rangle \approx \frac{1}{2} (n_p^2 - n_m^2) \nabla \langle \vec{E}^2(\vec{r}, t) \rangle \quad (5.1)$$

where $\langle F_{grad}(\vec{r}, t) \rangle$ is the time-averaged gradient force, \vec{E} the electric field of the laser beam, n_p and n_m are, respectively, the refractive index of the particle and the refractive index of the medium.

If $n_p > n_m$, as for a polymer particle in water ($n_p = 1.49$ – 1.59 , $n_m = 1.33$), the gradient force points toward the region of maximum electric field intensity (i.e. the laser focus), where the particle is stably trapped in three dimensions.

On the contrary, if $n_p < n_m$, the gradient force drives the particle away from the focus. Consequently, „low-refractive index“ particles such as micrometer-sized water droplets in a water-in-oil micro-emulsion ($n_p = 1.33$, $n_m = 1.46$ for liquid paraffin), cannot be trapped by a focused Gaussian beam. Optical trapping of liquid droplets can be of particular interest when studying molecular processes in spatially confined liquid environments (such as biomolecular reactions inside organelles or cells), because processes there can behave quite differently than when taking place in a bulk environment,

due basically (but not exclusively) to the much higher surface-to-volume ratio. Single micro-droplets containing different solutes can be fused by using optical manipulation and the physical or chemical processes occurring inside the resulting mixture can then be monitored with spectroscopic methods. Raman spectroscopy on optically trapped organic micro-droplets in water (like toluene droplets in water) was already reported in the literature [Ajito 1998; Ajito 1999; Ajito 2001]. Similar studies on water-in-oil micro-emulsions, which appear ubiquitously in petroleum processing, food and pharmaceutical preparation, are also of interest, but „low-index“ particles cannot be manipulated with TEM₀₀ optical tweezers. Another type of particles which cannot be trapped by Gaussian beams are micrometer-sized (Mie-size range) metallic particles, because the scattering force largely overcomes the gradient force in this case. On the contrary, nanometer-sized (Rayleigh-size range) metallic particles can efficiently be trapped, because scattering from metallic and dielectric particles is similar in this size range [Ng 2000; Sato 1994; Svoboda 1994].

Optical confinement and trapping of both „low-index“ and metallic micrometer-sized particles can be achieved by using alternative trap designs. The general strategy is to generate an annular beam, which has a low-light intensity core (“dark” core) surrounded by a high-intensity ring-shaped region. After focusing the beam with a high-N.A. objective, a particle placed in the dark centre of the beam experiences a repulsive potential barrier created by the surrounding high-intensity boundaries, and therefore can be two-dimensionally trapped in the centre. In this way, optical trapping of highly reflective and low-refractive particles can be performed. A straightforward way to obtain an annular beam is to partially obstruct the laser beam. With such a method, trapping of metallic Mie-size particles was successfully demonstrated [Gu 2000]. However, more flexible and efficient methods are available, which will be described in the next paragraphs.

5.1.2 Scanning-beam optical trap

As ingeniously demonstrated by Sasaki et. al. [Sasaki 1991, Sasaki 1992], both low-index and metallic particles can be steadily trapped in three-dimensions by quickly moving a TEM₀₀ beam around a circle (Fig. 5.1). A particle with $n_p < n_m$ or with high reflectivity is „caged“ by the scanning laser beam if its scan rate is faster than the time scale of the Brownian diffusive

motion of the particle. In this way, Sasaki et al. succeeded in trapping iron particles in water and water droplets in liquid paraffin. However, since the rotating beam apparatus (based generally on galvanic scanning mirrors, or acousto-optic modulators) is relatively complicated to build and to control, alternative schemes for implementing “dark core” laser traps were proposed.

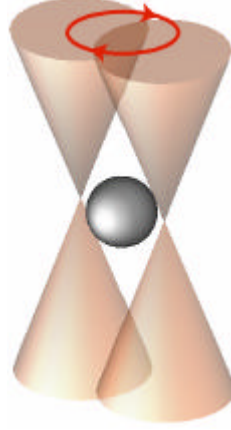


FIGURE 5.1 **Scanning- beam optical trap.**

5.1.3 **Optical trapping with doughnut-mode beams**

An ideal laser emits a coherent and monochromatic electromagnetic field $\vec{U}(r)$ which satisfies the Helmholtz wave equation:

$$(\nabla^2 + k^2)\vec{U}(r) = 0 \quad (5.2)$$

where $k = 2\pi/\lambda$ (wave number) and λ is the laser’s wavelength. Eq. (5.2) has an infinite manifold of solutions. Actual lasers generate a spatially coherent electromagnetic field which has a finite transversal extension and propagates with moderate spreading. That means that the wave amplitude changes only slowly along the propagation axis (z-axis) compared to the wavelength and finite width of the beam. Thus, the electromagnetic wave equation Eq. (5.2) can be solved using the *paraxial approximation*. By solving the wave equation in Cartesian coordinates, a complete and orthogonal set of solutions is given by the products of Hermite’s polynomials and a Gaussian function. The so-called *Hermite-Gaussian*

propagation modes are structurally stable, i.e. their transverse intensity profile does not change qualitatively under free propagation [Abramochkin 1993]. Each Hermite-Gaussian mode is characterized by two integer numbers m and n , and denoted as TEM_{mn} or HG_{mn} . Let x and y be the transverse, and ζ the longitudinal (along the propagation axis) directions. Then, the electric field amplitude is given by

$$TEM_{m,n}^H = \frac{1}{w(\zeta)} H_m\left(\sqrt{2} \frac{x}{w}\right) H_n\left(\sqrt{2} \frac{y}{w}\right) \exp\left[ikz - \frac{r^2}{w_0^2(1+i\zeta)} - \Psi_{m,n}\right] \quad (5.3)$$

$\zeta = z/z_R$ is the normalized coordinate along the propagation axis, with $z_R = kw_0^2/2 = \pi w_0^2/\lambda$ being the Rayleigh length and w_0 the radius of the beam waist and

$$E_0 = \frac{1}{w(\zeta)} \exp\left[ikz - \frac{r^2}{w_0^2(1+i\zeta)} - \Psi_{m,n}\right] \quad (5.4)$$

is the electric field of a Gaussian beam, where

$$\Psi_{m,n} = (1+m+n)\arctan \zeta \quad (6.5)$$

denotes Gouy's phase, which is a phase-shift acquired by the phase front when passing through the beam's focus. Guoy's phase depends on the mode order (m,n) .

The $H_p(x)$ are Hermite polynomials of order p in x . Hermite polynomials are defined through Rodrigues' formula

$$H_p(x) = (-1)^p \exp(x^2) \frac{d^p}{dx^p} \exp(-x^2), \quad (6.6)$$

so that

$$H_0(x) = 1; \quad H_1(x) = 2x; \quad H_{j+1}(x) = 2xH_j - 2jH_{j-1}.$$

The fundamental mode TEM_{00} (or HG_{00}) has the well-known Gaussian intensity profile (Fig. 5.2). Hermite-Gaussian beams can be directly generated in a laser cavity.

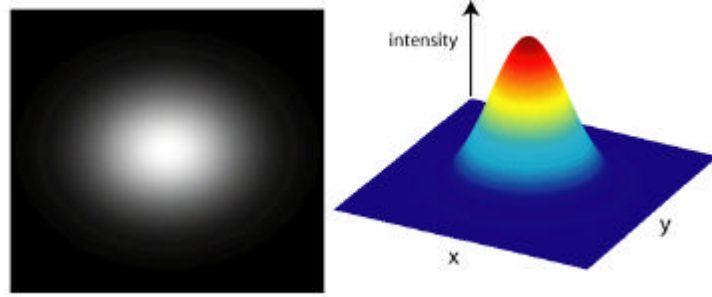


FIGURE 5.2 Transverse intensity profile of a TEM_{00} mode laser beam.

Higher order TEM_{mn} modes are shown in Fig. 5.3.

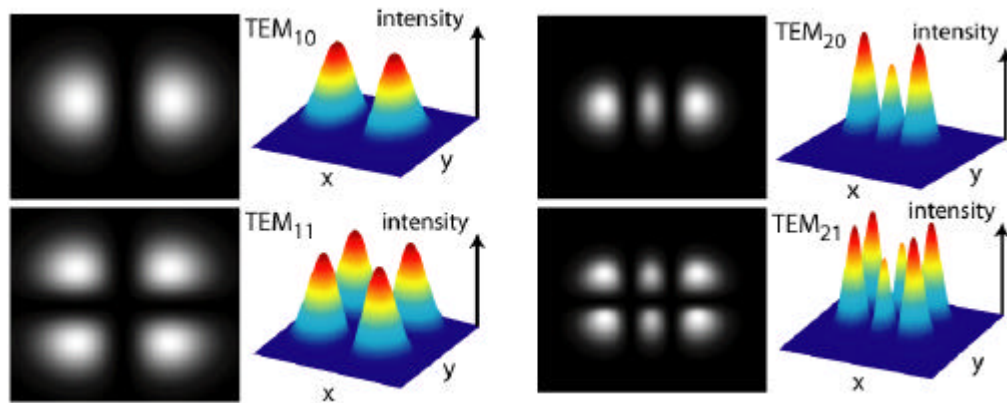


FIGURE 5.3 Transverse intensity profile of higher order TEM_{lp} mode laser beams.

Laguerre-Gaussian propagation modes

Hermite-Gaussian beams of higher order have been used to firmly trap disk-shaped blood cells, stabilizing their three-dimensional alignment within the trap [Sato1991], but such beams are not generally employed in laser trapping systems. Another complete basis set of solutions is given by solving the paraxial wave equation in cylindrical coordinates. In this case, the transverse electric field distribution is described by the product of a Laguerre polynomial and a Gauss function. Laser beams described by *Laguerre-*

Gaussian propagation modes have a radially symmetric field distribution. The transverse electric field is given by

$$TEM_{m,n}^* = \frac{e^{-in\phi}}{w(\zeta)} \left(\frac{r}{w(\zeta)} \right)^n L_m^n \left(\frac{2r^2}{w^2(\zeta)} \right) \exp \left[ikz - \frac{r^2}{w_0^2(1+i\zeta)} - \psi_{n,m}^L \right] \quad (5.7)$$

where $\psi_{n,m}^L = (1+n+2m)\arctan \zeta$ is again Gouy's phase, and the $L_m^n(r)$ are associated Laguerre polynomials defined by Rodrigues' formula:

$$L_m^n(r) = \frac{e^r r^{-n}}{m!} \frac{d^m}{dr^m} (e^{-r} r^{n+m}) \quad (5.8)$$

so that

$$L_0^1 = 1; \quad L_1^1 = 2 - x; \quad L_2^1 = 3 - x$$

In Eq. (5.7), $n \geq 0$ is the azimuthal mode index and $m \geq 0$ is the radial index. The index n is the number of complete phase cycles around the beam circumference (the phase changes from 0 to $2\pi n$); the number of radial nodes of the beam is given by $m + 1$. The azimuthal phase term $e^{-in\phi}$ distinguishes Laguerre-Gaussian modes from Hermite-Gaussian modes. Unlike Hermite-Gaussian modes, which have largely planar wavefronts, Laguerre-Gaussian modes have helical wavefronts arising from the azimuthal phase structure (Fig. 5.4).



FIGURE 5.4 The helical wavefronts of the optical vortices with $n = 1$, $n = 2$, and $n = 3$

Since the azimuthal phase of the helical wavefront varies from 0 to $2\pi n$, a phase singularity occurs along the beam axis [Mair 2000]. Thus, a Laguerre-

*orbital angular
momentum of a
LG beam*

*spin angular
momentum of a
LG beam*

Gaussian beam has zero field intensity along its center axis. Moreover, because of the helical wavefront, a *rotating Poynting vector* is associated with the propagation of Laguerre-Gaussian beams (Padgett1995). Consequently, Laguerre-Gaussian beams carry an intrinsic *orbital angular momentum* (independent on the polarization of the beam) of $n\hbar$ per photon [Allen 1992], which can be transferred onto absorbing particles inducing a rotational motion [He 1995; Padgett 1999; Mair 2000; O’Neil 2000]. For this reason, Laguerre-Gaussian beams are also called “optical vortex” beams. Light beams carry also a *spin angular momentum* that is associated with circular polarization. Circularly polarized light carries a spin angular momentum of $+\hbar/-\hbar$ per photon. Transfer of spin angular momentum from circular-polarized light to a birefringent quartz wave plate was already reported by Beth in the 1930s [Beth 1936]. Beth’s experiment was recently reproduced on birefringent calcite particles trapped with optical tweezers using a circularly polarized laser beam [Moothoo 2001]. The total angular momentum (J_z) of a beam is given both by its spin (S_z) and orbital (L_z) contributions:

$$J_z \hbar = (L_z + S_z) \hbar \quad (5.9)$$

Fig. 5.5 shows the transverse intensity profiles of higher-order TEM_{mn}^* (or LG_{mn}) laser beams. The fundamental modes TEM_{00}^* (LG_{00}) and TEM_{00} (HG_{00}) are identical and have a Gaussian intensity profile usually observed for conventional lasers (Fig. 5.2).

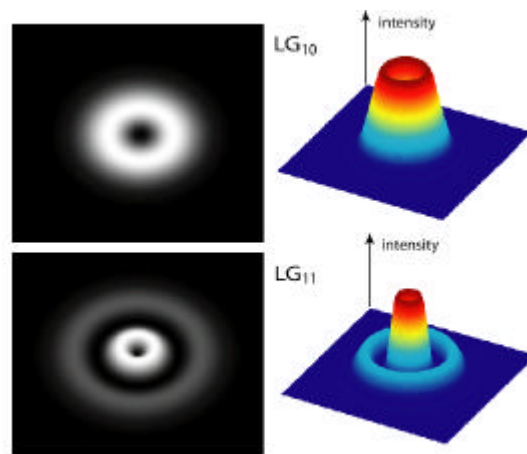


FIGURE 5.5 Transverse intensity profile of higher order TEM_{lp}^* mode laser beams.

Both the Hermite-Gaussian and the Laguerre-Gaussian modes constitute a complete, orthogonal set of solutions (eigenmodes) of the wave equation in the paraxial approximation. Consequently, the linear combination of two eigenmodes produces again an eigenmode [Mair 2000]. Hermite-Gaussian and Laguerre-Gaussian modes are structurally stable, that is the amplitude and phase profiles remain unchanged in shape at any position z along the propagation axis, though the transversal scale, given by $w(z)$, changes as the beam propagates. A structurally stable beam is also called “non-diffracting” [Bouchal 2000]. The mode structure of a non-diffracting beam is preserved even when the beam is focused.

Laguerre-Gaussian modes with $n > 0$ and $m = 0$ have only one zero at the propagation axis ($r = 0$) and are also called *doughnut modes*.

In Fig. 5.6, the intensity profile of a focused doughnut beam is shown.

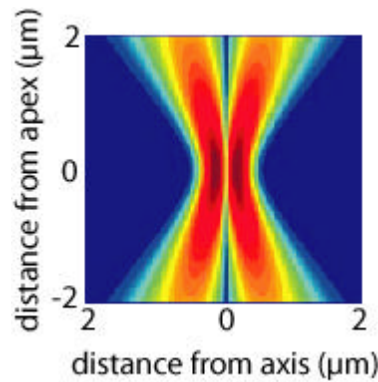


FIGURE 5.6 **Transverse intensity profile of a focused LG_{01} doughnut beam (adopted from Webster 2000).**

**optical trapping
with doughnut
beams**

Doughnut beams are successfully used in optical trapping. Mie-sized metallic particles, as well as low- and high-refractive-index particles can be trapped by using doughnut modes. Indeed, a primary advantage of doughnut-mode optical tweezers over conventional TEM_{00} -laser traps is that all types of particles can be manipulated with one and the same beam [Gahagan 1996, Gahagan 1998]. Regarding the trapping efficiency of doughnut-beams, the inventor of optical trapping, Arthur Ashkin, already pointed out that only light rays with large inclination towards the beam’s main propagation axis contribute to the axial trapping efficiency [Ashkin 1992], since the gradient force arises from a change in the direction of the light rays when interacting with the trapped particle (at least within the framework of geometric optics). Thus, a TEM_{01}^* beam, which has no on-axis rays, has an improved efficiency

parameter Q_{axial} (about efficiency parameter Q see also Chapter I) for high-index particles. Sato et al. reported an improvement of about 20% even for the lateral trapping efficiency when using a TEM_{01}^* beam [Sato 1991]. However, further investigations did not confirm such early observations. In fact, the lateral trapping efficiency is largely unaltered when using Laguerre-Gaussian beams. In case of dielectric, high-index particles with a diameter of less than 2 μm , the lateral trapping force of TEM_{mn}^* beams is indeed lower than that exerted by a TEM_{00} mode [O'Neil 2001].

trapping of low-index and metallic particles

Laguerre-Gaussian beams are primarily useful in optical manipulation of metallic and low-index particles. Stable trapping of low-index particles (e.g. hollow glass microspheres in water) in three dimensions by using a TEM_{01}^* beam has been demonstrated [Gahagan 1996, Gahagan 1998]: the spheres (diameter 20 μm) are trapped slightly above the beam focus; transversal trapping is due to scattering and gradient forces (both directed towards the dark core), whereas longitudinal trapping results from the balance between scattering and gravitational forces.

Two-dimensional trapping and translation of Mie-sized metallic particles was obtained with TEM_{01}^* [O'Neil 2000] and TEM_{03}^* [Friese 1996] Laguerre-Gaussian beams. The micron-sized metallic particles are loosely confined inside the “dark” region of the annular beam by scattering force, below the beam focus.

transfer of orbital angular momentum: optical spanners

As previously cited, doughnut beams can also transfer an angular momentum, due to their wavefront helicity. For this reason, a laser trap created with a doughnut beam is also called an “optical spanner” or “optical wrench”. Transfer of orbital angular momentum from a doughnut beam induces a torque in the absorbing particles (for example CuO or Teflon particles), which subsequently rotate around the optical axis. For absorbing particles, the torque force depends also on the beam polarization: the particle rotates faster if the beam is circularly polarized with a spin of the same direction of rotation as the vortex, and slower if the spin is oppositely oriented [Friese 1996].

In the case of metallic particles with much higher reflectivity, the polarization state of the beam has no influence on the rotation of the particle and the predominant force is the scattering force. Therefore, rotation is induced only by the orbital component of the Poynting vector [O'Neil 2000]. In contrast, for non-absorbing birefringent particles such as calcite particles, rotation is induced predominantly by the polarization state of the beam [Friese 1998a, Friese 1998b, Friese 2001].

A general scheme for rotating trapped particles applicable with arbitrary dielectric properties (neither absorption nor birefringence are required) was recently proposed by Paterson et al. [Paterson 2001].

*generation of
Laguerre-
Gaussian modes*

It is possible to configure a laser cavity to directly produce Laguerre-Gaussian modes [Tamm 1990, Harris 1994]. However, Laguerre-Gaussian beams are much simpler obtained by externally converting Hermite-Gaussian modes.

*computer-
generated-
holograms*

One method for generating optical vortices uses *computer-generated-holograms* (CGH) [Churin 1999]. The interference pattern generated by a plane wave crossing a beam with helical phase structure n is numerically computed and then transferred onto a transparent photopolymer film [Gahagan 1998]. The hologram acts as a grating, and a fundamental TEM₀₀ beam transmitted through it diffracts into multiple orders which can be spatially separated with a pinhole. In the diffracted beam, the plane wavefront of the TEM₀₀ beam is converted into a helical wavefront. The first-order diffracted beam has the phase structure e^{inf} . The higher-order beams contain optical vortices with their orbital index n equal to the diffraction order [Gahagan 1998]. The use of computer-generated-holograms for the generation of Laguerre-Gaussian modes is more flexible than other methods. A remarkable advantage of the holographic method is that the size of the vortex at the beam's waist can be changed by simply varying the diameter of the Gaussian beam incident on the hologram. This is particularly important for optimizing optical trapping. However, holograms have also some limitations. The first limitation is that about 40% of the light incident onto the hologram is absorbed, scattered and reflected by the hologram. The second limitation is that the resulting beam (first diffraction order) is not a single LG mode, but rather a combination of many Laguerre-Gaussian modes with different indices n . Thus, the central field singularity (doughnut) can be clearly observed only in the far field of the beam [Mair 2000, Padgett 1999]. Nevertheless, computer-generated-holograms are widely used for optical trapping [He 1995, Friesse 1996, Padgett 1999, Arlt 2000, O'Neil 2000, O'Neil 2001]. Particularly interesting is a method which produces doughnut modes by reconstructing computer-generated holograms on a liquid-crystal display (LCD) [Reicherter 1999]. With such a technique, polystyrene particles were successfully trapped. Even more intriguing is the possibility of generating multiple, independently movable optical traps with LCD-modulation [Reicherter 1999, Liesener 2000]. Spatial-light modulators can also be used for that purpose [Davis 1999, Mogensen 2000].

A pure Laguerre-Gaussian mode can be produced with 100% efficiency by using a pair of identical cylindrical lenses. With a cylindrical-lens mode converter, any Hermite-Gaussian mode with indices n and m is converted in a Laguerre-Gaussian mode with indices $n' = (n-m)$ and $m' = \min(n,m)$ [Padgett 1995].

5.2 *Hollow beam optical trap by using an axicon*

5.2.1 Introduction

The *axicon* is an optical element having a conical surface. Such an element was introduced and characterized in the 1950s by McLeod [McLeod 1954]. Unlike spherical lenses, axicons refract light rays at a constant angle regardless of the rays' distance from the optical axis. Consequently, an axicon converts a Gaussian beam into a diverging, ring-shaped hollow beam, as shown in Fig. 5.7.

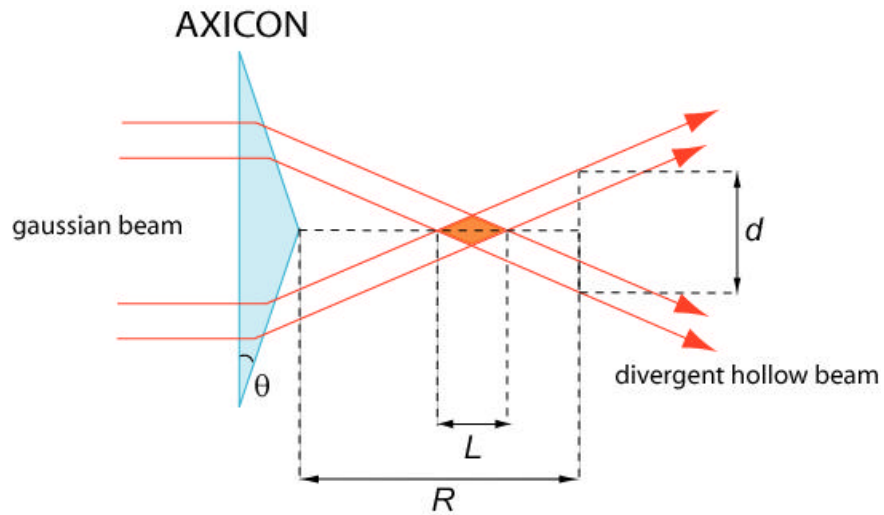


FIGURE 5.7 Refraction of a light beam by an axicon.

From Fig. 5.7 it is immediately seen that all rays of the transmitted beam are refracted toward the axis of the conical surface. Thus, the energy of the incoming light beam is concentrated near the optical axis along a line of

length L . This differs from the action of a spherical lens, which focuses, at first order, all the light rays into a single point. After passing the focal line, the beam of light propagates as a diverging ring of light. The ring diameter d at a distance R from the axicon's apex is given by [Schäfer 1986, Manek 1998, Song 1999a]:

$$d = 2R\theta(n_g - 1) \quad (5.10)$$

*difference
between axicon-
generated hollow
beams and LG
modes*

where θ is the axicon's base angle (typically $\theta = 10$ mrad) and n_g the refractive index of the axicon. In contrast to a TEM_{01}^* mode, the hollow beam generated by an axicon has a dark core extended over most of its diameter and steep walls where most of the light power is concentrated (Fig. 5.8).

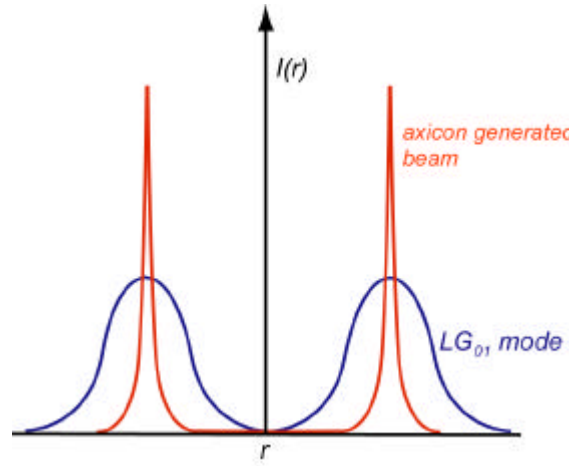


FIGURE 5.8 Comparison between the intensity profile of a hollow beam generated by an axicon and that of a TEM_{01}^* beam.

*applications of
axicon*

The non-spherical properties of an axicon and its ability to confine most of the beam energy inside a narrow ring have led to a variety of applications, such as laser machining [Belanguer 1978, Rioux 1978] and corneal surgery [Ren 1990]. Recent applications of the axicon are atom trapping [Manek 1998, Song1999a, Song1999b, Ovchinnikov 1998, Arlt 2001] and laser particle acceleration [Hafizi 1999].

*generation of
Bessel beams
with axicon*

Focusing a Gaussian beam through an axicon is the most efficient method for generating a non-diffracting *Bessel beam*. As discussed in Paragraph 5.1.3, most lasers have a transverse electric field distribution which can be

described by Hermite-Gaussian or Laguerre-Gaussian modes. In 1987, Durnin et al. [Durnin 1987] proposed the existence of light beams described by

$$E(r, z, t) = A \cdot J_0(k_\rho \rho) \exp[i(k_z z - \omega t)] \quad (5.10)$$

which is an exact solution of the Helmholtz Eq. (5.2). Here, A is a normalizing constant, $\rho = \sqrt{x^2 + y^2}$, k_ρ and k_z are, respectively, the radial and longitudinal components of the wave vector k , with $k^2 = k_\rho^2 + k_z^2 = \omega^2 / c^2$, and $J_0(k_\rho \rho)$ is the zero-order Bessel function of the first kind.

Eq. (5.10) describes the field of a so-called Bessel-beam. An ideal Bessel-beam has a sharp on-axis intensity peak, is absolutely free of any divergence, and has an infinite transversal extension (Fig. 5.9), which can not be realized experimentally.

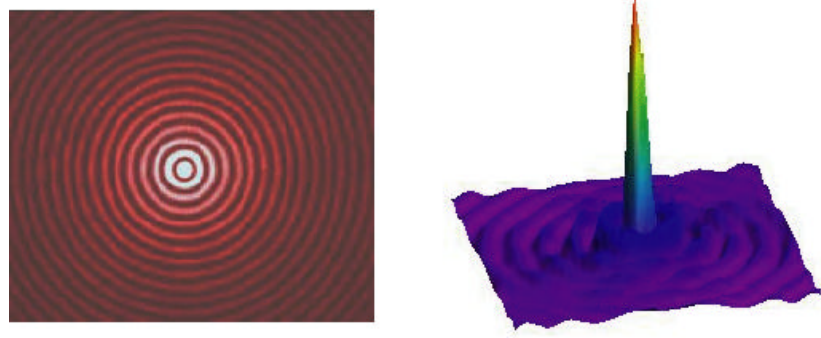


FIGURE 5.9 **Transverse intensity distribution of a Bessel beam.**

However, a close approximation to a Bessel beam is generated by an axicon near its focal line. The central intensity maximum of the beam propagates nearly without spreading (or, in other words, is non-diffracting) for a limited distance given by [Arlt 2001]:

$$L_{\max} \approx \frac{w_0}{(n_g - 1)\theta} \quad (5.11)$$

Where w_0 is the beam waist, n_g the refractive index of the axicon, and θ the base angle of the axicon. The narrow central spot of the Bessel beam, which

is available over a long axial distance, can be used for aligning and trapping of atoms [Arlt 2000, Arlt 2000b]. The axicon can also be applied for optical trapping. Very recently, a technique for optical manipulation of micrometer-sized particles (including biological samples) was reported that uses an axicon-generated zeroth-order Bessel beam [Arlt2001].

In the present work, a new method of trapping both micrometer-sized metallic particles as well as low-index droplets is presented. Such particles are firmly trapped with a hollow beam generated by an axicon. The optical trap that is generated by strongly focusing such a beam works similar to the “optical bottle” discussed by Arlt et al. [Arlt 2000]. An “optical bottle” is a beam with zero intensity near its focus surrounded by non-vanishing intensity along all three directions. A pure, non-diffracting Laguerre-Gaussian mode is a structurally stable beam, which propagates in space without changing its shape. Thus, the characteristic on-axis singularity is sustained even when the beam is focused (see Fig. 5.6). As a consequence, the zero-intensity region obtained at the focus is only two-dimensionally surrounded by regions of higher intensity. In contrast, an “optical bottle” can be obtained only when focusing a beam which is structurally unstable. Structurally unstable beams are obtained by superimposing two or more structurally stable beams, whose relative phases change with propagation [Arlt 2001]. The beam produced by an axicon is structurally unstable as well. The difference between an “optical bottle” and the hollow optical trap generated by an axicon is that the axicon does not produce a dark region enclosed in all directions by high-intensity boundaries but rather a light “cup”, as shown in Fig. 5.10. Micrometer-sized particles can be trapped both above and below the focal region of the optical bottle. The set-up adopted for producing the optical bottle trap and the experimental results are discussed in the next paragraphs.



FIGURE 5.10 “Light cup” optical trap produced with the axicon.

5.2.2 Set-up

The set-up developed for generating the “optical bottle”-trap is schematically shown in Fig. 5.11. The TEM₀₀ beam emitted by a solid state, diode pumped ND:YAG laser (LCS-DTL-222, Laser Compact, maximum output power 300 mW) is directed toward the axicon using two adjustable mirrors.

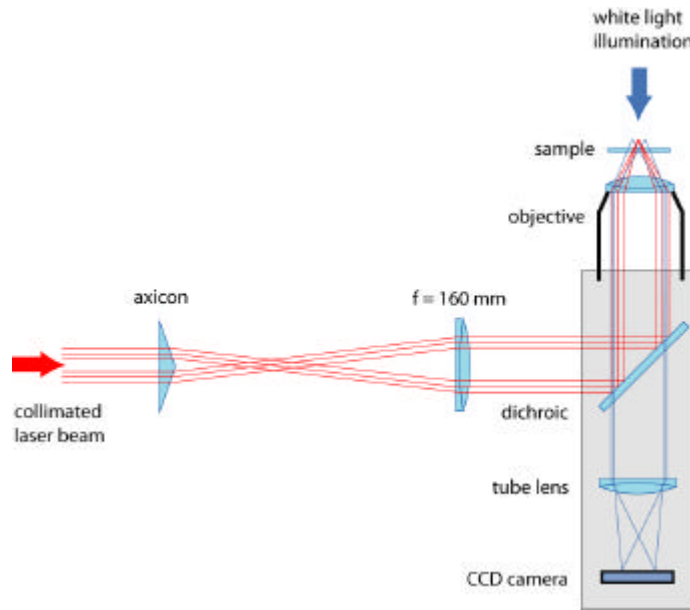


FIGURE 5.11 Set-up for “optical bottle”-tweezing.

The collimated beam is linearly polarized and has a wavelength of 1064 nm. The beam diameter immediately in front of the axicon is about 2 mm. The axicon converts the beam into a hollow light cone with an aperture angle 2θ , where $\theta = 10$ mrad is the axicon cone angle. An achromatic doublet lens with focal length $f = 160$ mm that is placed at a distance of about 180 mm away from the axicon’s apex yields a nearly collimated, slightly divergent cylindrical hollow beam with an outer diameter of about 3.5 mm. The beam, after reflection by a dichroic beam splitter, is introduced into the objective’s rear pupil and focused onto the sample. The objective (Zeiss Neofluar 100 \times , 1.3 N.A., oil immersion) strongly focuses the hollow beam, producing a micrometer-sized hollow conical shell with its vertex in the focal plane, as shown in Fig. 5.10.

Frame “A” in Fig. 5.12 shows the transversal intensity profile of the beam at about 10 micrometers below the focal plane. The ring-shaped profile of the

beam is almost circular, as can be seen in the picture. The ring's diameter is about 15 μm . An image at the focal plane is shown in frame "B" (Fig. 5.12). The focus has the characteristic intensity profile of a Bessel beam, i.e. a bright central spot surrounded by lower-intensity side lobes (see also Fig. 5.9 for comparison).

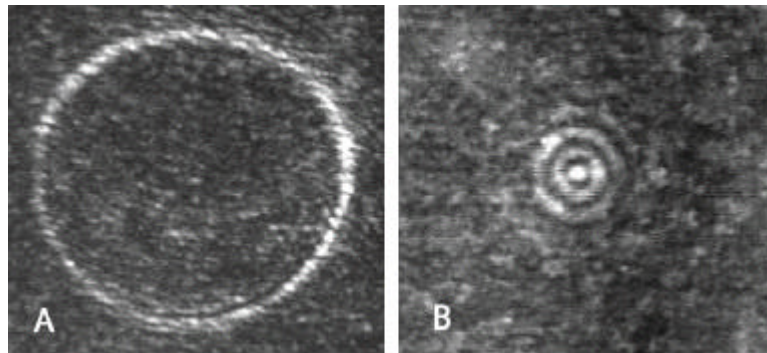


FIGURE 5.12 Transversal intensity profile of the "optical bottle" produced by the axicon. (A) 10 μm below the focus; (B) at the focus.

5.2.3 Measurements

trapping of micrometer-sized metallic particles

To experimentally test the ability of the axicon-generated "optical bottle" in trapping and manipulating micrometer-sized metallic particles, a small quantity of fine zinc powder (Merck) was suspended in 5 ml of distilled water. The suspension was then transferred to the microscope probe chamber, and the particles (in the size range between 5 and 50 μm) were imaged with the inverted microscope set-up using bright field illumination (Fig. 5.13).

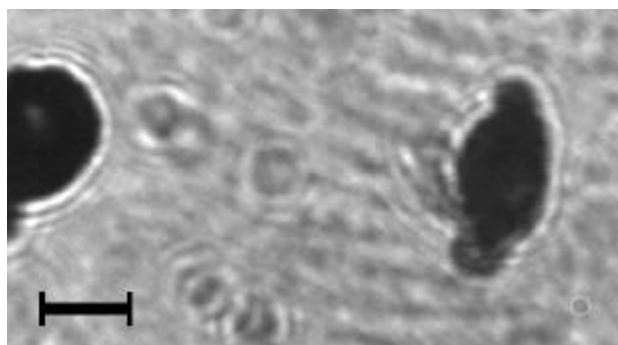


FIGURE 5.13 Bright-field image of a micrometer-sized zinc particle (scale bar 10 μm).

Two-dimensional optical trapping of the particles was achieved by slightly displacing the laser focus upwards along the optical axis (as shown in Fig. 5.12a). As a result, the metallic particle is “caged” downside the beam focus as shown in Fig. 5.10. Particles with a diameter of about 10 μm can reliably be trapped and manipulated by the beam. However, particles smaller than 10 μm are not trapped steadily, they display rather a twitching motion inside the light cage due to the strong repulsion exerted by the scattering force. In principle, the particles can be trapped above the focus, in a position where buoyant, gravitational and scattering forces are in balance. In practice, such equilibrium position was quite difficult to achieve. Two-dimensional translation of a trapped zinc particle is shown in Fig. 5.14.

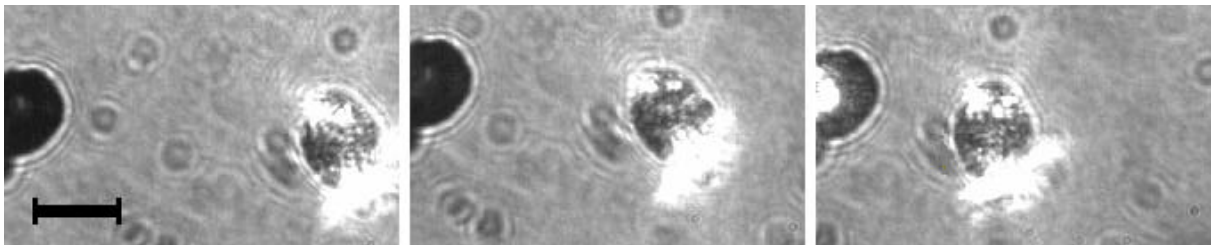


FIGURE 5.14 Translation of a trapped zinc particle in the xy -plane (scale bar 10 μm).

In this case, the laser output power was 90 mW. Further increasing the laser power leads to unstable trapping, because the scattering force is not balanced uniformly from all sides due to the irregular shape of the particle. The scattered laser light is also visible in Fig. 5.14.

trapping of “low-index” micro-droplets

In order to test the functionality of the trap on particles with a refractive index lower than that of the surrounding medium, an inverse water-in-oil emulsion of water droplets in liquid paraffin was prepared by treating the mixture of the two liquids in an ultrasonic bath. The emulsion was then transferred into the microscope chamber and the laser focused onto the sample. The water droplets in the emulsion could be trapped by the hollow beam much more efficiently than it was observed with the metallic particles. This effect can be explained with the much smaller influence of the scattering force for purely dielectric particles. Indeed, the water droplets are not confined by the repulsive scattering force acting from all sides, but rather trapped by the gradient force, which attracts the particle towards the dark core of the beam. The mean diameter of the droplets was 1 μm . Trapping of

a water droplet is shown in Fig. 5.15.

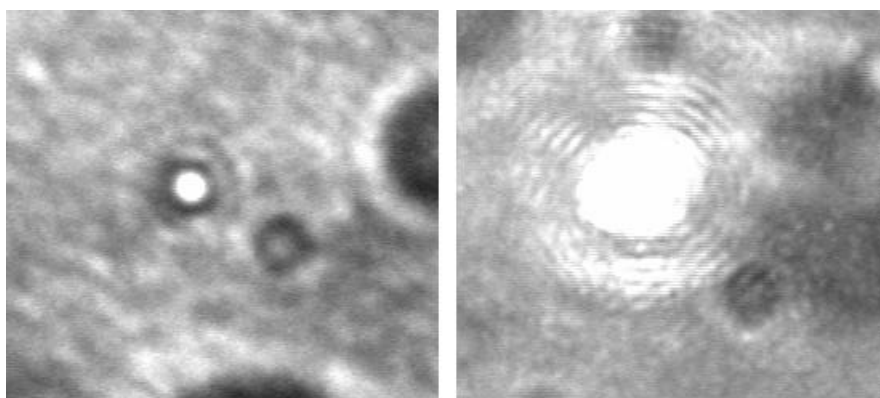


FIGURE 5.15 **Trapping of a water droplet (diameter 1 μm) immersed in liquid paraffin. In the right picture the light scattered by the droplet is visible.**

5.2.4 Discussion

A new hollow-beam laser tweezers suited for trapping and manipulation of both metallic and “low-index”-particles was developed by using an axicon. In contrast to the “dark-core” traps generated with Laguerre-Gaussian modes, which have the dark singularity in the center surrounded only in two dimensions by regions of higher intensity, a so-called “optical bottle” is obtained. Both two-dimensionally and three-dimensionally translation of the particles was successfully demonstrated with this trap. Hollow-beam optical tweezers can have wide application in colloidal chemistry, particularly for the study of the properties of inverse emulsions. The set-up presented here is easy to implement and to align, involving no moving parts for beam scanning or mode converters or holograms for generating a hollow beam. Further improvements of the system are possible. In particular, because the axicon is a non-imaging optical element, a second axicon could be inserted in the set-up in order to obtain a properly collimated beam (i.e. with a constant diameter of the light ring). A further problem is caused by the apex of the axicon which produces unwanted diffraction rings. This problem can also be solved by employing a second axicon. After the beam passes the second axicon, the diffraction rings can be separated from the light tunnel by spatial filtering.

The most compact realization of this idea is the arrangement shown in Fig. 5.15. After passing the axicon, the beam is back-reflected again through the same axicon. The incoming and the reflected light rays are separated by changing the beam polarization with a $\lambda/4$ waveplate used in combination with a polarizing beam splitter.

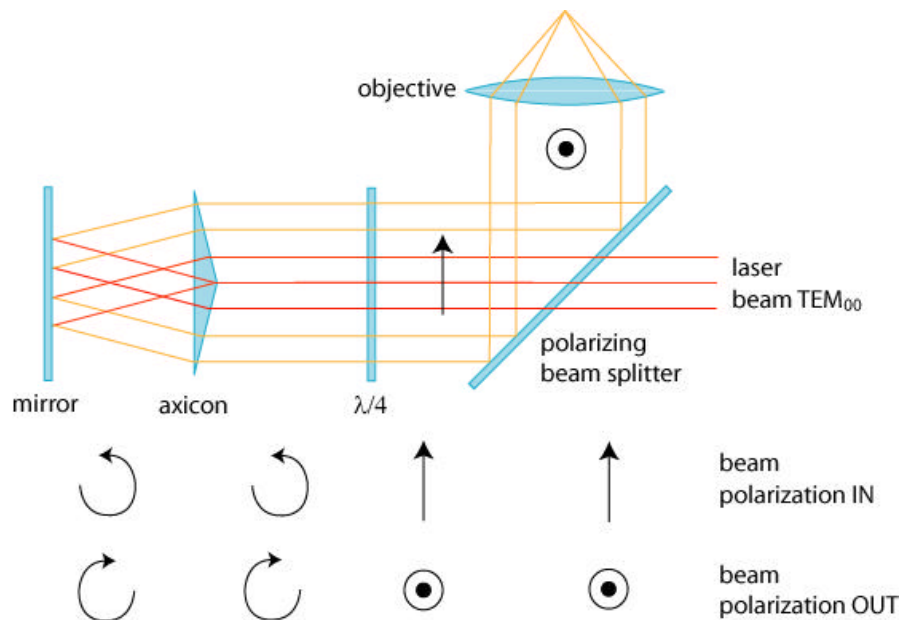


FIGURE 5.15 Producing a collimated hollow beam with a single axicon.

References

- [Abramochkin 1993] Abramochkin E., Volostnikov V.
Opt. Commun. 102: 336- (1993)
- [Ajito 1998] Ajito K.
Combined near-infrared raman microprobe and laser trapping system: application to the analysis of a single organic microdroplet in water.
Appl. spectroscopy 52: 339-342 (1998)
- [Ajito 1999] Ajito K., Morita M.
Imaging and spectroscopic analysis of single microdroplets containing p-cresol using the near-infrared laser tweezers/Raman microprobe system.
Surface Science 427-428: 141-146 (1999)
- [Ajito 2001] Ajito K., Torimitsu K.
Near-infrared Raman spectroscopy of single particles.
Trends in analytical chemistry 20: 255-262 (2001)
- [Allen 1992] Allen L., Beijersbergen M.W., Spreeuw R.J.C., Woerdmann J.P.
Phys. Rev. A 45: 8185-8189 (1992)
- [Arlt 2000] Arlt J., Padgett M. J.
Generation of a beam with a dark focus surrounded by regions of higher intensity: the optical bottle beam.
Opt. Lett. 25: 191-193 (2000)
- [Arlt 2000b] Arlt J., Dholakia K.
Generation of high-order Bessel beams by use of an axicon.
Opt. Comm. 177: 297-301 (2000)
- [Arlt 2001] Arlt J., Garces-Chavez V., Sibbet W., Dholakia K.
Optical micromanipulation using a Bessel light beam.
Opt. Comm 197: 239-245 (2001)
- [Ashkin 1992] Ashkin A.
Forces of a single-beam gradient laser trap on a dielectric sphere in the ray optics regime.
Biophys. J. 61: 569-582 (1992)
- [Belanguer 1978] Belanguer P. A., Rioux M.
Ring pattern of lens-axicon doublet illuminated by a Gaussian beam.
Appl. Opt. 17: 1080-1086 (1978)
- [Beth 1936] Beth R.E.
Mechanical detection and measurement of angular momentum of light.
Phys. Rev. 50 115-125 (1936)
- [Bouchal 2000] Nondiffracting propagation and self-reconstruction of light beams.
http://thunder.upol.cz/optics/research/nondiffracting_beams/
- [Churin 1999] Churin E. G.
Diffraction-limited laser beam shaping by use of computer-generated holograms with dislocations.
Opt. Lett. 24: 620-621 (1999)
- [Davis 1999] Davis J. A., Escalera J. C., Campos J., Marquez A., Yzuel M. J., Iemmi C.
Programmable axial apodizing and hyperresolving amplitude filters

- with a liquid-crystal spatial light modulator.
Opt. Lett. 24: 628-630 (1999)
- [Durnin 1987] Durnin J., Miceli J. J., Eberly J. H.
Phys. Rev. Letters 58: 1499-1501 (1987)
- [Frieze 1996] Frieze M. E. J., Enger J., Rubinsztein-Dunlop H., Heckenberg N. R.
Optical angular-momentum transfer to trapped absorbing particles.
Phys. Rev. A 54: 1593-1596
- [Frieze 1998a] Frieze M. E. J., T. A. Nieminen, N.R. Heckenberg, Rubinsztein-Dunlop H.
Optical torque controlled by elliptical polarization.
Opt. Lett. 23: 1-3 (1998)
- [Frieze 1998b] Frieze M.E.J., Nieminen T.A., Heckenberg N.R., Rubinsztein-Dunlop H.
Optical alignment and spinning of laser-trapped microscopic particles.
Nature 394: 348-350 (1998)
- [Frieze 2001] Frieze M. E. J., Rubinsztein-Dunlop H., Gold J., Hagberg P., Hanstorp D.
Optically driven micromachine elements.
Appl. Phys. Lett. 78: 547-549 (2001)
- [Gahagan 1996] Gahagan K. T., Swartzlander Jr. G. A.
Optical vortex trapping of particles.
Opt. Lett. 21: 827-829 (1996)
- [Gahagan 1998] Gahagan K.T.
Optical manipulation of microparticles and biological structures.
Ph.D. Thesis – Worcester Polytechnic Institute, Faculty of Physics (1998)
- [Gu 2000] Gu M., Morrish D., Ke P.C.
Enhancement of transverse trapping efficiency for a metallic particle using an obstructed laser beam.
Appl. Phys. Lett. 77: 34-36 (2000)
- [Hafizi 1999] Hafizi B., Ganguly A. K., Ting A., Moore C. I., Sprangle P.
Analysis of Gaussian beam and Bessel beam driven laser accelerators.
Phys. Rev. E 60: 4779-4792 (1999)
- [Harris 1994] Harris M., Hill C.A., Tapster P.R., Vaughan J.M.
Phys. Rev. A 49: 3119- (1994)
- [He 1995] He H., Heckenberg N.R., Rubinsztein-Dunlop H.
Optical particle trapping with higher-order doughnut beams produced using high efficiency computer generated holograms.
J. Mod. Opt. 42: 217-223 (1995)
- [Liesener 2000] Liesener J., Reicherter M., Haist T., Tiziani H.J.
Multi-functional optical tweezers using computer-generated holograms.
Opt. Comm. 185: 77-82 (2000)
- [Mair 2000] Mair A.E.
Nichtlokale und singuläre Quantenzustände des Lichts.
PhD Work – University of Wien, Institute of experimental physics (2000)
- [Manek 1998] Manek I., Ovchinnikov Yu. B., Grimm R.

- Generation of hollow laser beam for atom trapping using an axicon.
Opt. Comm. 147: 67-70 (1998)
- [McLeod 1954] McLeod J. H.
J. Opt. Soc. Am. 44: 592- (1954)
- [Mogensen 2000] Mogensen P. C., Gluckstad J.
Dynamic array generation and pattern formation for optical tweezers.
Opt. Comm. 175: 75-81 (2000)
- [Moothoo 2001] Moothoo D. N., Arlt J., Conroy R. S., Akerboom F., Voit A.,
Dholakia K.
Beth's experiment using optical tweezers.
Am. J. Phys. 69: 271-276 (2001)
- [Ng 2000] Ng L. N., Zervas M. N., Wilkinson J. S., Luff B. J.
Manipulation of colloidal gold nanoparticles in the evanescent field
of a channel waveguide.
Appl. Phys. Lett. 76: 1993-1995 (2000)
- [O'Neil 2000] O'Neil A. T., Padgett M. J.
Three-dimensional optical confinement of micron-sized metal
particles and the decoupling of the spin and orbital angular
momentum within an optical spanner.
Opt. Comm. 185: 139-143 (2000)
- [O'Neil2001] O'Neil A. T., Padgett M. J.
Axial and lateral trapping efficiency of Laguerre-Gaussian modes in
inverted optical tweezers.
Opt. Comm. 193: 45-50 (2001)
- [Padgett 1999] Padgett M. J., Allen L.
The angular momentum of light: optical spanners and the rotational
frequency shift.
Opt. Quant. Electr. 31: 1-12 (1999)
- [Padgett 1995] Padgett M.J., Allen L.
The Poynting vector in Laguerre-Gaussian modes.
Opt. Comm. 121: 36-40 (1995)
- [Paterson 2001] Paterson L., MacDonald M. P., Arlt J., Sibbett W., Bryant P. E.,
Dholakia K.
Controlled rotation of optically trapped microscopic particles.
Science 292: 912-914 (2001)
- [Reicherter 1999] Reicherter M., Haist T., Wagemann E. U., Tiziani H. J.
Optical particle trapping with computer-generated holograms written
on a liquid-crystal display.
Opt. Lett. 24: 608-610 (1999)
- [Ren 1990] Ren Q., Birngruber R.
Axicon: a new laser beam delivery system for corneal surgery.
IEEE J. Quantum Electron. 26: 2305-2308 (1990)
- [Rioux 1978] Rioux M., Tremblay R., Belanguer P. A.
Linear, annular, and radial focusing with axicons and applications to
laser machining.
Appl. Opt. 17: 1532-1536 (1978)
- [Sasaki 1991] Sasaki K., Koshio M., Misawa H., Kitamura N., Masuhara H.
Pattern formation and flow control of fine particles by laser-scanning
micromanipulation.
Opt. Lett. 16: 1463-1465 (1991)

- [Sasaki 1992] Sasaki K., Koshioka M., Misawa H., Kitamura N.
Optical trapping of a metal particle and a water droplet by a scanning laser beam.
Appl. Phys. Lett. 60: 807-809 (1992)
- [Sato 1994] Sato S., Harada Y., Waseda Y.
Optical trapping of microscopic metal particles.
Opt. Lett. 19: 1807-1809 (1994)
- [Sato1991] Sato S., Ohyumi M., Shibata H., Inaba H., Ogawa Y.
Optical trapping of small particles using a 1.3-mm compact InGaAsP diode laser.
Opt. Lett. 16: 282-284 (1991)
- [Schäfer 1986] Schäfer F.P.
On some properties of axicons.
Appl. Phys. B 39: 1-8 (1986)
- [Song 1999a] Song Y.
Hollow beam atom tunnel.
Dissertation – University of Maryland (1999)
- [Song1999b] Song Y., Milam D., Hill III W.T.
Long, narrow all-light atom guide.
Opt. Lett. 24: 1805-1807 (1999)
- [Svoboda 1994] Svoboda K., Block S.M.
Optical trapping of metallic Rayleigh particles.
Opt. Lett. 19: 930-932 (1994)
- [Tamm 1990] Tamm C., Weiss C.O.
J. Opt. Soc Am. B 7: 1034- (1990)
- [Webster 2000] Webster S. A., Hechenblaikner G., Hopkins S. A., Arlt J., Foot C. J.
Dipole force trapping of caesium atoms.
J. Phys. B: At. Mol. Opt. Phys. 33: 4149-4155 (2000)

Summary

In this work, an optical tweezers system for measuring forces in the range of piconewton was developed (Chapter II). The system detects the position of a trapped microscopical probe (typically a micrometer-sized latex bead) with high spatial (nm range) and temporal (msec range) resolution. In the system, the laser light that is scattered back by the probe is detected by a *four quadrants photodiode*. By electronically processing the signal generated by each quadrant of the photodiode, the position of the probe can be measured with high accuracy. The analysis of the Brownian motion of a bead inside the harmonic potential of the trap yields information about the local rheological properties of the surrounding environment. The validity of different approaches for analyzing the Brownian motion of the bead were tested by studying the viscosity of simple Newtonian fluids (glycerine/water mixtures). It was found that the *histogram method* yields better results than the methods that use the *corner frequency* or the *autocorrelation function* (Chapter III). For such Newtonian fluids, the local viscosity values are identical to the bulk values.

Next, the developed optical tweezers system was also used as a *scanning probe microscope* for measuring the topography of cellular membranes *in vivo* (Chapter III). In this technique, also known as *optical force microscopy*, the trapped probe works similarly to the scanning stylus in an AFM, while the trap's force potential plays the role of the cantilever. The trapped probe is brought onto the surface of the sample and scanned over it. The change of the position of the probe along the *z*-axis during scanning is

related to the morphology of the surface. Since the stiffness of the optical trap is at least one order of magnitude smaller than the stiffness of AFM cantilevers, optical force microscopy is best suited for studying soft sample like biological membranes. In this work, the membrane of erythroleukemia cells was studied. When the surface of a biological specimen is scanned, non-specific adhesion can induce sticking of the probe to the surface, leading subsequently to the escape of the probe from the trap. This is the most serious problem encountered during the experiments performed in this work. The performed experiments lead to new insights for further improving the technique.

Conventional optical tweezers have some limitations. One limitation is the limited working distance (imposed by the microscope objective usually employed), so that trapping is possible only through thin substrates like 170 μm -thick cover-slips. A further well-known limitation is that particles with a refractive index lower than that of the surrounding medium cannot be trapped by optical tweezers that use a TEM_{00} beam (Gaussian intensity profile). Two new set-ups of optical tweezers overcoming such constraints were developed during this work. First, a new versatile and compact set-up was developed that employs a single aspherical lens as the focusing element (Chapter IV). One advantage of this system is that the very large working distance of the aspherical lens (about 3 mm) allows trapping through thick substrates. Further advantages are the low loss of laser power (by optical absorption) and the possibility to assemble very compact optical tweezers systems.

A second set-up was developed (Chapter V), that employs a conical prism (*axicon*) for generating a hollow-beam optical trap. The axicon converts beams with a TEM_{00} (Gaussian) propagation mode into beams with an annular intensity profile. By focusing the annular beam, an "optical-cup" laser trap is generated. High-reflecting and low-index particles are trapped inside the dark zone of the beam and can be manipulated in three dimensions.

Acknowledgments

I wish to express my sincere thank to the many people who have helped to make this work possible.

First of all I wish to thank my advisor, PD Dr. Jörg Enderlein, for his invaluable guidance, patience, and friendship throughout all my work.

I am grateful to Prof. Dr. Piero Baglioni of the University of Florence for his enduring support. He always encouraged me to pursue my own ideas and in a difficult time his resolution and promptness made possible the prosecution of my work.

I especially thank Martin Böhmer and David Raab. I shared with them much of my lab time and they were for me invaluable colleagues and friends.

Also special thanks to Michael Büschel, Stephan Laib, and Roland Reichenbach-Klinke, for their sincere friendship and generous support.

Thanks also to Matthias Mayer, who kindly provided me with the HeL cells necessary for the experiments.

I wish to thank my father, Dr. Gabriele Pampaloni, for his suggestions and help in electronics, and to all my family. They have always been a rock solid support for me.

I am grateful to Mrs. Magdalena Bauer, for her kindness and for helping me in many administrative questions and problems.

Finally, I wish to thank the staff of the electronic and mechanical workshops of the University of Regensburg, for many suggestions and help in the assembling of my set-up.

Publications and presentations

Zahn M., Kurzbuch D., Pampaloni F., Seeger S.
Optical tweezers as a tool to study molecular interactions at surfaces.
Proc. SPIE 3604 (optical diagnostics of living cells): 90-99 (1999)

Böhmer M.; Pampaloni F.; Wahl M.; Rahn H.J.; Erdmann R.; Enderlein J.
Time-resolved confocal scanning device for ultrasensitive fluorescence detection.
Rev. Sci. Instrum. 72: 4145-52 (2001).

Pampaloni F.; Böhmer M.; Berti D.; Baglioni P.; Enderlein J.
Measuring viscosity by monitoring the Brownian motion of optically trapped micro-beads.
Submitted to *J. Phys. Chem. B*

Pampaloni F., Böhmer M.
Invention: Compact optical tweezers.
Aktenzeichen des Deutschen Patentamts 1D1 43 637.8

4th Workshop of Marie Curie Fellows – MPI für Physik, München (Germany) October 25-27 1999
Measurement of surface forces using microprobes in light gradients - device development and methods. (oral presentation)

5th Workshop of Marie Curie Fellows – University of Bonn, Bonn (Germany) Juli 12-14 2000
- *Imaging cell membrane with optical tweezers.* (oral presentation)
- *Development of versatile optical tweezers by using a single-element compact disk. pickup* (Poster presentation)

6th International Workshop on Single Molecule Detection and Ultrasensitive Analysis in Life Sciences – WISTA Campus, Berlin (Germany) September 27-29 2000
- *Microthermometry by monitoring the Brownian motion of an optically trapped microbead.* (Poster presentation)
- *Optical trapping of dielectric particles using a compact disk singlet objective lens.* (Poster presentation)

3th Annual Linz Winter Workshop – Single Molecule Techniques in Biophysics and Drug Discovery – University of Linz, Linz (Austria) February 2-5 2001
Photonic force microscope with backscattered light feedback control and simultaneous fluorescence detection. (Poster presentation)

2nd International Symposium on Physics, Chemistry and Biology with
Single Molecules – Kloster Banz, Staffelstein (Germany) March 5-7 2001
*Optical confinement and manipulation of microdroplets by hollow-beam
laser tweezers obtained with a conical prism.* (Poster presentation)

NanoBioTec 2001 – Congress Center Halle Münsterland, Münster
(Germany) September 24-27 2001
*New compact optical tweezers for manipulation and sorting of living cells
and micro-particles.* (Poster presentation)

Lebenslauf

Persönliche Daten:

Name:	Francesco Pampaloni
Geburtsdatum:	04.02.1972
Geburtsort:	Florenz (Firenze)
Familienstand:	verheiratet
Staatsangehörigkeit:	italienisch

Schulausbildung:

1978-1991	Grundschule, Orientierungsstufe und Gymnasium in Florenz
1991	Abitur

Zivildienst:

1997-1998	Opera per la Gioventu' G. La Pira – Florenz
-----------	---

Universitätsausbildung:

1992-1997	Studium der Chemie an der Universität Florenz
06.1996-06.1997	Diplomarbeit am Institut für Physikalische Chemie der Universität Florenz (bei Prof. Dr. P. Baglioni) und an der Karl-August- Universität Heidelberg (bei Prof. Dr. J. Wolfrum). Thema: "Laser trapping and manipulation of microscopical probes for the study of molecular adhesion forces"
10.1998-04.2002	Dissertation am Institut für Analytische Chemie, Chemo- und Biosensorik der Universität Regensburg, Thema: "Force sensing and surface analysis with optically trapped microprobes"
04.2002	Doktorprüfung

